Fertilization-induced deformations are controlled by the actin cortex and a mitochondria-rich subcortical layer in ascidian oocytes

by

Silvia Caballero Mancebo

June, 2021

A thesis submitted to the
Graduate School
of the
Institute of Science and Technology Austria
in partial fulfillment of the requirements
for the degree of
Doctor of Philosophy

Committee in charge:

Mario de Bono, Chair
Carl-Philipp Heisenberg
Edouard Hannezo
Alex McDougall

The thesis of Silvia Caballero Mancebo, titled Fertilization-induced deformations are controlled by the actin cortex and a mitochondria-rich subcortical layer in ascidian oocytes, is approved by:

Supervisor: Carl-Philipp Heisenberg, IST Austria, Klosterneuburg, Austria

Signature:

Committee Member: Edouard Hannezo, IST Austria, Klosterneuburg, Austria

Signature:

Committee Member: Alex McDougall, Laboratoire de Biologie du Développement de Villefranche-sur-mer, Sorbonne Université, Villefranche-sur-mer, France

Signature:

Defense Chair: Mario de Bono, IST Austria, Klosterneuburg, Austria

Signature:

Signed page is on file

IST Austria Thesis, ISSN: 2663-337X

[ISBN: 978-3-99078-012-1]

I hereby declare that this thesis is my own work and that it does not contain other people's work without this being so stated; this thesis does not contain my previous work without this being stated, and the bibliography contains all the literature that I used in writing the dissertation.

I declare that this is a true copy of my thesis, including any final revisions, as approved by my thesis committee, and that this thesis has not been submitted for a higher degree to any other university or institution.

I certify that any republication of materials presented in this thesis has been approved by the relevant publishers and co-authors.

Signature: _____

Silvia Caballero Mancebo

June, 2021

Signed page is on file

*Creative Commons licenses:

Buy the ticket, take the ride...

Hunter S. Thompson

Abstract

Cytoplasmic reorganizations are essential for morphogenesis. In large cells like oocytes, these reorganizations become crucial in patterning the oocyte for later stages of embryonic development. Ascidian oocytes reorganize their cytoplasm (ooplasm) in a spectacular manner. Ooplasmic reorganization is initiated at fertilization with the contraction of the actomyosin cortex along the animal-vegetal axis of the oocyte, driving the accumulation of cortical endoplasmic reticulum (cER), maternal mRNAs associated to it and a mitochondria-rich subcortical layer – the myoplasm – in a region of the vegetal pole termed contraction pole (CP). Here we have used the species *Phallusia mammillata* to investigate the changes in cell shape that accompany these reorganizations and the mechanochemical mechanisms underlining CP formation.

We report that the length of the animal-vegetal (AV) axis oscillates upon fertilization: it first undergoes a cycle of fast elongation-lengthening followed by a slow expansion of mainly the vegetal pole (VP) of the cell. We show that the fast oscillation corresponds to a dynamic polarization of the actin cortex as a result of a fertilization-induced increase in cortical tension in the oocyte that triggers a rupture of the cortex at the animal pole and the establishment of vegetal-directed cortical flows. These flows are responsible for the vegetal accumulation of actin causing the VP to flatten.

We find that the slow expansion of the VP, leading to CP formation, correlates with a relaxation of the vegetal cortex and that the myoplasm plays a role in the expansion. We show that the myoplasm is a solid-like layer that buckles under compression forces arising from the contracting actin cortex at the VP. Straightening of the myoplasm when actin flows stops, facilitates the expansion of the VP and the CP. Altogether, our results present a previously unrecognized role for the myoplasm in ascidian ooplasmic segregation.

Acknowledgments

Many people supported my during my PhD and it is my pleasure to express my gratitude to them.

First and foremost, I would like to thank my supervisor Carl-Philipp Heisenberg for giving me the opportunity to work in his lab and for challenging me to work on a second model organism in the lab, which has been really gratifying. I want to commend him for his incredible insight into the project and for giving me the freedom to pursue any direction I wanted during these years. I want to thank my external advisor, Alex McDougall, who genuinely helped me and supported me from the beginning of my PhD. Alex hosted me in his lab for a month and the knowledge and experience I gathered were extremely beneficial for the development of the project and my own as a scientist. I would also like to thank Edouard Hannezo, my internal advisor, for his readiness to help and for his great feedback during our meetings.

Special thanks to Benoit Godard. Thank you for introducing me to the exciting world of ascidian embryology, patiently teaching me how to manipulate ascidian embryos and helping me throughout the project with great feedback.

I want to thank the help and support I received over the years from the Scientific Service Units at IST Austria. I want to thank the Bioimaging Facility for their incredible support we receive every day and their readiness to help whenever something unexpected comes up. I specially want to thank Gabriel Krens for his encouragement and advice, sincerely thank you! I would also like to thank the Electron Microscopy Facility for their collaboration over the years. I would like to acknowledge the contribution of Jack Merrin from the Nanofabrication Facility in designing and building the imaging wells used in this study and the Machine Shop for the design of the cooling stage, essential for the project. I want to thank also the Fish Facility, specially Verena. Although taking care of an ascidian aquarium is not technically 'fish work', she always had time to help me with questions and took an amazing care of the ascidian aquarium and the animals during corona times. Thanks a lot!

I am incredibly grateful to my collaborators: Shayan, Greg, Matilda, Irene and David. Thank you for your help and your amazing contribution!

A huge thanks to past lab members: Jana, Peng, Matt, Michy, Roland, Nicoletta, Conny, Vanessa, Daniel (buddy!), Zoltan, Keisuke, Hitoshi, Philipp, Yuuta, Deborah, Oleksandr and Ehsan. It was great working with you all. I am forever thankful to the present members of the lab for their support during the hard times but also for all the fun we have had over the years. Thank you to Karla, Feyza, Shayan, Ste, Diana, Alex, Gayathri, Nikhil, Suyash, Irene, Koni, Laura, Xin, Naoya and Tushna. A special mention is due to the other member of the ascidian team in the lab, Madison. Thank you for your optimism, support and uncontrollable desire to help during the last year. Getting to know you has been one of my highlights of this year!

Over these years I have met incredible people that have supported me every day and without whom I would not be here. Matilda, Greg and Dani, thank you for the amazing times, for always supporting me and for the little family we have created.

A special mention is due to my friends back home: Marga, Moni, Isa, Cris, Miri, Inma, Sara, Angela, Helga, Noa, Susana, Estela and Maria. Despite the distance, we have had lots of fun and incredible moments meeting up somewhere in the world. Where next?

Finally, I am eternally indebted and grateful to my parents and sister. You have forgiven my absences and born my burdens but have always supported me in any adventure I wanted to pursue in life. Elena thank you for inspiring me every day in so many ways and for your unconditional support. To my parents, thank you for your love, strength and encouragement and for always being participants in my successes. I owe you everything.

About the Author

Silvia Caballero Mancebo completed a BSc and MSc in Biotechnology at the University of Leon (Spain) and an MSc in Nanotechnology at the University of Zaragoza (Spain) before joining IST Austria in September 2014. Her main research interests are how forces shape cells and tissues during embryonic development. During her PhD studies she worked in the research project "Fertilization-induced deformations are controlled by the actin cortex and a mitochondria-rich subcortical layer in ascidian oocytes" in the Heisenberg group at IST Austria. She presented her work at several conferences, such as the 10th International Tunicate Meeting and EMBO conferences. She is also interested in science education and presented her research at the Gymnasium Klosterneuburg and participated in the outreach program *Pop up Science* developed by IST Austria.

List of Collaborators and Publications

1. Slováková J, Sikora M, **Caballero-Mancebo S**, Krens SF G, Kaufman WA, Huljev K, Heisenberg CP. Tension-dependent stabilization of E-cadherin limits cell-cell contact expansion. BioRxiv 2020.11.20.20.391284;
   doi: https://doi.org/10.1101/2020.11.20.391284

2. Shamipour S, **Caballero-Mancebo S**, Heisenberg C-P. Cytoplasm's got moves. Dev. Cell, 56 (2021), pp. 213-226.
   doi: https://doi.org/10.1016/j.devcel.2020.12.002

Table of Contents

List of Figures

List of Tables

List of Abbreviations

2D	Two-dimensional
3D	Three-dimensional
AP	Animal Pole
ASW	Artificial sea water
au	Arbitrary units
AV	Animal-vegetal
BSA	Bovine Serum Albumin
cAMP	Cyclic Adenosine Monophosphate
CAB	Centrosome Attracting Body
C. elegans	*Caenorhabditos elegans*
CaMypt	Constitutively active myosin phosphatase
cER	Cortical Endoplasmic Reticulum
CM	Center of mass
CP	Contraction Pole
GV	Germinal vesicle
GVBD	Germinal vesicle break down
HPF	High Pressure Freezing
LatB	Latrunculin B
LR	Left-right
min	Minutes
mpf	Minutes post fertilization
nm	Nanometers
Noco	Nocodazole
n.s.	Not significant
Pa	Pascals
PB	Polar body
PBS	Phosphate-buffered saline

Pc	Critical pressure
PEM	Posterior End Mark
PIV	Particle Image Velocimetry
pN	Piconewton
Rc	Cell radius
Rp	Pipette radius
RT	Room temperature
s	Seconds
SEM	Scanning Electron Microscopy
Tc	Cortical tension
TEM	Transmission Electron Microscopy
VP	Vegetal Pole
Unfert	Unfertilized
UV	Ultraviolet
YFP	Yellow Fluorescent Protein
µm	Micrometer

1. Introduction

1.1 Cytoplasmic reorganizations

The cytoplasm of cells is a highly crowded environment at the microscopic level[1], yet macroscopic large-scale cytoplasmic reorganizations are essential for various cellular processes such as cell division, migration and polarization[2-3]. Such reorganizations become non-trivial in large cells like oocytes, in which the position of the nucleus and spindle[4-5] or the localization of maternal factors to specific regions within the oocyte[6] has a crucial role in development.

The main driver of cytoplasmic reorganizations is the cell cytoskeleton, mainly microtubules and the actin network. In the next section we will discuss the molecular, cellular and biophysical mechanisms underlying the role of the cell cytoskeleton in such reorganizations in different developmental settings.

In the section 1.2 we will focus on what is known about cytoplasmic reorganizations in the ascidian oocyte and zygote and the molecular mechanisms that drive them.

1.1.1 Cytoplasm's got moves

Publication:

Shamipour S, **Caballero-Mancebo S**, Heisenberg C-P. Cytoplasm's got moves. Dev. Cell, 56 (2021), pp. 213-226.
doi: 10.1016/j.devcel.2020.12.002

Cytoplasm's got moves

Shayan Shamipour1, Silvia Caballero-Mancebo1, and Carl-Philipp Heisenberg1,2,*
1Institute of Science and Technology Austria, Klosterneuburg, Austria
2Lead Contact
*Correspondence: heisenberg@ist.ac.at

Abstract

Cytoplasm is a gel-like crowded environment composed of various macromolecules, organelles, cytoskeletal networks and cytosol. The structure of the cytoplasm is highly organized and heterogeneous due to the crowding of its constituents and their effective compartmentalization. In such an environment, the diffusive dynamics of the molecules are restricted, an effect that is further amplified by clustering and anchoring of molecules. Despite the crowded nature of the cytoplasm at the microscopic scale, large-scale reorganization of the cytoplasm is essential for important cellular functions, such as cell division and polarization. How such mesoscale reorganization of the cytoplasm is achieved, especially for large cells, such as oocytes or syncytial tissues that can span hundreds of micrometers in size, is only beginning to be understood. In this review, we will discuss recent advances in elucidating the molecular, cellular and biophysical mechanisms by which the cytoskeleton drives cytoplasmic reorganization across different scales, structures and species.

Introduction

Central to any form of life is the precise spatiotemporal organization of its building blocks, such as cells and tissues in multicellular organisms and cytoplasmic components in single cells. The importance of cytoplasmic organization becomes particularly apparent in eggs (oocytes), where the localization of large organelles and maternally-deposited molecules within the cytoplasm is crucial for subsequent embryonic development. For instance, the position of the nucleus and spindle within the oocyte can decide oocyte and embryo polarization (Lénárt et al., 2005; Schuh and Ellenberg, 2008), and the subcellular localization of certain maternal mRNAs and proteins within the oocyte can determine the fate of the cells that inherit them (Prodon et al., 2008).

The movement of cytoplasmic components is generally thought to be controlled by a combination of diffusion and active force generation. Diffusion of cytoplasmic molecules can be hampered by their steric as well as binding interactions with surrounding cytoplasmic components and caging effects of cytoskeletal networks, such as actin networks and microtubule structures, resulting in their sub-diffusivity (Luby-Phelps, 2000). Consequently, diffusion alone is not sufficient for fast cytoplasmic reorganization to take place across larger distances (hundreds of micrometers), as found, for instance, in oocytes and syncytial tissues. There, active processes mediated by ATP consumption powering enzymatic processes, such as polymerization and motor protein activity (Brangwynne et al., 2007; Weber et al., 2012), play a decisive role in moving cytoplasmic components. Such active processes can trigger large-scale movements of cytoplasmic components through motor-dependent cytoskeletal network flows and the friction-based interaction of these flowing networks with the cytosol

and other cytoplasmic components (Deneke et al., 2019; Ierushalmi et al., 2020; Sakamoto et al., 2020). Also, motors carrying cargos along cytoskeletal tracks can generate viscous drag forces (see Box 1 for definition) in the adjacent cytoplasm (Goldstein et al., 2008), which triggers the movement of cytoplasmic structures, such as the nucleus, sperm aster and spindles, to specific locations within the cell (Field and Lénárt, 2011; Xie and Minc, 2020). Moreover, the cumulative viscous drag of these moving cargo-motor complexes, e.g. on arrays of microtubules anchored to the cortex, can induce coherent cytoplasmic flows that span tens of micrometers as observed in *Drosophila* oocytes and *Caenorhabditis elegans* (*C. elegans)* zygotes (Kimura et al., 2017; Quinlan, 2016). Such large-scale cytoplasmic flows are of great importance to embryo development, where positioning of cytoplasmic structures such as the golgi, endoplasmic reticulum (ER), granules, nucleus and spindle provides the blueprint for future development.

One remarkable aspect of cytoplasmic reorganization is its capacity for self-organization with the cytoplasm organizing its constituents at both the molecular and cellular scale in the absence of external cues. For instance, homogenized *Xenopus* egg extracts can spontaneously organize their cytoplasmic components, including ER, mitochondria and microtubule structures, into cell-like compartments (Cheng and Ferrell, 2019). Importantly, these processes can occur in the absence of external cues and nuclear material, suggesting that self-organization is inherent to the cytoplasm.

In this review, we will summarize recent advances in unravelling the mechanisms underlying large-scale cytoplasmic rearrangements, their self-organizing capacity and the role of pre-patterning and external cues in steering these processes. We will predominantly focus on the role of the actomyosin and microtubule networks - the main cytoskeletal networks yet implicated in large-scale cytoplasmic rearrangements - describing the forces generated by them both at the surface and in the bulk of the cytoplasm, their functions in cytoplasmic extracts *in vitro*, and how those mechanisms are employed in intact oocytes and embryos.

Actomyosin-mediated processes

The actomyosin cytoskeleton plays a key role in various forms of cytoplasmic reorganization. Generally, the architecture and the connectivity of the actin network as well as the extent of motor activity influences the rate of network contraction and the length scale to which the stresses can be propagated without disrupting the network (Alvarado et al., 2013; Koenderink and Paluch, 2018). Turnover of network components, in addition, allows the maintenance of steady state contractions and flows while preserving network integrity (Malik-Garbi et al., 2019; McFadden et al., 2017). In this section, we will explore how these features of the actomyosin network are employed both in reduced *in vitro* settings and within developmental systems, for mediating robust and tunable large-scale cytoplasmic reorganizations.

Self-organization of the cytoplasm *in vitro*

Seminal studies using *Xenopus* egg extracts demonstrated the potential of the egg cytoplasm to spontaneously undergo gelation and contraction (Field et al., 2011). Moreover, spatially confining these extracts into cell-size three-dimensional (3D) capsules was found to be accompanied by persistent actomyosin network flows directed from the periphery to the center of the capsule (Figure 1A; Pinot et al., 2012). These flows are created by myosin II-mediated active stresses and maintained by the rapid turnover of actomyosin network

components, which allows continuous dissipation of elastic stresses and the diffusion of the disassembled network components back to the capsule surface, where assembly takes place (Malik-Garbi et al., 2019). Notably, this self-organized steady-state flow of actomyosin is not only able to move small particles above a certain minimal size (Colin et al., 2016), but also to induce large-scale reorganization of the encapsulated cytoplasm, apparent by the relocalization of membranous organelle aggregates to distinct locations within the capsule (Tang et al., 2018). The positioning of these aggregates was shown to be capsule-size-dependent, with larger capsules accumulating the organelle aggregates at their center and smaller ones asymmetrically near their surface (Figure 1A). This difference in organelle positioning is related to different forces exerted by the actomyosin network: organelle centering is thought to be achieved by friction forces (see Box 1 for definition) that arise at the contact area between the actin network and its surrounding cytosol. These forces depend on the relative flow velocity between these two structures, their viscosities and the size of the contact area, and are directed opposite to the network flow. Consequently, any network asymmetries relative to the capsule center are balanced by the corresponding asymmetric friction forces, eventually leading to network and organelle centering (Figure 1A-I; Ierushalmi et al., 2020). In addition, organelle centering is promoted by actin polymerization on the side of the organelle surface that faces the outside of the capsule, which in turn generates comet-like pushing forces moving them towards the capsule center (Figure 1A-I; Sakamoto et al., 2020).

Off-center organelle positioning, in contrast, is mediated by the transient and stochastic interaction of the actomyosin network with the capsule boundary, leading to the formation of bridge-like structures, which then pull the organelles to the periphery and position them off-center. These bridge-mediated surface forces become more significant in smaller capsules due to their higher surface-to-volume ratio, promoting organelle off-centering there (Figure 1A-II; Ierushalmi et al., 2020; Sakamoto et al., 2020). Collectively, these studies reveal a tunable mode of self-organization, where by controlling the contractility of the bulk actin network and the extent by which it interacts with the cell boundary and cytoplasm, the symmetric or asymmetric localization of organelles can be controlled in a system-size-dependent manner. In the following, we will describe how the physical principles of actomyosin-mediated cytoplasmic reorganizations identified *in vitro* are applicable to *in vivo* systems, where cytoplasmic reorganization is needed for patterning and morphogenesis.

Nucleus and spindle positioning in the oocyte

Oocytes can be large cells spanning hundreds of micrometers in size. Consequently, large-scale cytoplasmic (ooplasmic) reorganization is needed for proper positioning of the nucleus and spindle within the oocyte, a critical step in axis establishment and early embryonic development. In recent years, various mechanisms driving ooplasmic reorganization in different model organisms were proposed. In starfish oocytes undergoing meiosis, for instance, bulk actin structures were shown to play important roles in chromosome capture and transport towards the animal pole of the oocyte, where the meiotic spindle forms (Lénárt et al., 2005). The chromosomes of prophase I-arrested starfish oocytes are initially scattered across the nucleoplasm. Upon nuclear envelope breakdown (NEBD), an extensive actin network encompasses the nuclear region and undergoes an isotropic and homogeneous mode of contraction while remaining anchored to the nearest part of the cortex at the animal pole (Lénárt et al., 2005; Mori et al., 2011). This results in the translocation of the actin

network together with the entrapped chromosomal material towards the animal pole. The chromosomes are thought to be passively transported by the actin network due to them being larger than the actin network mesh-size (Mori et al., 2011). Notably, contraction of this network is independent of myosin II, and, instead, relies on filamentous actin disassembly (Bun et al., 2018). For filamentous actin disassembly to generate network contraction, a molecule with depolymerizing-end-tracking features would be required, the existence of which in the starfish oocyte still needs to be shown (Bun et al., 2018; Zumdieck et al., 2007).
The actin cytoskeleton also plays an important role in the relocalization of the meiotic spindle, other cytoplasmic domains and maternal mRNAs along the animal-vegetal axis of the ascidian oocyte (Prodon et al., 2006). Upon NEBD, the spindle moves to the animal pole of the oocyte, while a subcortical mitochondria-rich domain (myoplasm) and cortical endoplasmic reticulum (cER), together with maternal mRNAs, accumulate at the vegetal pole. The vegetal translocation of myoplasm and cER was proposed to be triggered by vegetal-directed cortical actomyosin flows at the oocyte periphery, which in turn, due to the incompressibility of the ooplasm, lead to animal-directed back-flow of bulk cytoplasm, thought to maintain the meitoic spindle at the animal pole (Prodon et al., 2008). Yet, the precise mechanism by which the actomyosin network functions in ascidian ooplasmic reorganizations remains to be demonstrated.

Like in starfish and ascidians, the ooplasm of the mouse oocyte contains a highly dynamic actin network (Pfender et al., 2011; Schuh and Ellenberg, 2008). Nucleators of this actin network are localized to both Rab11a vesicles and the oocyte actomyosin cortex, giving rise to a polarized network with actin filament minus ends preferentially pointing towards the interior of the oocyte (Schuh, 2011). In addition to actin nucleators, the Rab11a vesicles also recruit myosin Vb motors, allowing the vesicles to move with increasing motility along the intrinsically polarized bulk actin filaments towards the oocyte cortex where they accumulate (Holubcová et al., 2013; Schuh, 2011). This graded motility of Rab11a vesicles was further proposed to be important for positioning of the nucleus to the oocyte center during prophase, possibly by generating a pressure gradient along the radial axis of the oocyte pushing the nucleus towards the center (Figure 1B-I; Almonacid et al., 2015, 2018). As expected for a pressure gradient, this centering mechanism is not specific to the nucleus and can also drive centering of other cytoplasmic components of a certain minimal size (Colin et al., 2020). Yet, despite efforts in numerically simulating such motility-driven pushing forces, experiments challenging this hypothesis by changing this gradient are still missing.

Upon NEBD the meiotic spindle in mouse oocytes moves from the oocyte center towards the cortex, where it drives the first asymmetric meiotic division. This movement is thought to be driven by the bulk actin cytoskeleton generating both pushing and pulling forces (Azoury et al., 2008; Dumont et al., 2007). Pushing forces on the spindle are generated by an initially uniform actin cloud, polymerized on ER structures surrounding the spindle. This cloud then spontaneously undergoes symmetry breaking, leading to preferential actin accumulation at one side of the spindle, which exerts a comet-like pushing force moving the spindle towards the cortex on the opposite side (Li et al., 2008). Pulling forces by the bulk actin network on the spindle are generated by Rab11a vesicles and their associated actin networks, preferentially moving towards the cortex (see above) and thereby taking the spindle along. Activation of myosin II at the spindle poles further enhances these movements towards the cortex by exerting additional pulling forces on the actin network associated with the Rab11a

vesicles (Holubcová et al., 2013; Schuh and Ellenberg, 2008). Besides the bulk actin network, the cortical actomyosin network was also directly implicated in spindle positioning within the mouse oocyte. As the spindle chromosomes move closer to the cortex, a chromatin-induced signal activates the Arp2/3 complex at the cortex to nucleate actin filaments (Yi et al., 2011). This locally increases cortical thickness, leading to myosin II exclusion from the cortex and cortical softening (Chaigne et al., 2013; Chugh et al., 2017). As a result of this cortical softening, the cortex deforms towards the approaching spindle, thereby increasing the filament density connecting the spindle to the cortex and thus amplifying the pulling forces generated by the bulk actin network associated with Rab11a vesicles (Figure 1B-II; Bennabi et al., 2020; Chaigne et al., 2013, 2015). In addition to enhancing short-range bulk actin network forces, Arp2/3-mediated bulk actin polymerization, mediated by the approaching spindle, is also thought to induce long-range bulk actin flows along the periphery of the oocyte towards its opposite pole. This peripheral flow then triggers a cytoplasmic back-flow in the oocyte center due to the incompressibility of the ooplasm, thereby generating a swirling pattern that pushes the spindle further towards the cortex (Figure 1B-III; Yi et al., 2011, 2013).

Collectively, these findings suggest a number of force-generating mechanisms by which dynamic changes in polymerization and contraction of both the bulk and cortical actin cytoskeleton move the nucleus/spindle within the oocyte. In the following, we will describe how those mechanisms are adapted for triggering large scale reorganization of the cytoplasm in fertilized oocytes/zygotes.

Cytoplasmic streaming in the zygote

Cytoplasmic streaming, occurring both at the cell surface and within the bulk of the cytoplasm, is a common mode of large-scale cytoplasmic reorganization, involved in various cellular processes, including cell polarization (Illukkumbura et al., 2020) and cytoplasmic segregation (Pieuchot et al., 2015; Shamipour et al., 2019).

The function of cytoplasmic streaming in cell polarization was first studied in zygotes, where extensive cytoplasmic reorganization takes place to pattern the embryo. In the *C. elegans* zygote, for instance, cortical actomyosin is initially organized in a filamentous network with many dynamic foci undergoing contractions along the surface of the zygote. At the end of meiosis, the sperm centrosome moves close to the cortex at the future posterior pole of the zygote, where Aurora A kinase released from the centrosome locally suppresses cortical contractions by reducing myosin II activity, thus breaking symmetry of the zygote (Zhao et al., 2019). As a consequence of this local suppression of cortical myosin II, a contractility gradient forms along the anterior-posterior (AP) axis of the zygote, giving rise to anterior-directed cortical actomyosin flows. These flows are thought to trigger and amplify AP polarization by transporting proteins involved in the establishment and maintenance of this polarity towards the anterior of the zygote (Mayer et al., 2010; Munro et al., 2004). Amongst those proteins are PAR3 and PAR6, which initially are uniformly distributed along the cortex but accumulate at the anterior pole upon symmetry breaking. Clustering of anterior PAR proteins is thought to promote their effective friction with the flowing cortical actomyosin network and, consequently, their relocalization to the anterior pole. PAR proteins also feed back on actomyosin contractility and flows by modulating cortical myosin II localization at the poles (Illukkumbura et al., 2020; Munro, 2017). Finally, the anterior-directed cortical actomyosin flows trigger a posterior-directed back-flow of bulk cytoplasm within the zygote due the

incompressibility of the cytoplasm, which is important for the establishment and maintenance of the AP polarity (Mittasch et al., 2018; Niwayama et al., 2011).

Cytoplasmic streaming was shown to also drive the segregation of cytoplasmic components within the zebrafish oocyte/zygote (Fernández et al., 2006; Shamipour et al., 2019). The zebrafish zygote contains a mixture of cytoplasm and yolk granules, which need to completely segregate upon fertilization for subsequent development to proceed normally (Figure 1C-I). This segregation occurs during the first meroblastic cell cleavage cycles, when the cytoplasm streams towards the animal pole and the yolk granules accumulate at the vegetal pole (Fernández et al., 2006). A bulk actin polymerization wave, starting from the nucleus at the animal pole during metaphase, and sweeping across the entire zygote towards the vegetal pole, is thought to drive this segregation by generating both pulling and pushing forces: filamentous actin polymerization establishes an animal-to-vegetal bulk actin gradient triggering large-scale actomyosin flows directed towards the animal pole (Figure 1C-II inset b). This bulk actomyosin flow, in turn, drags the cytoplasm along and leaves the yolk granules behind, due to the larger contact area and thus higher friction of the actin network with the cytosol compared to yolk granules. In addition, the bulk actin polymerization wave also leads to the formation of actin comet-like structures on the animal surface of yolk granules, which push them towards the vegetal pole (Figure 1C-II inset a). This points at a simple and generic mechanism where differential friction forces generated at the interface between a flowing actin cytoskeleton and different cytoplasmic components drive their segregation (Shamipour et al., 2019).

Observations in encapsulated cytoplasmic extracts show that spontaneous symmetry breaking results in center-ward actin flows, suggesting that cytoplasmic streaming can be self-organizing (Ierushalmi et al., 2020; Sakamoto et al., 2020). However, for such cytoplasmic streaming to occur in a polarized manner within oocytes and zygotes, some extent of initial symmetry breaking is required. In the *C. elegans* zygote, this is achieved by the movement of the sperm pronucleus towards the future posterior cell cortex, where it triggers an imbalance in cortical tension, leading to symmetry breaking (Mayer et al., 2010). In the zebrafish and mouse zygote/oocyte, in contrast, symmetry is already broken during oogenesis, apparent by an animal-to-vegetal gradient of bulk actin accumulation (zebrafish) and asymmetric localization of actin nucleators to the animal pole cortex (mouse; see above), setting the flow direction (Shamipour et al., 2019; Yi et al., 2011).

Cytoplasmic streaming in syncytial tissues

Cytoplasmic streaming is a common mechanism for reorganizing the cytoplasm not only at the cell but also tissue scale. This becomes particularly evident in syncytial tissues, where multiple nuclei are embedded in a common cytoplasm. *Drosophila* embryos form a syncytium by undergoing 13 rounds of nuclear divisions without cytokinesis. During the first three division rounds, the nuclei are positioned in the anterior half of the embryo without displaying major displacements. In the following three division rounds, however, extensive and periodic cytoplasmic flows take place within the embryo resulting in spreading of the nuclei along the AP embryonic axis in a cell-cycle-dependent manner (von Dassow and Schubiger, 1994). At the exit of each cell cycle, the level of mitotic phosphatase PP1 increases and spreads up to the actomyosin cortex overlying the dividing nuclei. PP1 activity at the cortex is suggested to recruit myosin II, thereby establishing a global cortical myosin II gradient along the AP axis of

the embryo with its peak adjacent to the dividing nuclei. The cortical myosin II gradient, in turn, creates actomyosin flows directed towards the peak of myosin II close to the center of the embryo, which takes along the directly underlying surface cytoplasm (Deneke et al., 2019). Due to the incompressibility of the cytoplasm, these center-ward cortical and adjacent cytoplasmic flows are balanced by pole-ward flows of the bulk cytoplasm that carry the nuclei along, thereby facilitating nuclei spreading along the AP axis (Figure 2A-I). This continues up to cell cycle 7, when the nuclei are evenly distributed along the AP axis and hence the myosin II gradients are lost (Figure 2A-II). The resultant even spacing of nuclei along the AP axis is critical for ensuring the synchrony of cell cycles by equalizing the nuclear to volume ratio of all nuclei (Deneke et al., 2019). Alternatively, or in addition, the nuclei positioned in the anterior half of the embryo were proposed to dissolve the surrounding bulk actin network, thereby generating a bulk actin network gradient peaking at the anterior and posterior poles, which might also contribute to nuclei redistribution along the AP axis (von Dassow and Schubiger, 1994). Whether and how cortical and bulk actomyosin networks cooperate in distributing the nuclei within the *Drosophila* embryo remains to be shown.

Actin-dependent cytoplasmic streaming is also observed in the *C. elegans* gonad, which is structured into two cylindrical U-shaped arms connected by a common uterus. Each arm consists of a central anucleate region (rachis) that is connected to the surrounding germ cells through cytoplasmic bridges, thereby forming a syncytium. As the germ cells grow and mature into differentiated gametes, they incorporate cytoplasmic components from the rachis due to cytoplasmic flows within the rachis directed towards its proximal end (Figure 2B; Wolke et al., 2007). These flows depend on bulk actomyosin, being upregulated by the major sperm protein signaling pathway at the proximal end of the rachis and downregulated by the GLP-1/Notch signaling pathway at the opposite distal end (Wolke et al., 2007). The resultant proximal-directed cytoplasmic flows are thought to drive oocyte expansion and maturation at the proximal end of the gonad (Nadarajan et al., 2009).

Collectively, both cortical and bulk actin networks were implicated in various forms of cytoplasmic reorganization, leading to cell polarity establishment, cytoplasmic phase segregation and nuclei positioning. The actomyosin cortex typically functions in these processes by undergoing myosin II-dependent contraction and flow, thereby taking along cytoplasmic components at the surface through friction-mediated advective flows. Due to the incompressibility of the cytoplasm at the time-scale of these flows, surface flows often trigger back-flows of bulk cytoplasm that can further reorganize the cytoplasm. The bulk cytoplasm itself contains actin networks that reorganize the cytoplasm by both inducing contraction-mediated advective flows and polymerization-mediated organelle movements, where actin polymerizes in comet-like structures on the surface of these organelles pushing them through the cytoplasm. Importantly, for actin to reliably drive cytoplasmic organization, prior symmetry breaking in the form of polarized distribution of actin nucleators and actin itself seems to be required. Whether this typically occurs through spontaneous symmetry breaking or by prepatterning is still being debated.

Microtubule-mediated processes

The microtubule cytoskeleton plays fundamental roles in orchestrating cytoplasmic reorganization, such as positioning of the nucleus and spindle, transporting molecules and defining the cleavage plane in dividing cells. While at the macroscopic scale the microtubule

cytoskeleton appears to be rather stable, its individual components, such as microtubules and associated motors, are highly dynamic. Microtubules are known to undergo dynamic instabilities defined by (de)polymerization rates, catastrophe and rescue frequencies (Brouhard and Rice, 2018). Moreover, microtubules can self-organize into nematic and polar configurations, where they locally align their orientations such as in the spindle centre (nematic) or radiate out with similar polarity from common foci points, such as in spindle asters (polar). This self-organizing capacity depends on the number of microtubule motors, their speed and the presence of other microtubule associated proteins (Roostalu et al., 2018) and is commonly used by cells to pattern their cytoplasm (Howard and Hyman, 2003). In this section, we aim at describing the large-scale cytoplasmic reorganizations that are mediated by microtubule structures both *in vitro* and *in vivo*, and discuss how their dynamic behavior and interaction with molecular motors and the surrounding cytoplasm can effectively be converted into forces that reorganize the cytoplasm.

Self-organization of the cytoplasm *in vitro*

Studies using interphase *Xenopus* egg extracts showed that the cytoplasm can self-organize across hundreds of micrometers. Homogenized extracts can organize themselves into cell-like compartments with the ER and mitochondria positioned at the center and dense microtubules at the periphery. The organization of these compartments is thought to be mediated by the movement of the microtubule minus-end motor dynein towards the center, taking along ER and mitochondria (Figure 3A; Cheng and Ferrell, 2019). Compartments are also separated from each other by boundary zones that are largely devoid of microtubules, ER or mitochondria. These boundary zones are established by the overlap between neighboring astral microtubule structures, inhibiting plus-end microtubule growth and promoting microtubule plus-end capping (Nguyen et al., 2014, 2018). Together, these findings reveal an important role of the microtubule cytoskeleton for cytoplasmic self-organization in *Xenopus* egg extracts by building cell-like compartments that are clearly separated from each other.

Aster positioning

Microtubules can organize in aster-like polar structures, where microtubules with similar polarity radiate out from common foci points. Microtubule asters are characteristic features of mitotic spindles, where they play a central role in spindle and nucleus positioning during oocyte fertilization and cell division (McNally, 2013). Astral microtubule filament growth or shrinkage, when in contact with surfaces such as the cell cortex, can generate both pushing and pulling forces (Dogterom et al., 2005; Grishchuk et al., 2005), a process previously implicated in nuclei centering in Schizosaccharomyces pombe (Tran et al., 2001) and anterior-ward nucleus translocation during *Drosophila* oogenesis (Zhao et al., 2012). In addition to the forces created by microtubule (de)polymerization, motor-induced pulling forces on microtubules are thought to drive aster positioning through a variety of mechanisms. Microtubule pulling forces can be the result of cortical dynein binding to astral microtubule filaments that are oriented with their plus-ends towards the cortex. Once bound, these dynein motors walk on the microtubule filaments towards their minus-ends, thereby effectively pulling the aster towards the cortex (Nguyen-Ngoc et al., 2007). Pulling forces on astral microtubules were also proposed to be mediated by cargo-carrying dynein motors moving along them (Xie and Minc, 2020). Here, the dynein motors exert pulling forces on the astral microtubules that are equal to the forces they experience by moving through the

surrounding viscous cytoplasm and oriented in the opposite direction of the motor movement. Consequently, the pulling forces exerted by cargo-carrying dynein motors scale with length of microtubule filaments, assuming a constant motor density on those filaments. This length-dependency of pulling forces on aster microtubules can also explain aster centering where asymmetry in aster size is directly translated into asymmetric pulling forces on these asters that in turn reduce this asymmetry (Hamaguchi and Hiramoto, 1986; Tanimoto et al., 2016; Wühr et al., 2010). While this length-dependent pulling model can explain aster centering in the absence of cortical interactions, its underlying assumptions are still being debated. For instance, work on *Xenopus* egg extracts showed that the bulk dynein-mediated forces driving aster migration are exerted only at the surface of the asters and not all along the aster volume (Pelletier et al., 2020), questioning the extent by which the length-dependent pulling model can account for aster movements in different environments. In line with this, analysis of *C. elegans* zygotes revealed that the movement of male and female pronuclei towards the zygote center is not only controlled by dynein-mediated length-dependent pulling forces exerted from the bulk of the cytoplasm, but also affected by dynein motors associated with the cortex and female pronuclear envelope (Figure 3B; De Simone et al., 2018). Moreover, sperm aster centering in sea urchin zygotes was recently suggested to depend on microtubule polymerization-mediated pushing forces against the cortex rather than bulk dynein-mediated drag forces (Meaders et al., 2020).

Cytoplasmic streaming in the oocyte/zygote

Microtubules and their associated molecular motors organize the cytoplasm not only by facilitating transport of organelles, but also more generally by generating forces on their surrounding cytoplasm and cytoskeleton. While the propagation of forces created by a single motor and its associated cargo is local, many cargo-carrying motors moving in the same direction are capable of producing forces that can be transmitted to distant parts of the cytoplasm (Monteith et al., 2016). This effect depends on the cargo size normalized to the distance between cargos, rather than cargo size alone, suggesting that arrays of microtubules, with several molecular motors attached to them can trigger large-scale intracellular cytoplasmic flows (Monteith et al., 2016).

One of the best studied examples for microtubule-driven cytoplasmic flows reorganizing the cytoplasm is the developing *Drosophila* oocyte, which is connected to 15 nurse cells at its anterior side. During oogenesis, the nurse cells pump their cytoplasm into the oocyte, thereby providing the oocyte with mRNAs, proteins and organelles needed for its maturation and growth (Quinlan, 2016). This process is accompanied by cytoplasmic streaming within the oocyte, which can be subdivided into an initial slow phase (Figure 3C-I) followed by a fast phase (Figure 3C-II), which together are required for segregation of maternal determinants and mixing of the nurse cells cytoplasm with the oocyte ooplasm (Becalska and Gavis, 2009; Gutzeit and Koppa, 1982). Both phases rely on microtubules and the microtubule motor kinesin-1 (Gutzeit, 1986; Palacios and St Johnston, 2002). The function of kinesin-1 in these processes critically depends on the buildup of a dynamic 3D network of microtubules within the oocyte during mid to late stages of oogenesis (Quinlan, 2016). This network is nucleated at the cortical regions of the oocyte, where γ-tubulin is enriched (Parton et al., 2011). Kinesin-1 mediated organelle transport along this yet unordered network results in slow and disordered cytoplasmic streaming, due to the resultant viscous drag forces in the ooplasm (Figure 3C-inset a; Ganguly et al., 2012). Concomitant with the onset of late oogenesis, when

the nurse cells pump all their remaining cytoplasm into the oocyte, the microtubule network self-organizes into parallel arrays, thereby creating long-range cytoplasmic streaming, which promotes the mixing of nurse cell cytoplasm with oocyte ooplasm (Figure 3C-inset d; Quinlan, 2016). This microtubule self-organization into parallel arrays is mediated by kinesin-1 motors moving towards microtubules plus ends, thereby generating viscous drag forces on the ooplasm as well as compressive forces on the microtubules on which they move, and requires kinesin-1 to cross a threshold level of activity (Monteith et al., 2016). Viscous drag forces promote microtubule alignment by generating cytoplasmic flows that synchronize the movement of neighboring microtubules (Figure 3C-inset b), while compressive forces function in this process by triggering microtubule buckling, which facilitates their reconfiguration into parallel arrays (Figure 3C-inset c). Microtubule alignment, in turn, enhances the viscous drag forces created by the kinesin-1 motors and their associated cargos and, consequently induces cytoplasmic flows across the oocyte in a positive-feedback loop (Ganguly et al., 2012; Monteith et al., 2016). In addition to these mechanisms, microtubule alignment and generation of long-range cytoplasmic streaming within the oocyte are thought to also rely on other non-exclusive processes, such as the relocalization of γ-tubulin, the dissolution of the bulk actin network, and the regulation of other motor activities (Dahlgaard et al., 2007; Parton et al., 2011; Serbus et al., 2005).

The ability of microtubules and associated motors to generate viscous drag forces inducing cytoplasmic flows critically depends on the presence of cytoskeletal and macromolecular structures within the cytoplasm. Studies in *C. elegans* zygotes, for instance, demonstrated that during meiosis II, the ooplasm undergoes extensive flows, which are dependent not only on microtubules and kinesin-1 motors, but also ER structures within the cytoplasm. In this process, microtubules, anchored to the cortex with their minus ends are thought to generate cytoplasmic streaming by recruiting kinesin-1 motors that carry large cargoes, such as ER, and move towards the microtubule plus ends thereby inducing drag forces in the cytoplasm (Figure 3D; Kimura et al., 2017). Reminiscent of the situation in the *Drosophila* oocyte (see above), the cytoplasmic flows induced by the viscous drag forces are thought to drive the alignment between neighboring microtubules in a positive-feedback loop that enhances the cytoplasmic flows and relies on ER-mediated hydrodynamic coupling (see Box 1 for definition) between microtubules and the cytoplasm (Figures 3D-inset a and b). Similar observations were also made in *Xenopus* egg extracts, where ER was shown to be critical for microtubule-induced cytoplasmic flows by acting not only as cargo creating viscous drag forces in the cytoplasm, but also transducing these forces across longer distances (Kimura et al., 2017).

Nuclei positioning in syncytial tissues

Besides their function in determining mitotic spindle positioning and driving cytoplasmic flows, microtubules are also essential for nuclei positioning in syncytial tissues. In the *Drosophila* syncytial stage embryo, nuclei, after distributing along the embryo AP axis (see above), relocalize from the interior of the embryo towards the surface, a process thought to rely on microtubules (Figures 4A-I and 4A-III; Zalokar and Erk, 1976). Analysis of microtubule aster shape during nuclear migration revealed that they are asymmetric with the shorter side pointing towards the surface, suggesting that a microtubule length-dependent pulling mechanism, as described for aster positioning in other systems, is unlikely to mediate this process. Instead, a pushing model was proposed, where a network of interdigitating

microtubule asters generate forces that repel neighboring nuclei, thereby driving their cortical relocalization (Figure 4A-II; Baker et al., 1993).

Once the nuclei have arrived at the surface of the *Drosophila* syncytium, they undergo four more rounds of nuclear divisions before cellularization sets in. Interestingly, while during each cycle the spindles expand their length to segregate chromosomes, they still remain homogeneously distributed within the tissue (Figures 4B-I and 4B-III; de-Carvalho et al., 2020). This points at the existence of a local ordering mechanism, regulating the distance between neighboring spindles. Analogous to the nuclear migration towards the surface (Baker et al., 1993; see above), forces that repulse neighboring asters and thereby define spindle positioning and orientation, were proposed to represent such ordering mechanism (Figure 4B-II). How those repulsive forces are established is not yet entirely clear, but the interaction zones between astral microtubules of adjacent spindles, consisting of overlapping antiparallel microtubules, were shown to recruit cytoskeletal proteins that cross-link microtubules and thus potentially confer mechanical stiffness to those zones (Deshpande et al., 2019).

Collectively, microtubules predominantly function in cytoplasmic reorganization by recruiting motors that exert forces on surrounding cytoplasmic structures and the microtubules themselves. These effects depend on motor activity, density and cargo size, and the mechanical properties of the microtubules and surrounding structures. The effect on surrounding structures becomes particularly apparent in processes where microtubules induce large-scale cytoplasmic streaming, while the effect on microtubules themselves is best understood in regard to mitotic spindle/aster positioning. Interestingly, for the effect of microtubules in generating large-scale cytoplasmic flows, positive-feedback of such flows on microtubule alignment seems to be important. In addition, microtubule (de)polymerization in contact with surfaces represents another mode of aster/nuclei positioning.

Perspectives

In this review, we describe several examples from both *in vitro* assays and *in vivo* developmental processes, in which the actin and microtubule cytoskeletons and their associated motor proteins induce large-scale cytoplasmic reorganizations. While those examples typically focus on the activity of either of these cytoskeletal structures, the crosstalk between them likely plays an important role in controlling various aspects of cytoplasmic reorganization, such as symmetry-breaking, force generation and transduction. For instance, in the case of *Drosophila* oocytes, where a microtubule network in conjunction with kinesin-1 motors triggers the transition from local unordered to large-scale ordered cytoplasmic flows, depolymerization of the filamentous actin network seems to be needed to facilitate this process (Manseau et al., 1996). This is consistent with *in vitro* studies, where the actin cytoskeleton was found to modulate the speed of organelle transport along microtubule filaments by hindering microtubule growth and controlling cytoplasmic viscosity (Colin et al., 2018; Pelletier et al., 2020). Microtubules were also found to influence actin-mediated cytoplasmic reorganization e.g. in the process of spindle positioning in mouse oocytes, where microtubule-dependent cortical anchoring of the meiotic spindle prevents premature actin-mediated spindle relocalization (Vasquez et al., 2020). Together, these findings support the notion that cytoplasmic reorganization critically depends on the coordinated activities of the actin and microtubule cytoskeletons.

Large-scale cytoplasmic reorganization not only depends on the coaction of different cytoskeletal networks themselves, but also is tightly linked to the cell cycle with Cdk1 playing an important role therein. For instance, the bulk actin cytoskeleton in *Xenopus* egg extracts and zebrafish zygotes undergoes periodic cycles of polymerization and contraction in phase with and dependent on Cdk1 activity levels (Field et al., 2011; Shamipour et al., 2019). The cortical actomyosin network, in contrast, is antiphasic with the Cdk1 cycle, disassembling when Cdk1 activity peaks, a phenomenon commonly observed in the starfish oocyte and the *Drosophila* syncytial blastoderm (Bischof et al., 2017; Deneke et al., 2019). Notably, Cdk1 not only affects the actomyosin cytoskeleton, but also astral microtubules growth (Belmont et al., 1990; Verde et al., 1992), suggesting multiple cytoskeletal effector processes by which Cdk1 controls cytoplasmic reorganization. One recent example for this dual function of Cdk1 in controlling both the actin and microtubule cytoskeletons is the regulation of homogeneous nuclear distribution in the *Drosophila* syncytial blastoderm (Lv et al., 2020). Here, a Cdk1 trigger wave traveling along the AP axis of the embryo not only controls cell cycle-dependent mitotic spindle formation, but also tissue material properties by affecting actin network formation. Differences in tissue material properties along the AP axis, in turn, affect how the mitotic spindles and associated microtubule asters distribute within the tissue during nuclei divisions, a process important for proper dispersion of nuclei within the syncytial embryo (Lv et al., 2020). Collectively, the ability of Cdk1 to form a trigger wave (Chang and Ferrell, 2013; Deneke et al., 2016), together with its capacity of modulating actin and microtubules, suggest that it can be at the core of a self-organizing module underlying cell cycle-dependent cytoplasmic reorganization in large oocytes and syncytial tissues.

Intriguingly, the cytoplasm can display different material properties, influencing how cytoplasmic reorganization takes place (Almonacid et al., 2015). Yet, how the material properties of the cytoplasm are spatiotemporally organized in large cells and syncytial tissues remains unclear. Intermediate filaments are likely candidates to be involved in this process, as they are known to play an important role in safeguarding the mechanical integrity of cells and tissues (Sanghvi-Shah and Weber, 2017). For instance, disassembly of actin and keratin intermediate filaments in the zone between neighboring microtubule asters was found to soften the midzone locally and facilitate aster segregation (Field et al., 2019; Pelletier et al., 2020). Intermediate filaments can also interact with other cytoskeletal networks, as for instance found in filamentous actin functioning as a template for intermediate filament assembly (Weber and Bement, 2002). However, the mode of action by which intermediate filaments function in cytoplasmic reorganization remains to be explored.

Although various mechanisms driving cytoplasmic reorganization have been proposed, the exact nature and relative contribution of forces generated at the cell cortex and bulk of the cytoplasm are still being debated. Due to the viscous nature of the cytoplasm and cortex, their flows are hydrodynamically coupled (Niwayama et al., 2011). As a result, cortical actomyosin flows can trigger cytoplasmic flows and vice versa (Deneke et al., 2019; Mittasch et al., 2018). Likewise, microtubule polymerization-based pushing forces against the cortex (Meaders et al., 2020; Sulerud et al., 2020) and the motor-mediated pulling forces on microtubules generated in the bulk of the cytoplasm (Hamaguchi and Hiramoto, 1986; Tanimoto et al., 2016) can effectively lead to similar cytoplasmic movements. This makes it often difficult to unequivocally pinpoint the place within the cell where the forces driving those movements/flows are generated. To overcome these limitations, new optogenetic tools and

biosensors for spatiotemporally manipulating and monitoring the activity of molecular motors (Deneke et al., 2019) need to be developed, with the help of which the different force-generating processes driving cytoplasmic reorganization can be dissected. Furthermore, the advancement of imaging modalities allowing e.g. live-imaging of microfilaments and their associated motors deep within the organism, and the development of reductionist approaches, such as cytoplasmic extracts within microfabricated chambers (de-Carvalho et al., 2020; Shamipour et al., 2019), will be critical for distinguishing the contributions of various force-generating processes to cytoplasmic reorganization. In addition to force generation, questions remain as to the extent by which the material properties of the cytoplasm affect cytoplasmic reorganization. Yet, biophysical tools to measure those properties, such as magnetic tweezers, pipette aspiration and ferrofluidic droplets (D'Angelo et al., 2019; Serwane et al., 2017; Shamipour et al., 2019) have so far been predominantly used on tissues, and thus need to be adapted and refined for use on single cells. Finally, the development and application of theoretical models, which when combined with precise biophysical measurements can test the plausibility of certain proposed mechanisms of cytoplasmic reorganization, will be indispensable for refining current models and predicting features that are not accessible by intuition only. This needs to be accompanied by the development of new biophysical tools, such as the induction of cytoplasmic flows by non-invasive focused laser light (Mittasch et al., 2018), with which one can directly address the predictions made by those models. Collectively, the combined use of experiments and theory will not only shed light on the capacity of the cytoplasm to self-organize, but also on the inherent spatial and temporal limitations of such self-organization and, consequently, why multicellularity has emerged in evolution.

Box 1. Glossary

Friction force: The resistance force between materials/objects, which are in contact and move relative to each other.
Viscous drag force: The friction force that a material/object experiences when moving through a viscous fluid.
Hydrodynamic coupling: The capacity of viscous fluid material in long-range transmission of forces.

References

Almonacid, M., Ahmed, W.W., Bussonnier, M., Mailly, P., Betz, T., Voituriez, R., Gov, N.S., and Verlhac, M.-H. (2015). Active diffusion positions the nucleus in mouse oocytes. Nat. Cell Biol. 17, 470–479.

Almonacid, M., Terret, M.-E., and Verlhac, M.-H. (2018). Control of nucleus positioning in mouse oocytes. Semin. Cell Dev. Biol. 82, 34–40.

Alvarado, J., Sheinman, M., Sharma, A., MacKintosh, F.C., and Koenderink, G.H. (2013). Molecular motors robustly drive active gels to a critically connected state. Nat. Phys. 9, 591–597.

Azoury, J., Lee, K.W., Georget, V., Rassinier, P., Leader, B., and Verlhac, M.-H. (2008). Spindle positioning in mouse oocytes relies on a dynamic meshwork of actin filaments. Curr. Biol. 18, 1514–1519.

Baker, J., Theurkauf, W.E., and Schubiger, G. (1993). Dynamic changes in microtubule configuration correlate with nuclear migration in the preblastoderm Drosophila embryo. J. Cell Biol. 122, 113–121.

Becalska, A.N., and Gavis, E.R. (2009). Lighting up mRNA localization in Drosophila oogenesis. Development 136, 2493–2503.

Belmont, L.D., Hyman, A.A., Sawin, K.E., and Mitchison, T.J. (1990). Real-time visualization of cell cycle-dependent changes in microtubule dynamics in cytoplasmic extracts. Cell 62, 579–589.

Bennabi, I., Crozet, F., Nikalayevich, E., Chaigne, A., Letort, G., Manil-Ségalen, M., Campillo, C., Cadart, C., Othmani, A., Attia, R., et al. (2020). Artificially decreasing cortical tension generates aneuploidy in mouse oocytes. Nat. Commun. 11, 1649.

Bischof, J., Brand, C.A., Somogyi, K., Májer, I., Thome, S., Mori, M., Schwarz, U.S., and Lénárt, P. (2017). A cdk1 gradient guides surface contraction waves in oocytes. Nat. Commun. 8, 849.

Brangwynne, C.P., MacKintosh, F.C., and Weitz, D.A. (2007). Force fluctuations and polymerization dynamics of intracellular microtubules. Proc. Natl. Acad. Sci. USA 104, 16128–16133.

Brouhard, G.J., and Rice, L.M. (2018). Microtubule dynamics: an interplay of biochemistry and mechanics. Nat. Rev. Mol. Cell Biol. 19, 451–463.

Bun, P., Dmitrieff, S., Belmonte, J.M., Nédélec, F.J., and Lénárt, P. (2018). A disassembly-driven mechanism explains F-actin-mediated chromosome transport in starfish oocytes. eLife 7, e31469.

de-Carvalho, J., Tlili, S., Hufnagel, L., Saunders, T.E., and Telley, I.A. (2020). Aster repulsion drives local ordering in an active system. BioRxiv doi: 10.1101/2020.06.04.133579.

Chaigne, A., Campillo, C., Gov, N.S., Voituriez, R., Azoury, J., Umaña-Diaz, C., Almonacid, M., Queguiner, I., Nassoy, P., Sykes, C., et al. (2013). A soft cortex is essential for asymmetric spindle positioning in mouse oocytes. Nat. Cell Biol. 15, 958–966.

Chaigne, A., Campillo, C., Gov, N.S., Voituriez, R., Sykes, C., Verlhac, M.H., and Terret, M.E. (2015). A narrow window of cortical tension guides asymmetric spindle positioning in the mouse oocyte. Nat. Commun. 6, 6027.

Chang, J.B., and Ferrell, J.E. (2013). Mitotic trigger waves and the spatial coordination of the Xenopus cell cycle. Nature 500, 603–607.

Cheng, X., and Ferrell, J.E. (2019). Spontaneous emergence of cell-like organization in Xenopus egg extracts. Science 366, 631–637.

Chugh, P., Clark, A.G., Smith, M.B., Cassani, D.A.D., Dierkes, K., Ragab, A., Roux, P.P., Charras, G., Salbreux, G., and Paluch, E.K. (2017). Actin cortex architecture regulates cell surface tension. Nat. Cell Biol. 19, 689–697.

Colin, A., Bonnemay, L., Gayrard, C., Gautier, J., and Gueroui, Z. (2016). Triggering signaling pathways using F-actin self-organization. Sci. Rep. 6, 34657.

Colin, A., Singaravelu, P., Théry, M., Blanchoin, L., and Gueroui, Z. (2018). Actin-Network Architecture Regulates Microtubule Dynamics. Curr. Biol. 28, 2647-2656.

Colin, A., Letort, G., Razin, N., Almonacid, M., Ahmed, W., Betz, T., Terret, M.-E., Gov, N.S., Voituriez, R., Gueroui, Z., et al. (2020). Active diffusion in oocytes nonspecifically centers large objects during prophase I and meiosis I. J. Cell Biol. 219.

Dahlgaard, K., Raposo, A.A.S.F., Niccoli, T., and St Johnston, D. (2007). Capu and Spire assemble a cytoplasmic actin mesh that maintains microtubule organization in the Drosophila oocyte. Dev. Cell 13, 539–553.

D'Angelo, A., Dierkes, K., Carolis, C., Salbreux, G., and Solon, J. (2019). In Vivo Force Application Reveals a Fast Tissue Softening and External Friction Increase during Early Embryogenesis. Curr. Biol. 29, 1564-1571.

von Dassow, G., and Schubiger, G. (1994). How an actin network might cause fountain streaming and nuclear migration in the syncytial Drosophila embryo. J. Cell Biol. 127, 1637–1653.

De Simone, A., Spahr, A., Busso, C., and Gönczy, P. (2018). Uncovering the balance of forces driving microtubule aster migration in C. elegans zygotes. Nat. Commun. 9, 938.

Deneke, V. E., Melbinger, A., Vergassola, M., & Di Talia, S. (2016). Waves of Cdk1 Activity in S Phase Synchronize the Cell Cycle in Drosophila Embryos. Dev. Cell, 38, 399–412.

Deneke, V.E., Puliafito, A., Krueger, D., Narla, A.V., De Simone, A., Primo, L., Vergassola, M., De Renzis, S., and Di Talia, S. (2019). Self-Organized Nuclear Positioning Synchronizes the Cell Cycle in Drosophila Embryos. Cell 177, 925-941.

Deshpande, O., de-Carvalho, J., Vieira, D.V., and Telley, I.A. (2019). Astral microtubule crosslinking by Feo safeguards uniform nuclear distribution in the Drosophila syncytium. BioRxiv doi: 10.1101/859975.

Dogterom, M., Kerssemakers, J.W.J., Romet-Lemonne, G., and Janson, M.E. (2005). Force generation by dynamic microtubules. Curr. Opin. Cell Biol. 17, 67–74.

Dumont, J., Million, K., Sunderland, K., Rassinier, P., Lim, H., Leader, B., and Verlhac, M.-H. (2007). Formin-2 is required for spindle migration and for the late steps of cytokinesis in mouse oocytes. Dev. Biol. 301, 254–265.

Fernández, J., Valladares, M., Fuentes, R., and Ubilla, A. (2006). Reorganization of cytoplasm in the zebrafish oocyte and egg during early steps of ooplasmic segregation. Dev. Dyn. 235, 656–671.

Field, C.M., and Lénárt, P. (2011). Bulk cytoplasmic actin and its functions in meiosis and mitosis. Curr. Biol. 21, R825-830.

Field, C.M., Wuhr, M., Anderson, G.A., Kueh, H.Y., Strickland, D., and Mitchison, T.J. (2011). Actin behavior in bulk cytoplasm is cell cycle regulated in early vertebrate embryos. J. Cell Sci. 124, 2086–2095.

Field, C.M., Pelletier, J.F., and Mitchison, T.J. (2019). Disassembly of Actin and Keratin Networks by Aurora B Kinase at the Midplane of Cleaving Xenopus laevis Eggs. Curr. Biol. 29, 1999-2008.

Ganguly, S., Williams, L.S., Palacios, I.M., and Goldstein, R.E. (2012). Cytoplasmic streaming in Drosophila oocytes varies with kinesin activity and correlates with the microtubule cytoskeleton architecture. Proc. Natl. Acad. Sci. USA. 109, 15109–15114.

Goldstein, R.E., Tuval, I., and van de Meent, J.-W. (2008). Microfluidics of cytoplasmic streaming and its implications for intracellular transport. Proc. Natl. Acad. Sci. USA. 105, 3663–3667.

Grishchuk, E.L., Molodtsov, M.I., Ataullakhanov, F.I., and McIntosh, J.R. (2005). Force production by disassembling microtubules. Nature 438, 384–388.

Gutzeit, H. (1986). The role of microtubules in the differentiation of ovarian follicles during vitellogenesis in Drosophila. Roux's Arch. Dev. Biol. 195, 173–181.

Gutzeit, H., and Koppa, R. (1982). Time-lapse film analysis of cytoplasmic streaming during late oogenesis of Drosophila. J. Embryol. Exp. Morphol. 67, 101-111.

Hamaguchi, M.S., and Hiramoto, Y. (1986). Analysis of the Role of Astral Rays in Pronuclear Migration in Sand Dollar Eggs by the Colcemid-UV Method. Dev. Growth Differ. 28, 143–156.

Holubcová, Z., Howard, G., and Schuh, M. (2013). Vesicles modulate an actin network for asymmetric spindle positioning. Nat. Cell Biol. 15, 937–947.

Howard, J., and Hyman, A.A. (2003). Dynamics and mechanics of the microtubule plus end. Nature 422, 753–758.

Ierushalmi, N., Malik-Garbi, M., Manhart, A., Abu Shah, E., Goode, B.L., Mogilner, A., and Keren, K. (2020). Centering and symmetry breaking in confined contracting actomyosin networks. eLife 9, e55368.

Illukkumbura, R., Bland, T., and Goehring, N.W. (2020). Patterning and polarization of cells by intracellular flows. Curr. Opin. Cell Biol. 62, 123–134.

Kimura, K., Mamane, A., Sasaki, T., Sato, K., Takagi, J., Niwayama, R., Hufnagel, L., Shimamoto, Y., Joanny, J.-F., Uchida, S., et al. (2017). Endoplasmic-reticulum-mediated microtubule alignment governs cytoplasmic streaming. Nat. Cell Biol. 19, 399–406.

Koenderink, G.H., and Paluch, E.K. (2018). Architecture shapes contractility in actomyosin networks. Curr. Opin. Cell Biol. 50, 79–85.

Lénárt, P., Bacher, C.P., Daigle, N., Hand, A.R., Eils, R., Terasaki, M., and Ellenberg, J. (2005). A contractile nuclear actin network drives chromosome congression in oocytes. Nature 436, 812–818.

Li, H., Guo, F., Rubinstein, B., and Li, R. (2008). Actin-driven chromosomal motility leads to symmetry breaking in mammalian meiotic oocytes. Nat. Cell Biol. 10, 1301–1308.

Luby-Phelps, K. (2000). Cytoarchitecture and physical properties of cytoplasm: volume, viscosity, diffusion, intracellular surface area. Int. Rev. Cytol. 192, 189–221.

Lv, Z., Rosenbaum, J., Mohr, S., Zhang, X., Kong, D., Preiß, H., Kruss, S., Alim, K., Aspelmeier, T., and Großhans, J. (2020). The Emergent Yo-yo Movement of Nuclei Driven by Cytoskeletal Remodeling in Pseudo-synchronous Mitotic Cycles. Curr. Biol. 30, 2564-2573.

Malik-Garbi, M., Ierushalmi, N., Jansen, S., Abu-Shah, E., Goode, B.L., Mogilner, A., and Keren, K. (2019). Scaling behaviour in steady-state contracting actomyosin networks. Nat. Phys. 15, 509–516.

Manseau, L., Calley, J., and Phan, H. (1996). Profilin is required for posterior patterning of the Drosophila oocyte. Development 122, 2109–2116.

Mayer, M., Depken, M., Bois, J.S., Jülicher, F., and Grill, S.W. (2010). Anisotropies in cortical tension reveal the physical basis of polarizing cortical flows. Nature 467, 617–621.

McFadden, W.M., McCall, P.M., Gardel, M.L., and Munro, E.M. (2017). Filament turnover tunes both force generation and dissipation to control long-range flows in a model actomyosin cortex. PLoS Comput. Biol. 13, e1005811.

McNally, F.J. (2013). Mechanisms of spindle positioning. J. Cell Biol. 200, 131–140.

Meaders, J.L., de Matos, S.N., and Burgess, D.R. (2020). A Pushing Mechanism for Microtubule Aster Positioning in a Large Cell Type. Cell Rep. 33, 108213.

Mittasch, M., Gross, P., Nestler, M., Fritsch, A.W., Iserman, C., Kar, M., Munder, M., Voigt, A., Alberti, S., Grill, S.W., et al. (2018). Non-invasive perturbations of intracellular flow reveal physical principles of cell organization. Nat. Cell Biol. 20, 344–351.

Monteith, C.E., Brunner, M.E., Djagaeva, I., Bielecki, A.M., Deutsch, J.M., and Saxton, W.M. (2016). A Mechanism for Cytoplasmic Streaming: Kinesin-Driven Alignment of Microtubules and Fast Fluid Flows. Biophys. J. 110, 2053–2065.

Mori, M., Monnier, N., Daigle, N., Bathe, M., Ellenberg, J., and Lénárt, P. (2011). Intracellular transport by an anchored homogeneously contracting F-actin meshwork. Curr. Biol. 21, 606–611.

Munro, E. (2017). Protein Clustering Shapes Polarity Protein Gradients. Dev. Cell 42, 309–311.

Munro, E., Nance, J., and Priess, J.R. (2004). Cortical flows powered by asymmetrical contraction transport PAR proteins to establish and maintain anterior-posterior polarity in the early C. elegans embryo. Dev. Cell 7, 413–424.

Nadarajan, S., Govindan, J.A., McGovern, M., Hubbard, E.J.A., and Greenstein, D. (2009). MSP and GLP-1/Notch signaling coordinately regulate actomyosin-dependent cytoplasmic streaming and oocyte growth in C. elegans. Development 136, 2223–2234.

Nguyen, P.A., Groen, A.C., Loose, M., Ishihara, K., Wühr, M., Field, C.M., and Mitchison, T.J. (2014). Spatial organization of cytokinesis signaling reconstituted in a cell-free system. Science 346, 244–247.

Nguyen, P.A., Field, C.M., and Mitchison, T.J. (2018). Prc1E and Kif4A control microtubule organization within and between large Xenopus egg asters. Mol. Biol. Cell 29, 304–316.

Nguyen-Ngoc, T., Afshar, K., and Gönczy, P. (2007). Coupling of cortical dynein and G alpha proteins mediates spindle positioning in Caenorhabditis elegans. Nat. Cell Biol. 9, 1294–1302.

Niwayama, R., Shinohara, K., and Kimura, A. (2011). Hydrodynamic property of the cytoplasm is sufficient to mediate cytoplasmic streaming in the Caenorhabditis elegans embryo. Proc. Natl. Acad. Sci. USA. 108, 11900–11905.

Palacios, I.M., and St Johnston, D. (2002). Kinesin light chain-independent function of the Kinesin heavy chain in cytoplasmic streaming and posterior localisation in the Drosophila oocyte. Development 129, 5473–5485.

Parton, R.M., Hamilton, R.S., Ball, G., Yang, L., Cullen, C.F., Lu, W., Ohkura, H., and Davis, I. (2011). A PAR-1–dependent orientation gradient of dynamic microtubules directs posterior cargo transport in the Drosophila oocyte. J. Cell Biol. 194, 121–135.

Pelletier, J., Field, C., Fürthauer, S., Sonnett, M., and Mitchison, T. (2020). Co-movement of astral microtubules, organelles and F-actin suggests aster positioning by surface forces in frog eggs. BioRxiv doi: 10.1101/2020.06.17.154260.

Pfender, S., Kuznetsov, V., Pleiser, S., Kerkhoff, E., and Schuh, M. (2011). Spire-type actin nucleators cooperate with Formin-2 to drive asymmetric oocyte division. Curr. Biol. 21, 955–960.

Pieuchot, L., Lai, J., Loh, R.A., Leong, F.Y., Chiam, K.-H., Stajich, J., and Jedd, G. (2015). Cellular Subcompartments through Cytoplasmic Streaming. Dev. Cell 34, 410–420.

Pinot, M., Steiner, V., Dehapiot, B., Yoo, B.-K., Chesnel, F., Blanchoin, L., Kervrann, C., and Gueroui, Z. (2012). Confinement induces actin flow in a meiotic cytoplasm. Proc. Natl. Acad. Sci. USA. 109, 11705–11710.

Prodon, F., Chenevert, J., and Sardet, C. (2006). Establishment of animal-vegetal polarity during maturation in ascidian oocytes. Dev. Biol. 290, 297–311.

Prodon, F., Sardet, C., and Nishida, H. (2008). Cortical and cytoplasmic flows driven by actin microfilaments polarize the cortical ER-mRNA domain along the a-v axis in ascidian oocytes. Dev. Biol. 313, 682–699.

Quinlan, M.E. (2016). Cytoplasmic Streaming in the Drosophila Oocyte. Annu. Rev. Cell Dev. Biol. 32, 173–195.

Roostalu, J., Rickman, J., Thomas, C., Nédélec, F., and Surrey, T. (2018). Determinants of Polar versus Nematic Organization in Networks of Dynamic Microtubules and Mitotic Motors. Cell 175, 796-808.

Sakamoto, R., Tanabe, M., Hiraiwa, T., Suzuki, K., Ishiwata, S., Maeda, Y.T., and Miyazaki, M. (2020). Tug-of-war between actomyosin-driven antagonistic forces determines the positioning symmetry in cell-sized confinement. Nat. Commun. 11, 3063.

Sanghvi-Shah, R., and Weber, G.F. (2017). Intermediate Filaments at the Junction of Mechanotransduction, Migration, and Development. Front. Cell Dev. Biol. 5, 81.

Schuh, M. (2011). An actin-dependent mechanism for long-range vesicle transport. Nat. Cell Biol. 13, 1431–1436.

Schuh, M., and Ellenberg, J. (2008). A new model for asymmetric spindle positioning in mouse oocytes. Curr. Biol. 18, 1986–1992.

Serbus, L.R., Cha, B.-J., Theurkauf, W.E., and Saxton, W.M. (2005). Dynein and the actin cytoskeleton control kinesin-driven cytoplasmic streaming in Drosophila oocytes. Development 132, 3743–3752.

Serwane, F., Mongera, A., Rowghanian, P., Kealhofer, D.A., Lucio, A.A., Hockenbery, Z.M., and Campàs, O. (2017). In vivo quantification of spatially varying mechanical properties in developing tissues. Nat. Methods 14, 181–186.

Shamipour, S., Kardos, R., Xue, S.-L., Hof, B., Hannezo, E., and Heisenberg, C.-P. (2019). Bulk Actin Dynamics Drive Phase Segregation in Zebrafish Oocytes. Cell 177, 1463-1479.

Sulerud, T., Sami, A.B., Li, G., Kloxin, A., Oakey, J., and Gatlin, J. (2020). Microtubule-dependent pushing forces contribute to long-distance aster movement and centration in Xenopus laevis egg extracts. Mol. Biol. Cell E20-01-0088.

Tang, S.K.Y., Renz, M., Shemesh, T., Driscoll, M., and Lippincott-Schwartz, J. (2018). Cytoplasmic self-organization established by internal lipid membranes in the interplay with either actin or microtubules. BioRxiv doi: 10.1101/506436.

Tanimoto, H., Kimura, A., and Minc, N. (2016). Shape-motion relationships of centering microtubule asters. J. Cell Biol. 212, 777–787.

Tran, P.T., Marsh, L., Doye, V., Inoué, S., and Chang, F. (2001). A mechanism for nuclear positioning in fission yeast based on microtubule pushing. J. Cell Biol. 153, 397–411.

Vasquez, D.L., Rodriguez-Lukey, K., Behura, S.K., and Balboula, A.Z. (2020). Cytoplasmic Microtubule Organizing Centers Regulate Meiotic Spindle Positioning in Mouse Oocyte. BioRxiv doi: 10.1101/2020.06.25.172684.

Verde, F., Dogterom, M., Stelzer, E., Karsenti, E., and Leibler, S. (1992). Control of microtubule dynamics and length by cyclin A- and cyclin B-dependent kinases in Xenopus egg extracts. J. Cell Biol. 118, 1097–1108.

Weber, K.L., and Bement, W.M. (2002). F-actin serves as a template for cytokeratin organization in cell free extracts. J. Cell Sci. 115, 1373–1382.

Weber, S.C., Spakowitz, A.J., and Theriot, J.A. (2012). Nonthermal ATP-dependent fluctuations contribute to the in vivo motion of chromosomal loci. Proc. Natl. Acad. Sci. USA. 109, 7338–7343.

Wolke, U., Jezuit, E.A., and Priess, J.R. (2007). Actin-dependent cytoplasmic streaming in C. elegans oogenesis. Development 134, 2227–2236.

Wühr, M., Tan, E.S., Parker, S.K., Detrich, H.W., and Mitchison, T.J. (2010). A model for cleavage plane determination in early amphibian and fish embryos. Curr. Biol. 20, 2040–2045.

Xie, J., and Minc, N. (2020). Cytoskeleton Force Exertion in Bulk Cytoplasm. Front. Cell Dev. Biol. 8, 69.

Yi, K., Unruh, J.R., Deng, M., Slaughter, B.D., Rubinstein, B., and Li, R. (2011). Dynamic maintenance of asymmetric meiotic spindle position through Arp2/3-complex-driven cytoplasmic streaming in mouse oocytes. Nat. Cell Biol. 13, 1252–1258.

Yi, K., Rubinstein, B., Unruh, J.R., Guo, F., Slaughter, B.D., and Li, R. (2013). Sequential actin-based pushing forces drive meiosis I chromosome migration and symmetry breaking in oocytes. J. Cell Biol. 200, 567–576.

Zalokar, M., and Erk, I. (1976). Division and migration of nuclei during early embryogenesis of Drosophila. J. Microsc. Biol. Cell 25, 97–106.

Zhao, P., Teng, X., Tantirimudalige, S.N., Nishikawa, M., Wohland, T., Toyama, Y., and Motegi, F. (2019). Aurora-A Breaks Symmetry in Contractile Actomyosin Networks Independently of Its Role in Centrosome Maturation. Dev. Cell 49, 651–653.

Zhao, T., Graham, O.S., Raposo, A., and St Johnston, D. (2012). Growing microtubules push the oocyte nucleus to polarize the Drosophila dorsal-ventral axis. Science 336, 999–1003.

Zumdieck, A., Kruse, K., Bringmann, H., Hyman, A.A., and Jülicher, F. (2007). Stress generation and filament turnover during actin ring constriction. PloS One 2, e696.

Acknowledgements

We would like to thank Justine Renno for illustrations, and Edouard Hannezo and members of the Heisenberg group for their comments on previous versions of the manuscript.

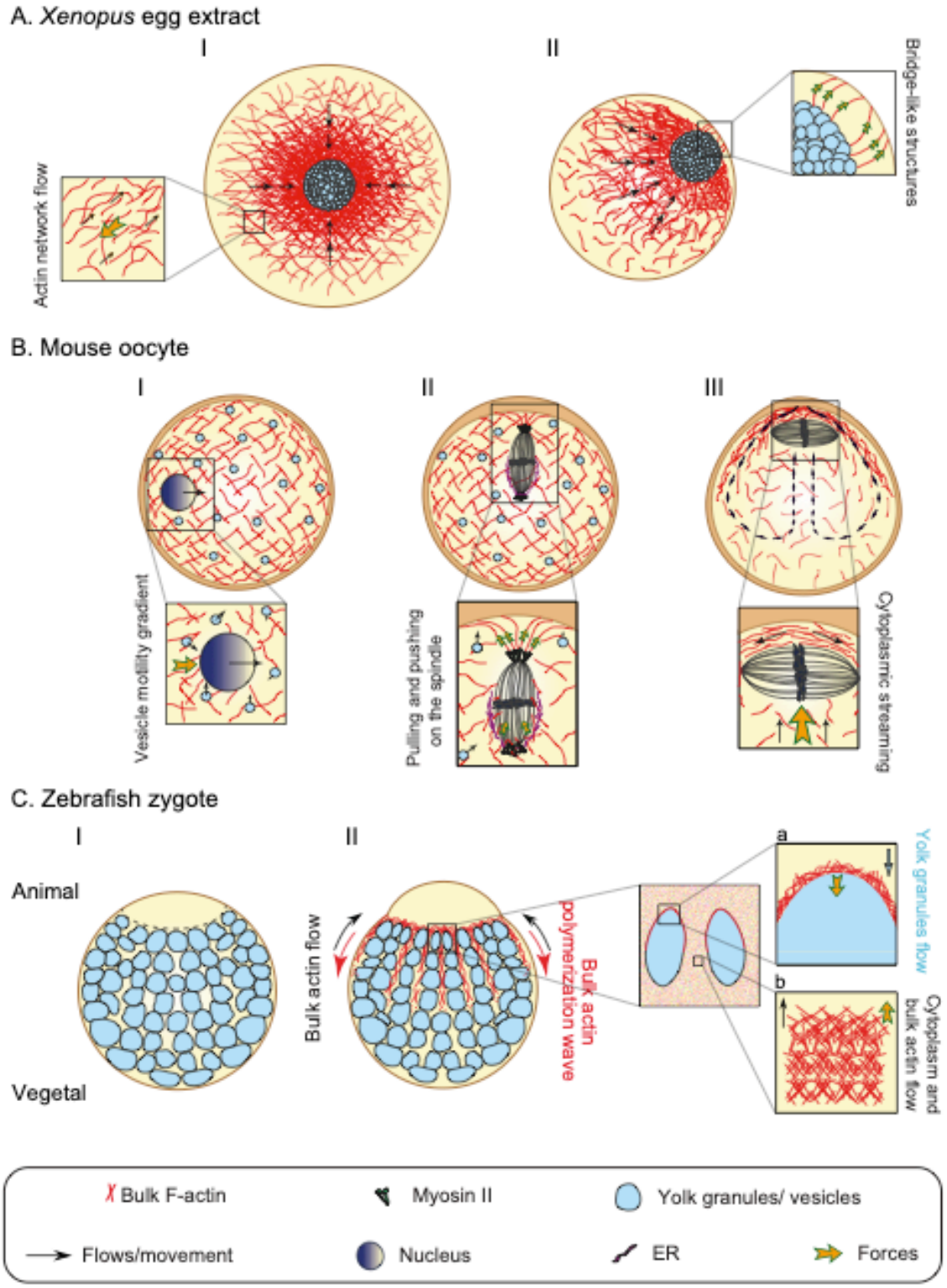

Figure 1. Actomyosin-mediated large-scale reorganizations in extracts, oocytes and zygotes. (A) Organelle positioning in encapsulated *Xenopus* egg extracts. Modified from (Ierushalmi et al., 2020; Sakamoto et al., 2020). Larger capsules position the organelles in their center (I), smaller capsules to their periphery (II). Center-ward actomyosin flows lead to organelle centering (I and inset), while bridge-like structures connecting organelles to the surface determine their asymmetric positioning (II and inset).

(B) Nucleus and spindle positioning in mouse oocytes. Modified from (Almonacid et al., 2015; Holubcová et al., 2013; Li et al., 2008; Schuh and Ellenberg, 2008; Yi et al., 2011). Nucleus centering in mouse oocytes is instructed by a gradient of vesicle motility (I and inset). Spindle migration towards the cortex depends on pulling and pushing forces: Rab11a vesicles and their associated actin networks, preferentially moving towards the cortex, take the spindle along. Myosin II-mediated pulling forces on this actin network further pulls on the spindle. In addition, actin comets polymerizing on the ER structures surrounding the spindle exert pushing forces on the spindle (II and inset). Arp2/3 complex-mediated bulk actin flows orchestrate cytoplasmic flows, which in turn push the spindle towards the cortex (III and inset).
(C) Cytoplasm-yolk granules segregation in zebrafish zygotes. Modified from (Shamipour et al., 2019). Zebrafish zygotes contain a mixture of cytoplasm and yolk granules, which prior to cytoplasmic flows are mixed across the zygote (I). During cytoplasmic streaming a bulk actin polymerization wave, travelling from the animal pole towards the vegetal pole, establishes bulk actomyosin flows towards the animal pole, dragging the cytoplasm along (II-inset b) and exerts pushing forces on yolk granules in the opposite direction (II-inset a).

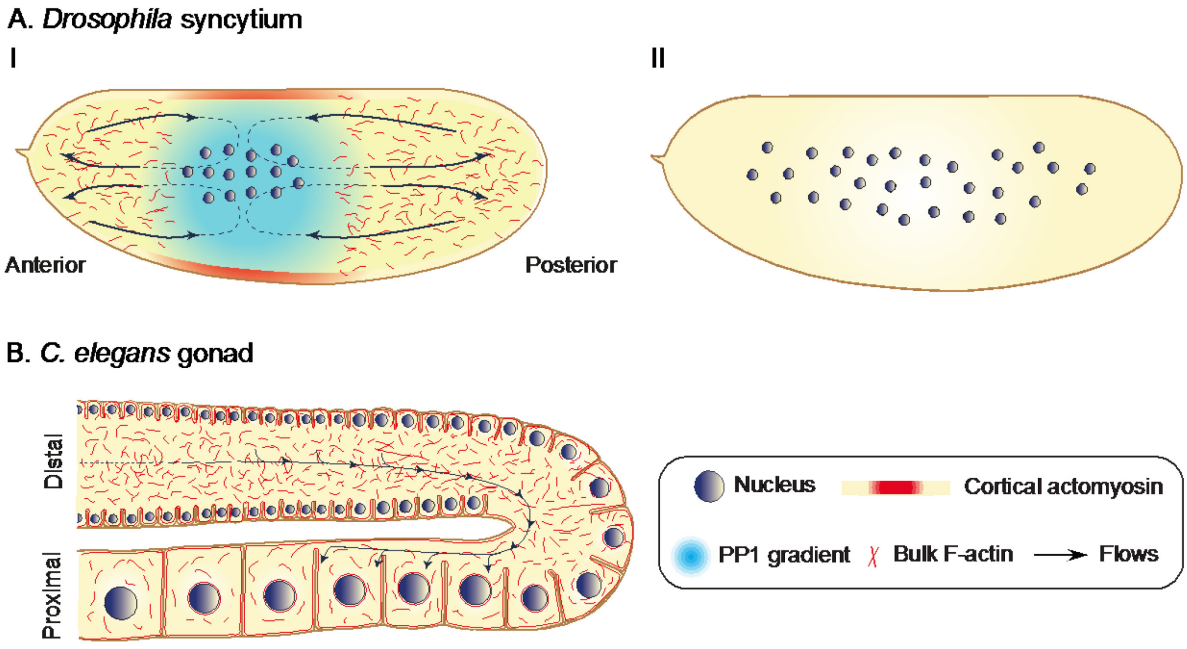

Figure 2. Actomyosin-mediated large-scale reorganizations in syncytia.
(A) Nuclear spreading in *Drosophila* blastoderm syncytium during (I) and after (II) axial expansion. Modified from (von Dassow and Schubiger, 1994; Deneke et al., 2019). Cortical flows of actomyosin towards the region where myosin II levels peak, drag along the surface cytoplasm, which then results in cytoplasmic back flows in the center of the embryo, distributing the nuclei along the anterior-posterior axis (Deneke et al., 2019). In addition, the nuclei positioned in the anterior half of the embryo were proposed to dissolve the surrounding bulk actin network, thereby generating a bulk actin network gradient peaking at the anterior and posterior poles, which might also contribute to nuclei redistribution along the AP axis (von Dassow and Schubiger, 1994).
(B) Distal-to-proximal cytoplasmic streaming in the *C. elegans* gonad. Modified from (Wolke et al., 2007).

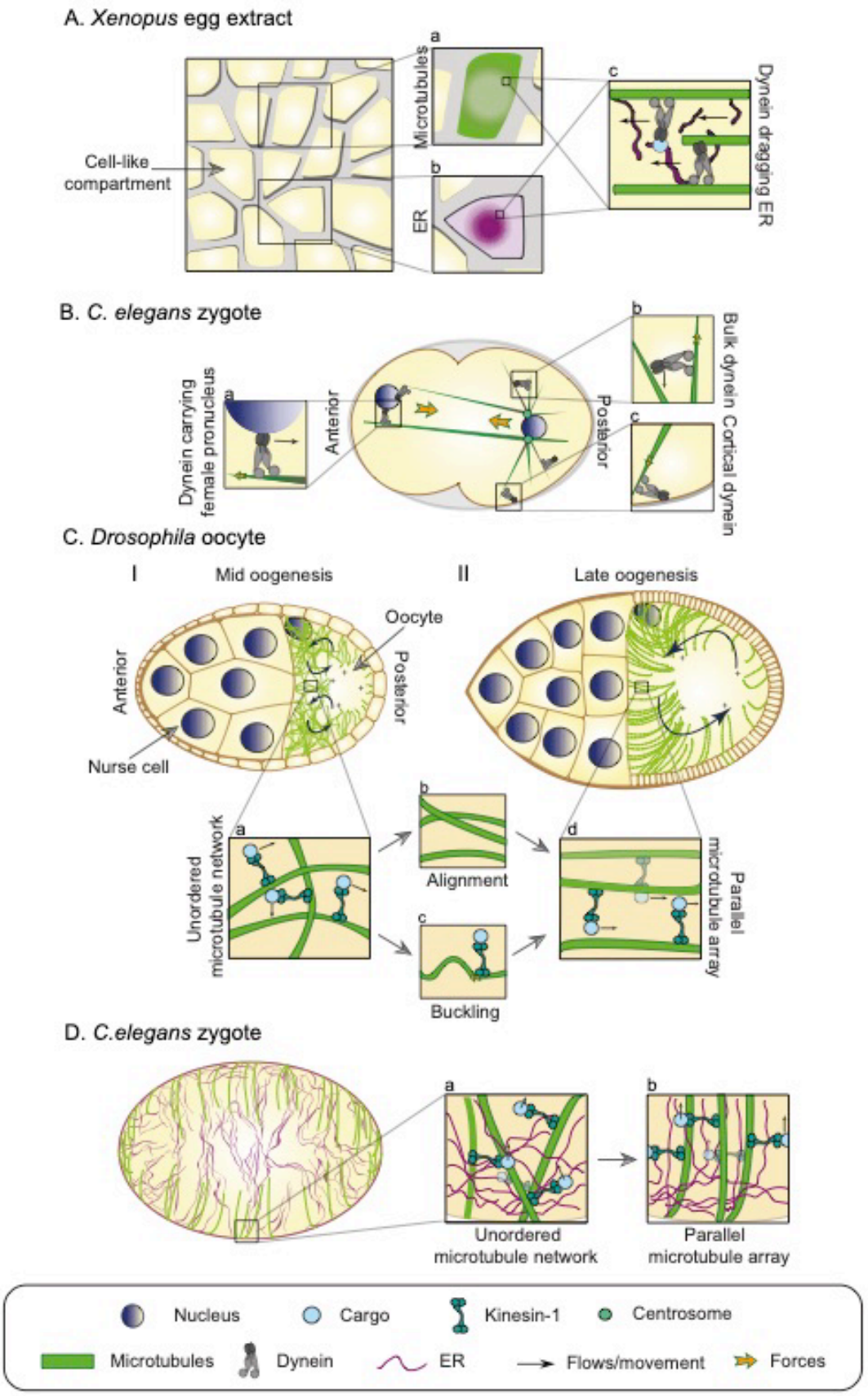

Figure 3. Microtubule-mediated large-scale reorganizations in extracts, oocytes and zygotes.
(A) Homogenized *Xenopus* egg extracts compartmentalized into cell-like compartments (left). Modified from (Cheng and Ferrell, 2019). Microtubules appear at the periphery (inset a) and ER structures position

at the interior (inset b). Dynein motors move towards the compartment center, taking along ER and other cargos (inset c).
(B) Male and female pronuclei migration in *C.elegans* zygote. Modified from (De Simone et al., 2018). Forces originating from dynein motors located at the cortex (inset c), in the cytoplasm (inset b) and on the female pronuclear envelope (inset a) pull on the microtubule asters, and female and male pronuclei, thereby collectively driving their centering.
(C) Cytoplasmic streaming in *Drosophila* oocytes. Modified from (Monteith et al., 2016; Quinlan, 2016). Oocytes exhibit slow cytoplasmic streaming at mid stages of oogenesis (I) and fast cytoplasmic streaming at late stages of oogenesis (II). Microtubule network appears initially random (inset a). The movement of kinesin-1 motors carrying cargos along this network of microtubules generates viscous drag forces to the cytoplasm resulting in microtubule alignment (inset b). The compressive forces by motors on microtubule filaments can lead to microtubule buckling (inset c). These forces collectively lead to microtubule alignment, resulting in large-scale cytoplasmic flows (inset d).
(D) Cytoplasmic streaming in *C.elegans* oocytes. Modified from (Kimura et al., 2017). Kinesin-1 motors carrying cargos such as ER along a random network of microtubules (inset a) create viscous drag forces to the cytoplasm, which in turn results in microtubule alignment (inset b).

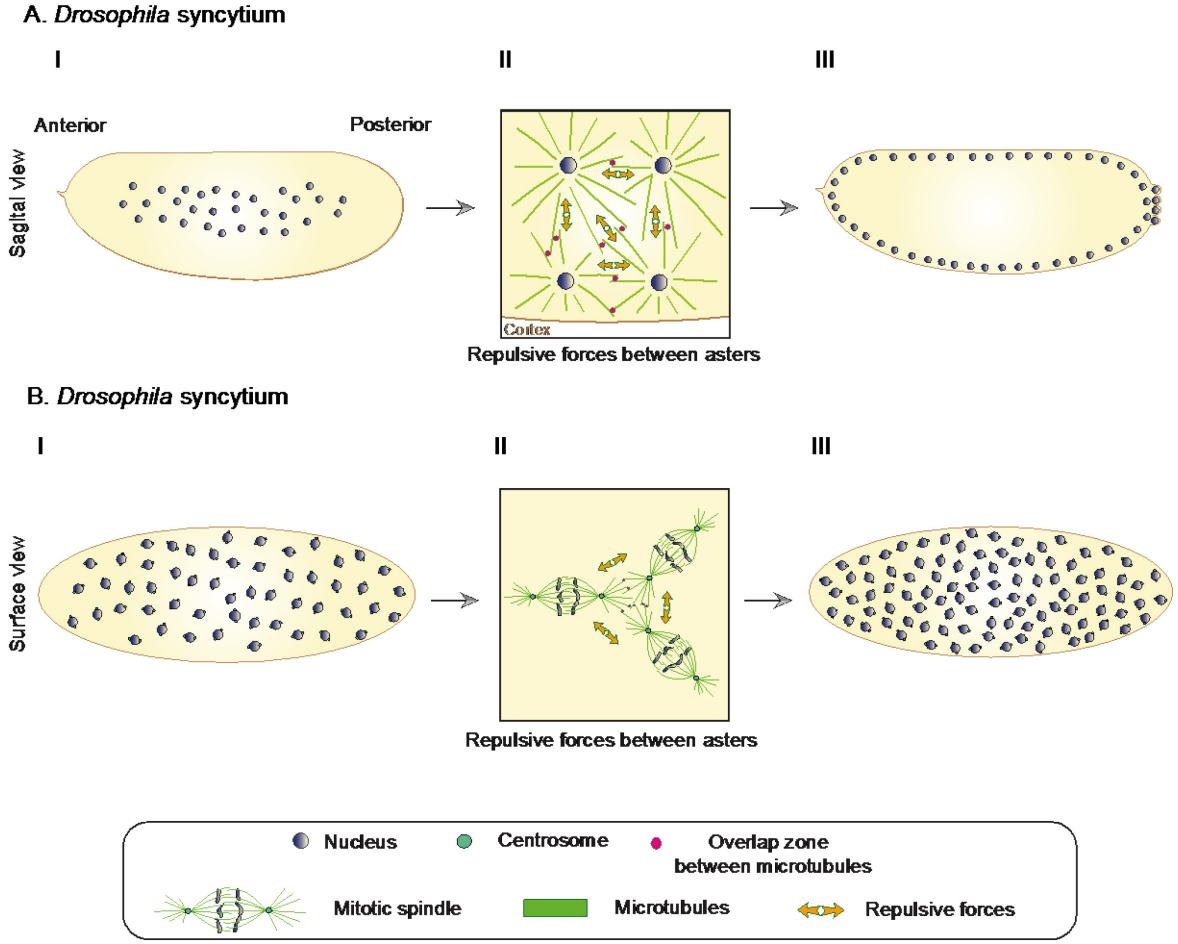

Figure 4. Microtubule-mediated large-scale reorganizations in syncytia.
(A) Nuclear migration in the *Drosophila* syncytial blastoderm. Modified from (Baker et al., 1993). Nuclei relocalization from the interior of the embryo (I: cycle 7) towards the cortex (III: cycle 9) relies on pushing forces between interphase asters (II).
(B) Nuclei maintain a uniform spacing during last syncytial nuclear divisions (I: cycle 10, III: cycle 11). Modified from (Deshpande et al., 2019). Pushing forces between astral microtubules are thought to repulse neighboring asters and thereby define mitotic spindle positioning and orientation (II).

1.2 Ascidian early development

1.2.1 Introduction

Ascidians are marine invertebrates that belong to a sister group of vertebrate animals (*Urochordata, Tunicata, Ascidiacea*). They can develop into tadpole larvae composed of less than 3000 cells and 6 different tissues[7]. The fertilized ascidian oocyte undergoes a stereotypical cleavage pattern such that by the beginning of gastrulation (at the 110-cell stage), the developmental fate of individual blastomeres can be identified[8]. The development of ascidians has long been regarded as the main example of mosaic development, in which the differential inheritance of maternal factors - localized to specific regions of cells - will determine the fate of each blastomere. Although it has been shown that cell-cell interactions are crucial in certain specification processes in ascidian embryonic development[7], segregation of maternal determinants - a hallmark of cytoplasmic reorganizations in oocytes and zygotes - is central to the proper establishment of embryonic axis and the first steps of cell specification. In the following sections we will outline the main known aspects of such reorganizations and how they lead to maternal determinants segregation.

There are several species of solitary ascidians used as model organisms in research and their embryonic development is almost identical between them. The work in this project was done using *Phallusia mammillata* (Fig. 1.1) as the model organism since the transparency of its embryos is a huge advantage for live imaging.

Fig. 1.1 – Phallusia mammillata. Photo credit: Benoit Godard.

1.2.2 Cytoplasmic reorganizations in the ascidian oocyte and early embryo

The ascidian oocyte and early embryo undergoes striking reorganizations of its cytoplasm and cytoplasmic domains in order to properly establish its future embryonic axis and pattern the embryo for the subsequent morphogenetic events. Here we summarize the current knowledge of such reorganizations from the first polarization event during oogenesis to the first cleavage.

1.2.2.1 Cytoplasmic reorganizations during oocyte maturation

In ascidian development the first embryonic axis to be established – the animal-vegetal (AV) axis – is specified during oogenesis (Fig. 1.2)[9].

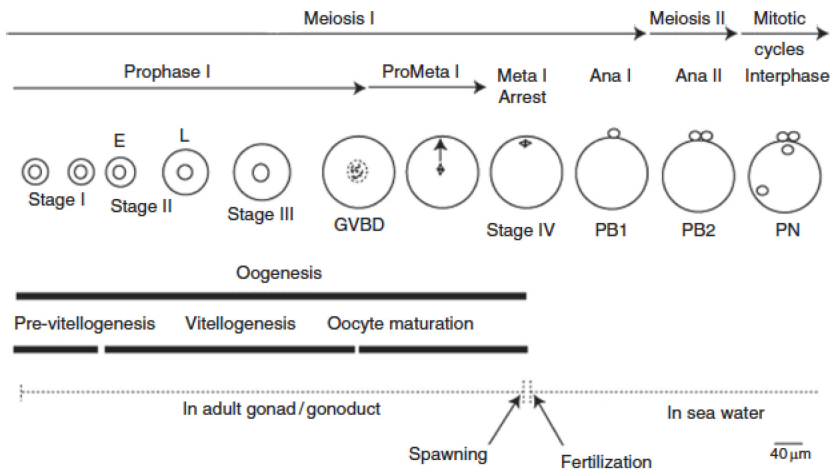

Fig. 1.2 – Ascidian meiotic maturation from oogenesis to meiosis completion after fertilization. Meiosis stages are shown on top. Germinal vesicle break down (GVBD), polar body (PB) and pronucleus (PN). Taken from[10].

Post-vitellogenic fully grown stage III oocytes of *Phallusia* and *Ciona* do not display any sign of polarity and the germinal vesicle (GV) is located in the center of the oocyte. A mitochondria-rich layer – called myoplasm – and the cortical endoplasmic reticulum (cER) and its associated mRNAs – termed *postplasmic/PEM* mRNAs in *Phallusia* and *Ciona* - are deposited under the plasma membrane all around the oocyte in a radially symmetric manner (Fig. 1.3.A)[9]. In *Ciona* a decrease in the levels of cAMP triggers GV breakdown and the meiotic spindle forms in the center of the oocyte[11]. A cloud of actin forms around the spindle and migrates with it towards a cortical region that becomes the animal pole (AP). The polarity cue that determines the direction of spindle migration in *Ciona* and *Phallusia* is unknown (Fig. 1.3.C). Once the spindle reaches the cortex, the cloud of actin disappears and a small bright cortical patch of actin forms surrounded by an area of local actin downregulation in the cortex immediately close to the spindle[9]. Spindle migration has been shown to be actin-dependent, however, the precise force-generating mechanism driving meiotic spindle migration in ascidians is not known.

Similarities with the mouse oocyte point to a parallel mechanism in which an actin cloud associated with the spindle breaks symmetry and exerts pushing forces on the spindle triggering its migration to the opposite cortex[12]. The specific way the actin cloud functions in ascidian oocytes remains to be studied.

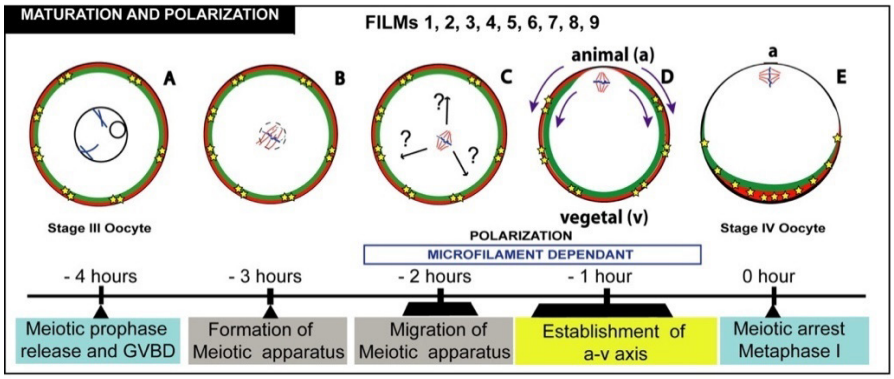

Fig. 1.3 – Cytoplasmic reorganizations during* Ciona *and* Phallusia *oogenesis. (**A**) Post-vitellogenic stage III oocyte with the cortical endoplasmic reticulum in red, myoplasm in green and maternal mRNAs represented by the yellow stars. (B) Germinal Vesicle Break Down. (C) Migration of the meiotic spindle to the cortex. (D) Initiation of the vegetal translocation of the myoplasm and the cortical endoplasmic reticulum. (E) Mature stage IV oocyte. The spindle marks the position of the animal pole. Taken from [13]***.***

Spindle migration and polarization of the actin cortex are the first signs of symmetry breaking in *Phallusia* and *Ciona* oocytes and are immediately followed by a clearance of the myoplasm and the *postplasmic/PEM* mRNAs away from the AP, eventually accumulating along the vegetal cortex, in a basket like manner (Fig. 1.3.D-E)[14]. Pharmacological treatments showed that the vegetal translocation of the myoplasm and the *postplasmic/PEM* mRNAs is actin-dependent[9].

Alternatively, in the oocyte of the species *Halocynthia roretzi* the GV is not centrally located but it appears close to the cortex (Fig. 1.4)[6]. Upon GVBD cortical and cytoplasmic flows are established in order to properly position the spindle close to the cortex. Similar to *Phallusia* and *Ciona* oocytes, the myoplasm and the *postplasmic/PEM* mRNAs eventually relocate to the vegetal cortex of the oocyte. Actin depolymerization and inhibition of myosin contractility severely affected both spindle migration and vegetal polarization of mitochondria and mRNAs, suggesting that actomyosin contractility functions in this process by establishing cortical and cytoplasmic flows that properly position the different cytoplasmic domains[6]. Yet, the precise mechanism that establishes and directs these flows and thus oocyte polarization remains to be demonstrated. Interestingly, AV polarization can be reversed in *Halocynthia roretzi*. Relocalization of the GV to the opposite pole of the oocyte by centrifugation induced repolarization along the AV axis and the reversal of the myoplasm localization suggesting that the AP is not fully specified in pre-GVBD oocytes[15].

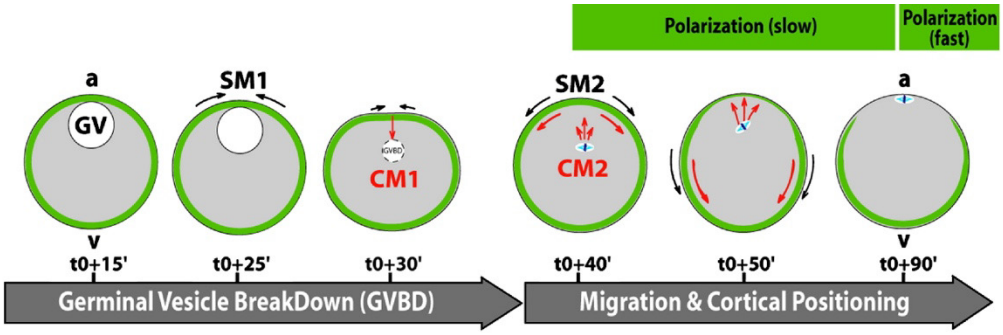

Fig. 1.4 – Cytoplasmic reorganizations during* Halocynthia *oogenesis. Schematic representation of the surface movements (SM, black arrows) and the cytoplasmic movements (CM, red arrows). Germinal vesicle (GV), a (animal) and v (vegetal). Myoplasm in green. Taken from [6].

Oocyte maturation ends with the stage IV oocyte arrested in metaphase I and ready to be fertilized[9]. Fertilization triggers a series events that have been grouped into the first and second phases of ooplasmic segregation (Fig. 1.5). Although both phases consist on several processes each, they are mainly driven by two molecular mechanisms: the first phase is dependent on actomyosin contractility and the second phase depends on microtubules[13]. Due to the transparency of *Phallusia mammillata* oocytes and embryos, most of the studies summarized here use this organism to study the dynamics of fertilization and early development, unless otherwise stated.

1.2.2.2 First phase of ooplasmic segregation

The stages of the first phase of ooplasmic segregation are depicted in Fig. 1.5.

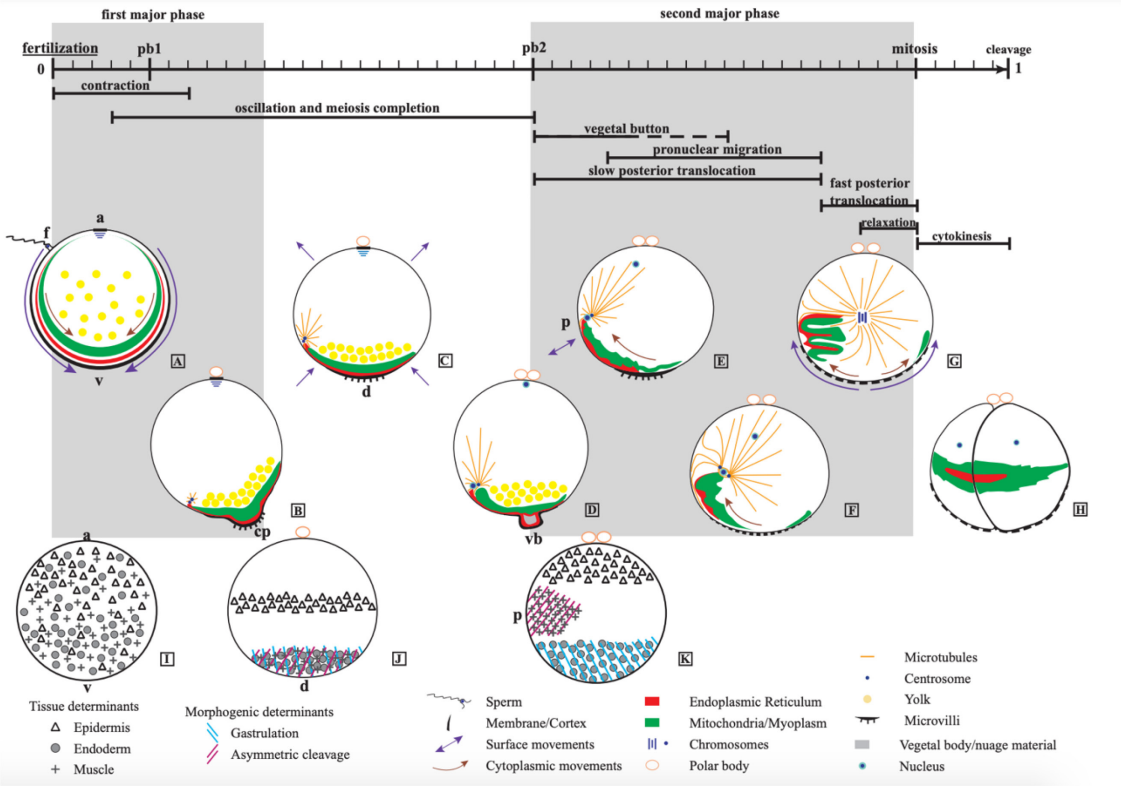

Fig. 1.5 – Phases of ooplasmic segregation upon fertilization. Time line of events in shown on top. The grey areas correspond to the first and second phases respectively. Segregation of maternal determinants is depicted in the bottom. Taken from[16].

When the metaphase-arrested mature oocyte is fertilized, a calcium wave is initiated from the point of sperm entry and travels along the oocyte to the opposite side[16]. The main role of this calcium wave is to activate the oocyte[17] and trigger meiosis I exit[17] . Following the calcium wave, a cortical contraction wave in the AV direction traverses the newly fertilized oocyte[18]. It has been proposed that the role of the cortical contraction is to accumulate the myoplasm, the cortical endoplasmic reticulum (cER) and the maternal *postplasmic/PEM* mRNAs at the vegetal pole in a protrusion called contraction pole (CP)[16]. The general AV directionality of the contraction is invariable and it has been suggested that a graded concentration of actin along the AV axis might be responsible for the overall directionality of the fertilization-induced contraction[14, 18]. Notably, the CP does not always form at the vegetal-most part of the cortex. It was proposed that the directionality of the calcium wave and therefore, the point of sperm entry, determines the position of the CP so that it can form up to 40-60° from the AV axis[18]. Together with the vegetal accumulation of cytoplasmic domains, the cortical contraction wave also leads to the vegetal translocation of the sperm nucleus and basal body that will orchestrate a series of fast calcium waves starting from the VP[19]. 7 minutes post fertilization,

the fast calcium oscillations pause, the first polar body is extruded at the AP and the CP eventually disappears[13]. This marks the end of the first phase of ooplasmic segregation.

1.2.2.3 Second phase of ooplasmic segregation

After the extrusion of the first polar body, small fast calcium waves are again originated from the VP. These calcium waves correlate with periodic fast contractions of the VP of the oocyte. Eventually, 25 minutes after fertilization the repetitive calcium waves cease and the second polar body is emitted, marking the beginning of the second phase of ooplasmic segregation (Fig. 1.4)[13].

At this time microtubule polymerization at the sperm aster makes it grow in size. Aster microtubules span the whole zygote and are used by female pronucleus to migrate towards the sperm aster. At the same time the sperm aster migrates along the vegetal cortex in the animal direction. The movement of the aster brings along the myoplasm and the *postplasmic/PEM* mRNAs attached to the cER. As the sperm aster starts migrating towards the center of the cell, vibrations are apparent in the vegetal pole. This is a reflection of the tensions that arise due to the motion of the aster away from the vegetal cortex and the cER-*postplasmic/PEM* mRNAs and myoplasm domains that are somehow attached to it[13]. Eventually both pronuclei leave the cortex and move towards the center of the zygote. This final migration induces a rupture of the myoplasm that splits in two portions. The final position of the aster in the cortex marks the posterior pole of the embryo[16].

Approximately 1 hour post fertilization, the zygote undergoes the first cleavage dividing along the future dorsal-ventral (DV) axis and separating the fertilized oocyte into right and left halves of the future tadpole. The second cleavage proceeds perpendicular to the first one and forms a flat 4-cell stage embryo with two anterior blastomeres and two posterior blastomeres, which contain the cER-*postplasmic/PEM* mRNAs and myoplasm domains. A third cleavage along the equator of the cells separates animal and vegetal blastomeres in the 8-cell stage embryo. The cER- *postplasmic/PEM* mRNAs and myoplasm domains are inherited by the vegetal posterior-most blastomeres[13] (Fig. 1.6).

1.2.3 Maternal determinant segregation during cytoplasmic reorganizations and their role in development

The main role of the cytoplasmic reorganizations in ascidians is to locate maternal factors in specific areas of the oocyte and early embryo. Their correct translocation is essential to ensure the appropriate cell interactions, the expression of zygotic genes during early development and cell fate specification. These maternal mRNAs are called *postplasmic/*PEM mRNAs because their accumulation at the vegetal posterior-most blastomeres of the 8-cell stage embryo defines the Posterior End Mark. These blastomeres concentrate cER-*postplasmic/PEM* mRNAs and form the Centrosome Attracting Body (CAB) that induces the eccentric positioning of the spindle during the subsequent 3 cleavages thus directing 3 rounds

of unequal cell division[20]. At the 64-cell stage, the cER-*postplasmic/PEM* mRNAs domain is inherited by 2 micromeres at the posterior of the embryo.

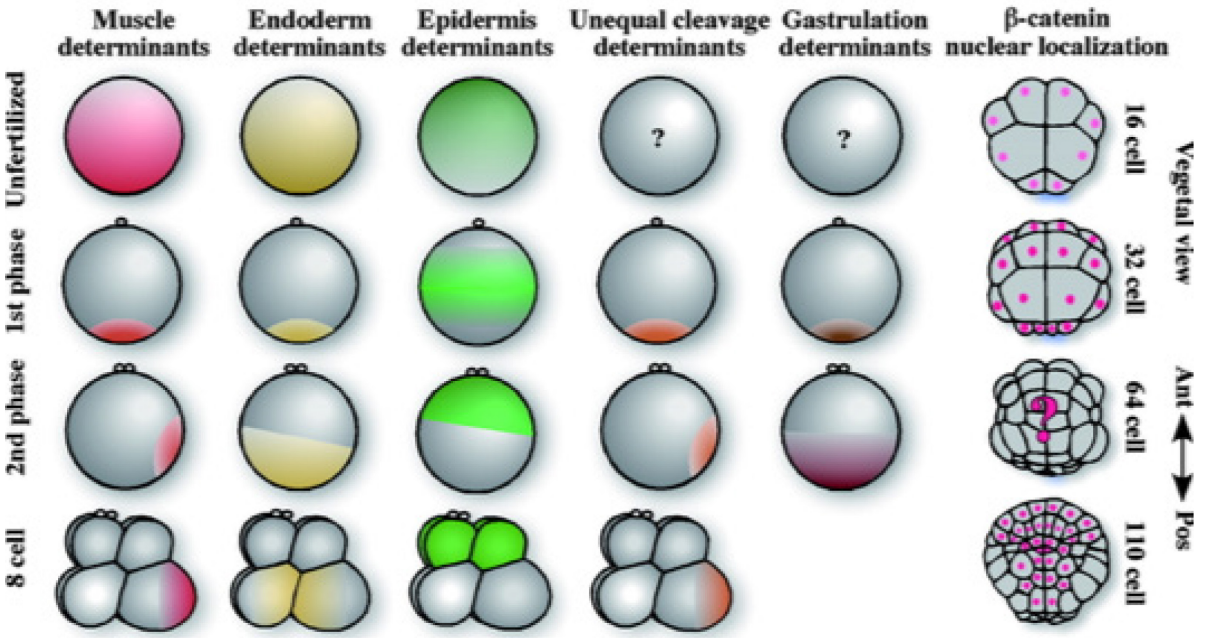

Fig. 1.6 – Segregation of maternal determinants and axis specification in ascidians. Schematic representation of the known localization of muscle, endoderm, epidermis, unequal cell division and gastrulation determinants from the unfertilized oocyte (top) to the 8-cell stage (bottom). Right column shows the nuclear accumulation of ß-catenin from the 16-cell stage until the beginning of gastrulation (110-cell stage). Adapted from[21].

There are more than 40 *postplasmic/PEM* mRNAs identified[20]. The fertilization-induced cortical contraction drives maternal determinants for mesoderm (muscle) and endoderm fates and morphogenetic determinants (gastrulation and unequal cleavage) to accumulate at the CP whereas ectoderm determinants remain at the animal hemisphere of the zygote (Fig. 1.6)[21]. After the second phase only the mesoderm and unequal cleavage determinants are translocated to the posterior pole, leaving the endoderm and gastrulation determinants at the VP (Fig. 1.6). Seminal studies by Nishida in *Halocynthia roretzi* led to the establishment of the accumulation pattern of the *postplasmic/PEM* mRNAs[22-23]. Removal of the CP after the first phase of ooplasmic segregation or the VP after the second phase from zygotes gave rise to radially symmetric embryos that lacked vegetal cell fates, namely, endoderm, mesoderm and notochord. Moreover, these embryos failed to gastrulate. Interestingly, if the ablated cytoplasm was transplanted at the AP of a VP-ablated embryo, gastrulation started at the transplantation site, suggesting that the gastrulation determinant accumulates at the CP after the first phase of ooplasmic segregation[22].

Nishida also ablated the posterior vegetal cortex right before the first cell cleavage. In this case, embryos gastrulated normally but they were radialized along the AV axis and showed no anterior-posterior specification. Transplantations of the ablated portion of the zygote into

the anterior-vegetal region of ablated embryos reversed the anterior-posterior axis suggesting that the determinants that are translocated to the posterior pole are able to inhibit the anterior cell fates[23]. These set of ablations demonstrate that gastrulation determinants remain at the VP after the first phase of ooplasmic segregation.

1.3 Aims of the thesis

The functional studies carried out by Nishida[22-23] highlight the importance of ooplasmic segregation in ascidian early embryonic development by establishing the embryonic axis and patterning the embryo before gastrulation.

Although the series of events that take place in each phase of ooplasmic segregation have been very well described[14, 16, 18], a mechanistic explanation of the force-generating mechanisms and how these forces are transmitted in order to reorganize cytoplasmic domains in such a spectacular manner is still lacking. Here we focused on the first phase of ooplasmic segregation. We analyzed the cellular deformations that arise in the oocyte upon fertilization and the role of the cytoskeleton in mediating them.

2. MATERIALS AND METHODS

2.1 Key resource table

REAGENT or RESOURCE	SOURCE	IDENTIFIER
Antibodies		
Anti-neurofilament 160 mouse Monoclonal Antibody	Sigma-Aldrich	Cat# N5264, RRID:AB_477278
Anti-phospho-S6 Ribosomal Protein (Ser235/236) rabbit Polyclonal Antibody	Cell Signaling Technology	Cat# 2211, RRID:AB_331679
Alexa Fluor 488 goat anti-mouse IgG (H+L)	Molecular Probes	Cat#A-11029; RRID: AB_138404
Alexa Fluor 546 goat anti-rabbit IgG (H+L)	Molecular Probes	Cat#A-11010; RRID: AB_143156
Chemical, Peptides, and Recombinant Proteins		
Tropic Marin® BIO-ACTIF Sea Salt	Tropic Marine	N/A
Nocolodazole	Sigma-Aldrich	Cat # M1404; CAS:31430-18-9
Latrunculin B	Sigma-Aldrich	Cat# 428020; CAS: 76343-94-7
Ficoll® PM400	Sigma-Aldrich	Cat# F4375; CAS: 26873-85-8
Gelatin from Bovin Skin	Sigma-Aldrich	Cat# G9391; CAS: 9000-70-8
Trypsin from Bovine Pancreas	Sigma-Aldrich	Cat# T8003; CAS: 9002-07-7
MitoTracker™ Deep Red FM	Invitrogen	Cat# M22426
Calcium Green	Invitrogen	Cat# C3713
mMESSAGE mMACHINE T3 Transcription Kit	Invitrogen	Cat # AM1343
MY-134	MY Polymers	Cat# MY-134
Experimental Model		
Phallusia mammillata	EMBRC - Roscoff Marine Station, France	https://embrc-france.obs-banyuls.fr/en/
Recombinant DNA		
pSPE3-Utrophin-Venus	Gift from Alex McDougall (Sorb Université/CNRS)	N/A
pSPE3-Utrophin-mCherry	Gift from Alex McDougall (Sorb Université/CNRS)	N/A
pSPE3-iMyo-YFP	Gift from Edwin Munro (Universit Chicago)	N/A
pSPE3-iMyo-mScarlet	This study	N/A
pSPE3-iMyo-mKO	This study	N/A
pCS2-caMypt	Weiser et al., 2009[24]	N/A

Software and Algorithms		
Fiji	Schindelin et al., 2012[25]	https://fiji.sc/
Imaris	Bitplane	https://imaris.oxinst.com/packages
Ilastik	Sommer et al., 2011[26]	https://www.ilastik.org/
Excel	Microsoft	https://products.office.com/en-us/?rtc=1
GraphPad Prism	GraphPad Software	https://www.graphpad.com/scientific-software/prism/
PIVlab	Thielicke and Stamhuis 2014[27]	https://pivlab.blogspot.com/
MATLAB	MATAB Software	https://www.mathworks.com/products/matlab.html
Python 3.0		http://www.python.org

2.2 Animal maintenance and embryo handling

Adult *Phallusia mammillata* were purchased from Roscoff Marine Station (EMBRC, France) and kept in artificial sea water (ASW) aquariums at 16°C for 3-4 weeks under constant light to prevent spawning. All embryo manipulations and experiments were carried out at 16 °C. Oocytes and sperm were obtained after animal dissection and kept at 4 °C for 3-4 days. Oocytes were chemically dechorionated in a 1% trypsin solution in ASW for 50 min to 1 h under gentle stirring and washed 5 times and kept in ASW supplemented with 0.05 g/l streptomycin sulfate salt.

For fertilization, sperm was activated by resuspending 1 ul of dry sperm in 1 ml of pH 9 ASW. Oocytes were then fertilized under the corresponding microscope.

2.3 Cloning of expression constructs

Gateway technology and Gibson assembly was used to generate the expression constructs[28].

pSPE3-iMyo-mScarlet
Gibson assembly was used to create a new destination vector (pSPE3-R1-RfA-R3). The backbone for the new destination vector was amplified using the following primers: 5'-TATACATAGTTGGATAAACTTAGATATCGCGGCCG-3' and 5'- GTCACTATGGTCGACCTGCAGAC-3' from the vector pSPE3-RfA[29], a gift from Lemaire Lab. The R3 arm of the new destination vector was amplified from pDEST™R4-R3 using the following primers: 5'-AGGTCGACCATAGTGACTGGATATGTTGTGTTTTACAGTATTATGT-3' and 5'-ATCTAAGTTTATCCAACTATGTATAATAAAGTTGAACGAGAAACGTAAAATGA-3'. PCR fragments were assembled following the one-step Gibson assembly protocol.

The following primers with gateway arms were used to amplify the coding region for mScarlet from the vector Bra>iMyo-mScarlet (a gift from Munro Lab, University of Chicago): 5'-GGGGACAGCTTTCTTGTACAAAGTGGCTATGGTGAGCAAGGGCGAGG-3' and 5'-GGGGACAACTTTGTATAATAAAGTTGCTTACTTGTACAGCTCGTCCATGCCG-3'. The PCR product was used to generate an entry vector using the pDONRP-P2r-P3. The following primers with gateway arms were used to amplify the coding region for iMyo from the vector Bra>iMyo-mScarlet: 5'-GGGGACCACTTTGTACAAGAAAGCTGGGTAACCTAGGACGGTCAGCTTGG-3' and 5'-GGGGACAAGTTTGTACAAAAAACAGGCTTAATGGCCGAGGTGCAGCT-3'. PCR product was used to generate an entry vector (p5M-iMyo) using the pDONRP221. Entry vectors were further recombined with the destination vector pSPE3-R1-RfA-R3.
Cloning was performed by David Labrousse-Arias.

pSPE3-iMyo-mKO
The following primers with gateway arms were used to amplify the coding region for mKO from the vector mKOkappa-2A-mTurquoise2[30] (a gift from a gift from Dorus Gadella; Addgene plasmid #98837 ; http://n2t.net/addgene:98837 ; RRID:Addgene_98837): 5'-GGGGACAGCTTTCTTGTACAAAGTGGTAGGCGAGGAGAGTGTGATTAAACC-3' and 5'-GGGGACAACTTTGTATAATAAAGTTGTTCGCCAGTGGAATGAGCTACT-3'. The PCR product was used to generate a p3M-mKO entry vector via recombination with pDONR-P2rP3. p3M-mKO, p5M-iMyo and pSPE3-R1-RfA-R3 were recombined to generate the expression construct.
Cloning was performed by Irene Steccari.

2.4 mRNA microinjections

Microinjections were performed as previously described with some modifications[31]. Microinjection needles (1B100-4, World Precision Instruments) were pulled with a P-97 needle puller (Sutter Precision Instruments) and mounted on a microinjection setup (Narishige) under an Olympus SZX16 stereomicroscope. Oocytes were placed in agarose circular wells made from homemade PDMS pillar microarray[32]. *In vitro* mRNA transcription was performed with the mMESSAGE mMACHINE T3 Transcription Kit. Purified mRNAs were injected in dechorionated unfertilized oocytes at 1 – 1.5 μg/μl the evening before the experiments except for CaMypt mRNA that was injected 3 to 4 h prior to the experiment.

2.5 Myoplasm labelling

Dechorionated unfertilized oocytes were incubated in 1 μM solution of MitoTracker™ Deep Red FM in ASW for 5 min and washed in ASW prior to fertilization.

2.6 Cytoskeletal inhibitors

For actin and microtubule inhibition, unfertilized oocytes were incubated in Latrunculin B (1 μg/μl) and Nocodazole (0.6 μM) for 10 minutes prior to fertilization.

2.7 Confocal live imaging

For live imaging unfertilized oocytes were mounted in transparent microwells as in[32]. Briefly, in a MaTek dish (P35G-1.5-14-C, MatTek) a PDMS stamp with micropillars of different sizes (Fig. 2.1) was pressed onto a small drop of MY-134, a polymer with a refracting index matching water's. Then it was purged in nitrogen for 5 minutes and placed under 365nm UV light in a nitrogen box for 15 minutes. Next, it was cured an additional 1 hour and 45 minutes without nitrogen flow. We use a beam expanded 100 mW UV LED M365L2-C1 (Thorlabs, Germany) at approximately 1 mW/cm^2. Then the PDMS stamp was peeled out and the microwells coated with 1% gelatin from bovine skin. The design and preparation of the microwells was performed by Jack Merrin from the Nanofabrication Facility at IST Austria.

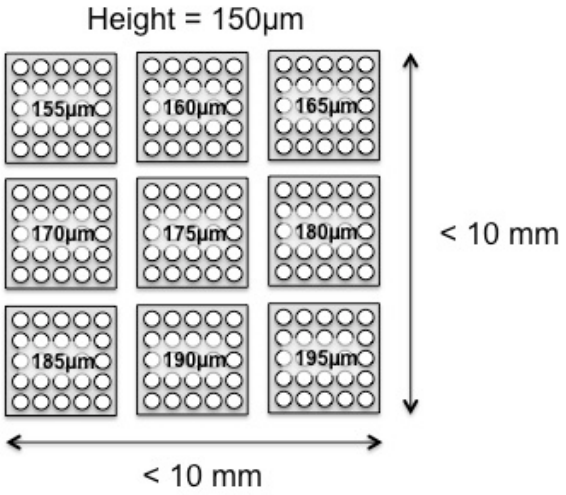

Fig. 2.1 – Design of the microwells used to mount ascidian oocytes for imaging. Design of the silicon wafer for the PDMS stamp and fabrication of the wells was done by Jack Merrin from the Nanofabrication Facility at IST Austria.

For confocal imaging, oocytes were imaged in an inverted Leica TCS SP5 confocal microscope equipped with a HC PL APO CS2 40x/1.10 NA water immersion objective (Leica) and resonant scanner. Temperature was kept constant during image acquisition at 16 °C using a cooling stage (Fig. 2.2) fabricated by the Machine Shop at IST Austria. The whole oocyte was imaged with an optical section thickness of 3 μm every 16 – 20 seconds.

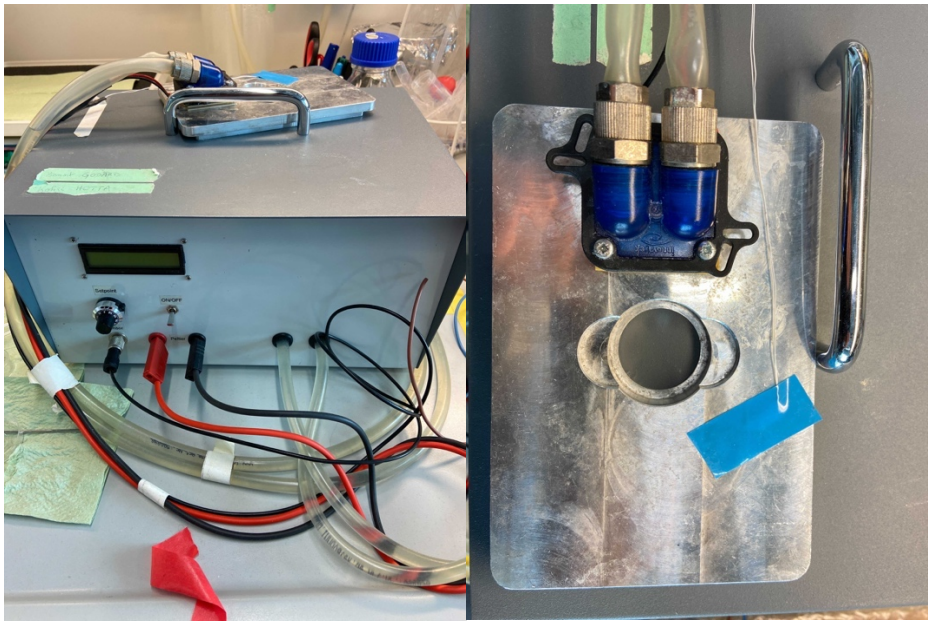

Fig. 2.2 – Custom-made cooling stage. Frontal view of the cooling system and top view of the stage inset used for keeping the temperature constant during imaging. Design and fabrication was done by the Machine Shop at IST Austria.

2.8 Micropipette aspiration experiments

2.8.1 Cortical tension in unfertilized oocyte

Cortical tension measurements of unfertilized oocytes was performed following previously established protocols[32-34]. Unfertilized dechorionated oocytes were placed in a gelatin-coated MaTek dish (P50G-0-14-F, MatTek) on an inverted Leica TCS SP5 microscope equipped with a home-made cooling stage (see section 2.7).

Blunt, fire-polished and passivated with heat-inactivated FBS (Sigma-Aldrich) micropipettes with a 20 μm inner diameter (Biomedical Instruments) and a 30° bent angle were controlled by micromanipulators (TransferMan Nk2, Eppendorf) and positioned at the cortex of animal or vegetal poles of unfertilized oocytes. A negative pressure was applied with an increment of 10 Pa using a Microfluidic Flow Control System Pump (Fluiwell, Fluigent) and the Dikeria micromanipulation software. Images were acquired every second. The length of the deformation inside the pipette was measured using a customized Fiji macro and plotted over time. Cortical (or surface) tension (T_c) was calculated using the Young-Laplace equation:

$$T_c = \frac{P_c}{2\left(\frac{1}{R_p} - \frac{1}{R_c}\right)}$$

P_c is the critical pressure reached when the deformation inside the pipette is equal to the pipette radius (R_p), R_c is the radius of the oocyte and was measured from the initial aspiration time-point using Fiji software.

2.8.2 Cortical tension in fertilized oocytes

Cortical tension changes upon fertilization were monitored using a slight modification of the methodology explained in the previous section. Briefly, micropipettes were placed at the animal and vegetal poles of unfertilized oocytes and a negative pressure was applied until the deformation in the pipette reached its radius (30 Pa and 45 Pa for animal and vegetal poles respectively). The oocyte was then fertilized and the aspirated pressure was modified accordingly in order to maintain the length of the deformation inside the pipette constant over time. Fertilization time-point was identified by injection of Calcium Green. The aspirating pressure was monitored over time and used to calculate the cortical tension during the duration of the experiment as explained in the previous section.

Blunt, 30° bent angle, passivated with heat-inactivated FBS micropipettes with an inner diameter 40 μm were used instead in order to avoid bleb-like events during the long aspirations.

2.8.3 Viscosity measurement in unfertilized oocytes

Viscosity of the VP in untreated and latrunculin B-treated unfertilized oocytes was performed as described previously[34-35] with some adaptations. Unfertilized dechorionated oocytes were placed in a gelatin-coated MaTek dish (P50G-0-14-F, MatTek) on an inverted Leica TCS SP5 microscope equipped with a home-made cooling stage (see section 2.7).

Blunt, fire-polished and passivated with heat-inactivated FBS (Sigma-Aldrich) micropipettes with a 20 μm inner diameter were positioned at the VP of unfertilized untreated and treated oocytes. A negative pressure of 150 or 100 Pa (for untreated and treated oocytes respectively) was applied until a constant velocity of the cortex was observed in the pipette (for 6 min approximately) and then the pressure was released immediately. In order to calculate the viscosity, the length of the aspirated cortex was measured over time with a custom-made Fiji macro and plotted over time. The slope of the aspiration curve (L_{asp}) at steady state depends on the viscosity η as follows:

$$L_{asp} = \frac{R_p\,(\Delta P - P_c)}{3\pi\eta}$$

where ΔP is the applied pressure. When the pressure is released and set to zero, the cortex retracts at a rate (L_{ret}):

$$L_{ret} = \frac{R_p\,P_c}{3\pi\eta}$$

Viscosity can be calculated from both aspiration and retraction rates:

$$\eta = \frac{R_p \, \Delta P}{3\pi \left(L_{asp} + L_{ret}\right)}$$

2.8.4 Myoplasm buckling assay

Taking advantage of the micropipette aspiration set up described above (see section 2.8.1), we designed an experiment in order to induce local buckling of the myoplasm upon local ectopic increase of cortical tension.
Blunt, 30° bent angle micropipettes with an inner diameter 20 μm were placed at the lateral side or vegetal poles of myoplasm-labelled (see section 2.5) unfertilized oocytes. A negative pressure below the critical pressure was applied for 4 to 10 min and the deformations of the myoplasm monitored over time.

2.9 UV laser ablation

UV laser ablation of unfertilized oocytes was performed on an Axio Observer Z1 (Zeiss) inverted microscope equipped with a confocal spinning disk unit (Andor Revolution ImagingSystem, Yokogawa CSU-X1), a Q-switched solid-state 355 nm UV-A laser (Powerchip, Teem Photonics) and a C-APOCHROMAT 40x/1.2 W Korr UV-VIS-IR water immersion objective[32, 36] and a home-made cooling stage.

Unfertilized oocytes were either injected with Utrophin-Venus mRNA the previous evening (see section 2.4) or incubated in MitoTracker™ Deep Red FM in order to label their myoplasm (see section 2.5) and oriented with their AP or VP facing the objective, respectively.

The AP actin cortex was cut at the spindle-related actin patch along 3-4 15 μm lines by applying 25 UV pulses at 1kHz. The oocyte was then imaged using a exposure time of 150 ms and 0.2 s frame rate. AP expansion was measured from the maximum recoil of the animal-most cortex of the ablated oocyte. A line was drawn perpendicular to the cut to generate a kymograph (using KymoResliceWide v.0.5 plugin for Fiji *(https://github.com/ekatrukha/KymoResliceWide*) from which the maximum deformation was measured and the animal pole and vegetal pole flow velocities calculated.

The myoplasm was cut at the vegetal-most part of the oocyte along a 10 μm line by applying 25 UV pulses at 1kHz. The oocyte was then imaged using a exposure time of 150 ms and 0.2 s frame rate. A line was drawn perpendicular to the cut to generate a kymograph (using KymoResliceWide v.0.5 plugin for Fiji *(https://github.com/ekatrukha/KymoResliceWide*)).

2.10 Aspect ratio and pole displacement calculations

For calculating the aspect ratio of oocytes/zygotes, 10 brightfield z-slides over the equator of the cell were sum projected and segmented using Ilastik software. The segmented images were stabilized (using StackReg plugin in Fiji) and the center of mass was obtained for each time point. The center of mass oscillated between 1 - 4 pixels (0.33 – 1.2 μm on average) through the time-lapse (within the error margin) so an average was taken. Using a custom-made Fiji plugin, we measured the distance from the center of mass to the animal, vegetal, right and left-most positions over time. The aspect ratio was then calculated as the ratio of the sum of the animal and vegetal distances to the sum of the right and left distances. The animal and vegetal distances were also plotted over time to visualize the individual AP and VP displacements.

2.11 Actin, myosin and myoplasm fluorescent intensity quantifications

For measuring the total fluorescent intensity, the segmented images obtained in section 2.10 were used as ROIs for measuring the total intensity of actin, myosin or myoplasm from whole oocyte sum projections using the Analyze Particles option in Fiji. For measuring the animal and vegetal intensities, only the animal or vegetal half of the oocyte, respectively, was measured. Total fluorescent intensities were batch normalized by modelling the background fluorescence decay as an exponential.

For calculating the cortex to cytoplasmic ratio of actin and myosin fluorescence over time, sum projections of 10 confocal sections (15 μm) over the equator of the cell were segmented using Ilastik software (using the pixel classification method) so that the cortex and cytoplasmic regions were obtained. The segmented images were then used as before to obtain the cortical and cytoplasmic intensities over time.

2.12 Temporal cross-correlation analysis

In order to study whether actin and myosin dynamics were in phase, the normalized actin and myosin total intensities (see section 2.11) were time delay correlated to determine whether there exists a typical time shift between them[37]. Code was generated by Gregory Szep.

2.13 Polar plots and line fluorescent quantification

The images form the segmented actin cortex obtained in section 2.11 were stabilized (using StackReg plugin in Fiji) and processed via a custom-made Python script in order to create the polar plots. The Python code was generated by Matilda Peruzzo.

Using the images from the segmented actin cortex, a line was drawn along one side of the cortex from the AP to the VP. The fluorescent intensity along that line was recorded over 8 time points and plotted as a function of the normalized distance from the AP to the VP.

2.14 Flow velocity analysis

To measure actin and myosin flow velocities in different conditions a 200 x 300 pixel ROI was selected in maximum intensity projections of the whole oocyte centered along the AV axis. This window was used for particle image velocimetry (PIV) analysis using PIVlab[27] and post-processed as in[38] by a custom-made MATLAB script. Flow velocities represented in the kymographs were averaged over 3 consecutive time points. MATLAB code generation and assistance with the analysis was done by Shayan Shamipour.

2.15 Electron Microscopy

Sample preparation and assistance with image acquisition was done by Vanessa Zheden and Daniel Gütl from the Electron Microscopy Facility at IST Austria.

2.15.1 Sample preparation

For high pressure freezing (HPF), unfertilized oocytes were placed in 3 mm diameter aluminum carriers (Wohlwend, Switzerland) with a solution of 5% BSA (Sigma-Aldrich) in ASW and were frozen using a HPM010F (Bal-TEC, Switzerland). Freeze substitution was carried out using an AFS2 (Leica Microsystems, Austria) with an agitation module mounted on (Goldammer et al., 2016; Reipert et al., 2018). Samples were incubated in 0.1% tannic acid in acetone at -90 °C for 24 h, followed by 3 x 10 min washing in acetone at -90 °C. Then samples were placed in 2% osmium tetroxide, 0.1% uranyl acetate in acetone at -90 °C for 4 h, before the temperature was raised at 15 °C/h to -60 °C, then incubated at this temperature for 3 h, followed by a temperature rise of 15 °C/h to -30 °C, then incubated for 3 h at -30 °C. Afterwards the temperature was raised at 15 °C/h to 4 °C, where the samples were incubated for 1 h. Then samples were washed 3 x 10 min in acetone on ice, before infiltration in a graded series of hard DurcupanTM ACM resin in acetone (1:3, 1:1, 3:1). The samples were placed in pure resin overnight at RT and then transferred to BEEM capsules, filled with fresh resin and polymerized for 3 days at 60 °C[39-40].

2.15.2 Transmission Electron Microscopy

Ultrathin sections (70 nm) were cut with a 4 mm Ultra 35° diamond knife (Diatome, Switzerland) using an ultramicrotome (EM UC7, Leica Microsystems, Austria) and mounted on formvar coated copper slot grids. Images were taken with a transmission electron microscope Tecnai 10 operated at 80 kV (FEI/Thermo Fisher Scientific). Images were then processed in Fiji.

2.15.3 Scanning Electron Microscopy

For serial sectioning, the blocks were trimmed with an Ultratrim diamond knife (Diatome, Switzerland) to a rectangle and a depth of 100 mm using an ultramicrotome (EM UC7, Leica Microsystems, Austria). Prior to sectioning, a carbon-coated Kapton tape (RMC Boeckeler, USA) was plasma treated using an ELMO glow discharge cleaning system (Agar Scientific, UK), equipped with a homemade reel-to-reel motorized winder, for increasing the hydrophilicity of the tape. Serial sections of 70 nm thickness were cut with a 4 mm Ultra 35° diamond knife (Diatome, Switzerland) and picked up with the plasma-treated tape using an automated tape-collecting ultramicrotome (ATUMtome, RMC Boeckeler, USA). After collecting the sections on the tape, the tape was mounted on 4 inch silicon wafers (University Wafer, USA) with conductive double sided adhesive carbon tape (Science Services, Germany). Then the wafers were coated with a 5 nm carbon layer to ensure conductivity (EM ACE600, Leica Microsystems, Austria). Sections were imaged by a scanning electron microscope (FE-SEM Merlin compact VP, Carl Zeiss, Germany) equipped with the Atlas 5 Array Tomography software (Carl Zeiss, Germany). The high-resolution serial images were taken with 5 nm pixel resolution, at 5kV using a backscattered electron detector. The serial images were then concatenated, aligned and segmented using TrackEM (NIH). Segmented images were imported into Imaris software for visualization.

2.16 Myoplasm Length and Buckling analysis

Single confocal central sections of actin and myoplasm-labelled oocytes were binarized and the signal was fitted to an ellipse. Then a second fit of the surface modes was performed on the fitted ellipse with gaussian basis functions using linear regression. Details of implementation can be found in appendix A.
Code generation and assistance with the analysis was done by Gregory Szep.

2.17 Centrifugation of unfertilized oocytes

In order to either displace the myoplasm from unfertilized oocytes, we designed a centrifugation experiment based on previous publications[41-43] with some modifications.
Utrophin-Venus expressing unfertilized oocytes were placed on a 5-30% Ficoll® PM400 in ASW continuous gradient (Gradient Station, Biocomp) and centrifuged for 1 h at 1500 g at 16 °C in an Beckman Optima XPN-100 Ultracentrifuge (Beckman Coulter, Inc.) using a swinging-bucket rotor (SW 41 Ti, Beckman Coulter, Inc.). Immediately after centrifugation, centrifuged oocytes were collected and washed at least 5 times in ASW to remove any residual Ficoll® PM400. Oocytes with the myoplasm displaced from the vegetal-most cortex were then incubated in MitoTracker™ Deep Red FM and fertilized under the microscope.

2.18 Whole mount immunofluorescence

Oocytes were stained following previously published methods[44] with minor modifications.

Oocytes were fixed in 4% formaldehyde (Sigma-Aldrich) in ASW at 16 °C for 2 h under gentle stirring. After fixation they were washed 3 times in PBS and permeabilized for 30 min in PBS-Tr (0.1% Triton 100-X in PBS). Then oocytes were incubated in blocking solution (0.1% Tween20, 0.5% goat serum in PBS) for 30 min. Oocytes were incubated in the primary antibody (1/400 dilution in blocking solution, see key resource table) overnight at 4 °C and washed 5 times in PBS-Tw (0.1% Tween20 in PBS). Incubation of the secondary antibody (1/100 dilution in blocking solution, see key resource table) was carried out for 4 h at RT. To label the maternal and paternal DNA, Hoescht (5 ug/ml) was added for the final 10 min of incubation. Oocytes were washed 5 times in PBS and mounted for imaging as in section 2.7.

2.19 Data analysis and statistics

Statistical analysis was performed using Prism 8 (GraphPad software). The statistical test used in each case and the resulting p-values are indicated in each figure. N were considered as independent experiments and n specify the number of oocytes and are indicated in each figure. No statistical method was used to predetermine sample size. The experiments were not randomized.

3. Results

The data presented here is the result of a collaborative work. The specific contribution of each collaborator is highlighted in the corresponding figure legend.

3.1 Changes in cell shape upon ascidian oocyte fertilization

In the ascidian *Phallusia mammillata* remarkable changes in cell shape can be observed upon fertilization and during the first minutes of development (Fig. 3.1.A). These cellular deformations involve successive oscillations along the AV axis. We therefore classified them according to the time scales of these oscillations (Fig. 3.1.A): a *fast AV oscillation* during the first 3 minutes post fertilization followed by a *slow AV oscillation* for the next 4 minutes.

The unfertilized oocyte is almost a perfect sphere (Fig. 3.1.A, Unfertilized). Fertilization triggers a fast cycle of lengthening and shortening of the AV axis here termed as *fast AV oscillation*. It takes place within the first 3 minutes of development (Fig. 3.1.A, 1 mpf – 3 mpf, white arrow head). This is followed by a *slow expansion of the AV axis* during the next 3-4 minutes that culminates with the formation of the CP (Fig. 3.1.A, 6 mpf, black arrow head) and the extrusion of the first PB at 7.5 mpf (Fig. 3.1.A, 6 mpf, asterisk). The zygote eventually recovers its original circular shape at 13 mpf (Fig. 3.1.A, 13 mpf). After the first PB is extruded, a series of fast contractions are visible in the cell which are associated with fast calcium oscillations in the newly fertilized oocyte[45]. From now on, we focused our analysis only on the changes in cell shape that take place before the first PB extrusion: the *fast AV oscillation* upon fertilization and the ensuing *slow AV expansion*.

In order to deepen our understanding of the nature of the two phases, we sought to describe the cellular deformations as changes in the 2-dimensional (2D) aspect ratio of the newly fertilized oocyte (Fig. 3.1.B-B'). Aspect ratio analysis - calculated as the ratio between the lengths of the AV axis and the left-right (LR) axis (Fig. 3.1.B) over time - confirms the periodic oscillations along the AV axis identified in the brightfield images: the initial *fast AV oscillation* corresponds to a rapid elongation of the AV axis immediately after fertilization (Fig. 3.1.B', first dotted line) followed by a quick recovery of almost the original circular shape at 3 mpf (Fig. 3.1.B', orange area). Next a second *slower expansion of the AV axis* takes place and lasts until 7.5 mpf when the first polar body is finally extruded (Fig. 3.1.A, asterisk; Fig. 3.1.B', second dotted line, grey area). This second AV axis expansion is concomitant with the formation of the CP (Fig. 3.1.A, black arrow head; Fig. 3.1.B', grey area – in all figures, black arrow head) that is fully expanded at 7.5 mpf.

To perform a more detailed analysis of these deformations, we measured the distance of both the animal and vegetal poles from the center of mass (CM) over time (Fig. 3.1.C-C"). Interestingly, both ends of the AV axis deformed differently. Whereas the initial AV elongation corresponds with an expansion of both the animal and vegetal poles - albeit, more pronounced at the AP (Fig. 3.1.C", pink, orange area) - the recovery of the original value of the aspect ratio at 3mpf is due to the flattening of the VP (Fig. 3.1.C'-C", orange line, white arrow head). This difference between poles is more pronounced during CP formation which

corresponds with an expansion of the VP alone (Fig. 3.1.C', orange line, grey area, black arrow head).

These results indicate that the initial AV axis elongation upon fertilization corresponds to a fast expansion of both animal and vegetal poles but the recovery of the circular shape and CP formation correspond to only deformations on the VP of the newly fertilized oocyte.

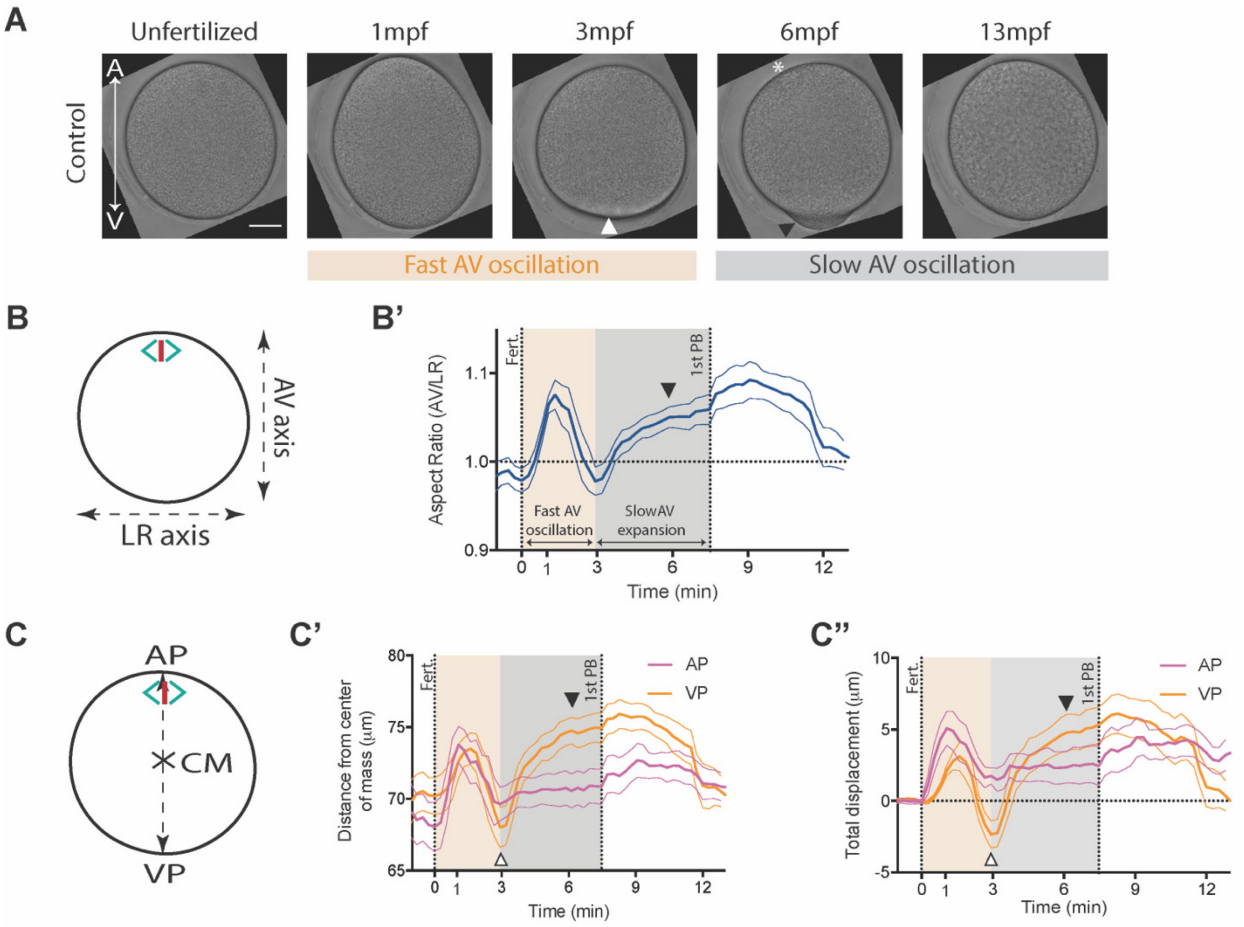

Fig. 3.1 – Changes in cell shape upon ascidian oocyte fertilization. (**A**) Brightfield confocal cross-sections of an ascidian oocyte/zygote from unfertilized to 13 mpf. A is animal, V is vegetal. White arrow head shows flattening at the VP, black arrow head shows the CP and the white asterisk shows the position of PB extrusion. Scale bar, 30 µm. (**B**) Schematic illustration of the aspect ratio analysis. AV axis is the distance from the animal to the vegetal pole. LR axis is the distance from the left to the right edges of the cell along the center of the cell. (**B'**) Quantification of the aspect ratio from the unfertilized oocyte to 13 mpf. The dotted line at 0 min indicates the fertilization timepoint. The dotted line at 7.5 min indicates the time where the first PB has formed. The orange-shaded area corresponds with the time of the fast oscillation of the AV axis. The grey area demarcates the timepoints of CP formation. Black arrow head shows the CP. (**C**) Schematic illustration of the poles displacement analysis. AP is the animal pole, VP is the vegetal pole and CM is the center of mass. (**C'**) Quantification of the distance from the animal and vegetal poles to the center of mass from the unfertilized oocyte to 13 mpf. White arrow head shows flattening at the VP, black arrow head shows the CP. (**C"**) Quantification of the total displacement for animal and vegetal poles in C'. White arrow head shows flattening at the VP, black arrow head shows the CP.
N = 8 animals, n = 10 oocytes. Error bars, SEM.

3.2 The role of the cytoskeleton in driving the changes in cell shape

The deformations described here are the result of what traditionally has been referred to as a cortical contraction triggered by fertilization[16]. It has been previously shown that the cortical contraction in ascidian oocytes is dependent on the activity of actin and myosin but not on the activity of microtubules[13]. Therefore, we examined the contributions of different cytoskeletal elements to the shape oscillations (Fig. 3.2.A). Consistent with previous observations, treating the oocyte with the actin polymerization inhibitor Latrunculin B severely undermined both expansions along the AV axis. The fast expansion-shortening following fertilization was severely diminished and no flattening at the VP was observed. In addition the slow VP expansion was also affected (Fig. 3.2.B). As a consequence, CP formation was not observed in these oocytes. Similarly, when myosin contractility was lowered by overexpression of a constitutively active version of myosin phosphatase (CaMypt)[24], all deformations were absent and the aspect ratio did not oscillate during the first minutes of development (Fig. 3.2.B). Interestingly, small short-lived protrusions were observed at the VP coinciding in time with the flattening at the VP in the control embryos (Fig. 3.2.A, 3 mpf, white arrow head). Finally, by depolymerizing microtubules using nocodazole, we observed that the range of the AV deformations was affected but not the nature of such deformations since we could still observe both the initial AV expansion and the VP elongation during CP formation (Fig. 3.2.B).

Altogether, this indicates that the deformations observed upon ascidian oocyte fertilization are the result of the activity of actin and myosin and that microtubules are not directly involved in the so-called cortical contraction upon fertilization.

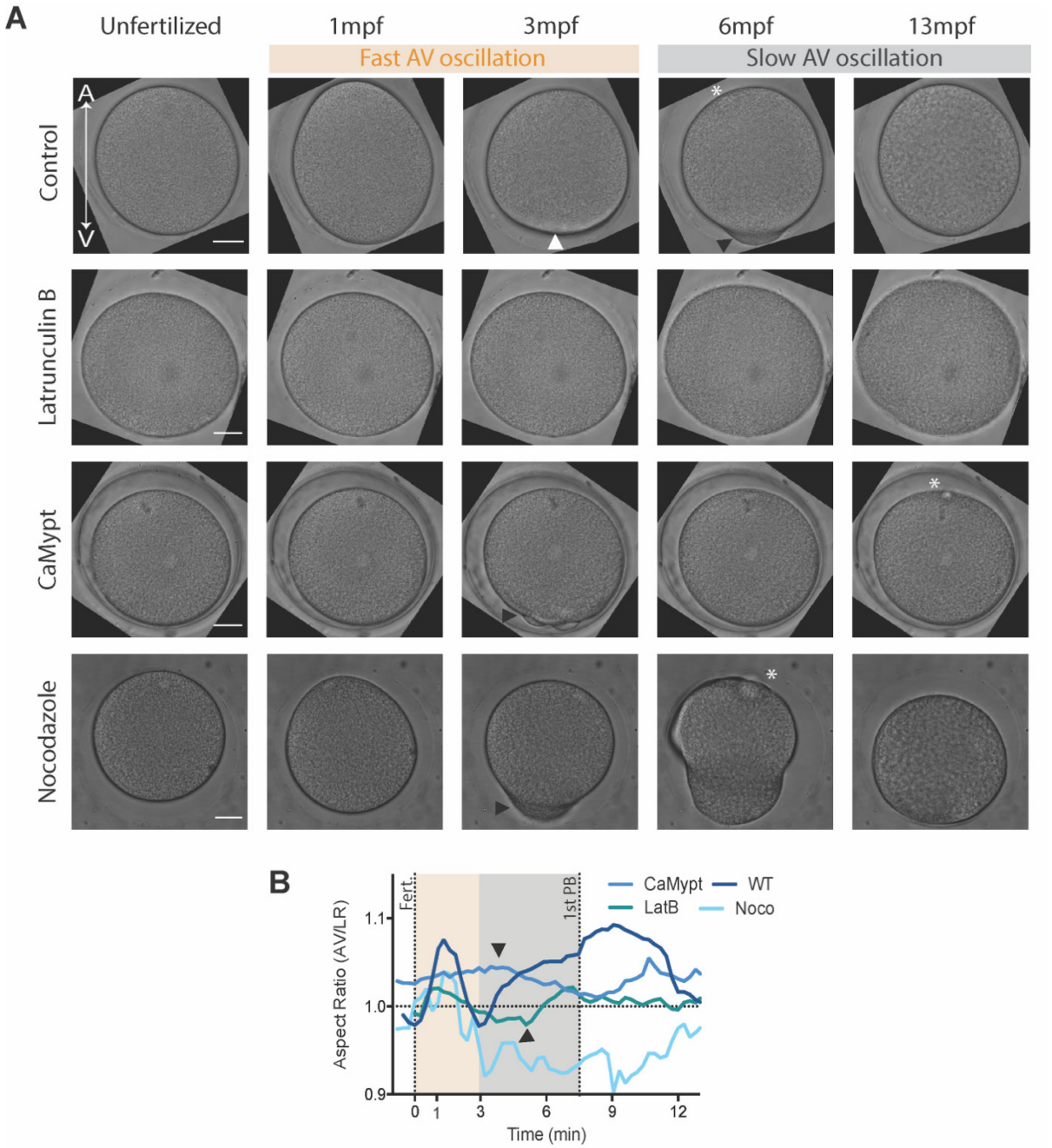

Fig. 3.2 – Changes in cell shape upon fertilization in oocytes treated with cytoskeletal inhibitors. (**A**) Brightfield confocal cross-sections of ascidian oocytes/zygotes from unfertilized to 13 mpf treated with Latrunculin B (1 μg/ml, 10 min incubation before fertilization), CaMypt (mRNA injection 3 h before fertilization) and Nocodazole (0.6 μM, 10 min before fertilization). White arrow head shows flattening at the VP, black arrow head shows the CP and the white asterisk shows the position of PB extrusion. Scale bar, 30 μm. A is animal, V is vegetal. (**B**) Quantification of the average aspect ratio from unfertilized oocyte to 13 mpf for the conditions in A. Control (taken from Fig. 3.1.B'), Latrunculin B (N = 2 animals, n = 4 oocytes), Nocodazole (N = 2 animals, n = 2 oocytes), CaMypt (N = 2 animals, n = 3 oocytes). Black arrow head shows the CP, asterisk shows the first PB. Error bars omitted for clarity.

3.3 Actomyosin reorganization upon fertilization

The previous analysis confirmed that the cell shape changes triggered by fertilization in the ascidian oocyte are dependent on actin and myosin activity. Additionally, the observed flattening at the VP is a further indication of a contractile event, in agreement with published reports of a cortical contraction travelling along the cortex in the animal-vegetal direction inducing CP formation[16, 46]. We therefore analyzed the localization and the dynamic distribution of actin and myosin during the fertilization-induced cortical contraction and CP formation.

In order to visualize actin and myosin, we injected the following mRNAs into mature unfertilized oocytes: Utrophin-Venus and Utrophin-mCherry for actin labelling and iMyo-YFP and iMyo-mKO for myosin[47]. Injected oocytes were fertilized under the microscope (Fig. 3.3.A). We then quantified the total amount of actin and myosin before and after fertilization (Fig. 3.3.B-C) as well as their dynamic redistribution over time (Fig. 3.3.E-E'').

In the mature unfertilized oocyte, actin was preferentially localized to the cortex (Fig. 3.3.A, Unfertilized; Fig. 3.3.C, green, left axis). Upon fertilization there was a slight cortical enrichment (Fig. 3.3.C, orange area) that eventually decayed during the last steps of CP expansion (Fig. 3.3.C, grey area). Interestingly, although the cortical enrichment of actin remained relatively constant during the fast and slow oscillations, the total amount of actin experienced a 2-fold increase following fertilization (Fig. 3.3.B, green, left axis, orange area), an indication of actin polymerization upon fertilization most of which was recruited to the cortex. Myosin localization in the unfertilized oocyte, on the other hand, was mostly cytosolic (Fig. 3.3.A, Unfertilized; Fig. 3.3.C, magenta, right axis) but accumulated at the cortex progressively upon fertilization until the CP was fully expanded (Fig. 3.3.C, orange and grey areas). This observation together with the fact that the total amount of myosin also increased 1-fold at fertilization (Fig. 3.3.B, magenta, right axis) indicated that myosin remained mostly cortical during the first minutes of development.

Given that the initial localization of actin and myosin was not the same before fertilization, we performed a temporal cross-correlation analysis in order to elucidate if their dynamics were correlated in time (Fig. 3.3.D). We found that normalized total actin and myosin intensities were closely correlated as their cross-correlation peaked at zero time lag (Fig. 3.3.D).

Time-lapse images of actin and myosin during the cortical contraction showed a polarized redistribution of cortical actomyosin in the AV direction with progressive accumulation of actomyosin at the VP (Fig. 3.3.A). Therefore, we analyzed the dynamic distribution of actomyosin upon fertilization in the animal and vegetal halves of the zygote (Fig. 3.3.E). We found that actin and myosin were preferentially accumulated at the vegetal half of the unfertilized oocyte (Fig. 3.3.E'-E'', 0 min) indicating an already polarized actomyosin distribution along the AV axis before fertilization. This polarization was reinforced during the fast AV oscillation (Fig. 3.3.E'-E", orange area) reaching the maximum difference between animal and vegetal halves at a time that coincides with the flatting of the VP (Fig. 3.3.E'-E'', 3 min; Fig. 3.3.F, 3 min). Interestingly, both actin and myosin accumulation at the vegetal half decreased during the slow AV elongation that leads to CP formation (Fig. 3.3.E'-E'', grey area;

Fig. 3.3.F) suggesting that a cortical relaxation and not a contraction, as it was previously reported[13], takes place during CP formation.

Altogether these results indicate that cortical actomyosin dynamically reorganizes upon fertilization. First, actomyosin is rapidly depleted from the AP and progressively accumulates at the VP cortex during the first expansion of the AV axis (Fig. 3.3.E). This suggests actomyosin accumulation at the VP is responsible for its flattening. Surprisingly, this accumulation precedes CP formation, in disagreement with previous reports that causally relate the cortical contraction with CP formation[16]. Instead, we observe a relaxation of the cortex at the vegetal pole that would allow the CP to expand and finally form.

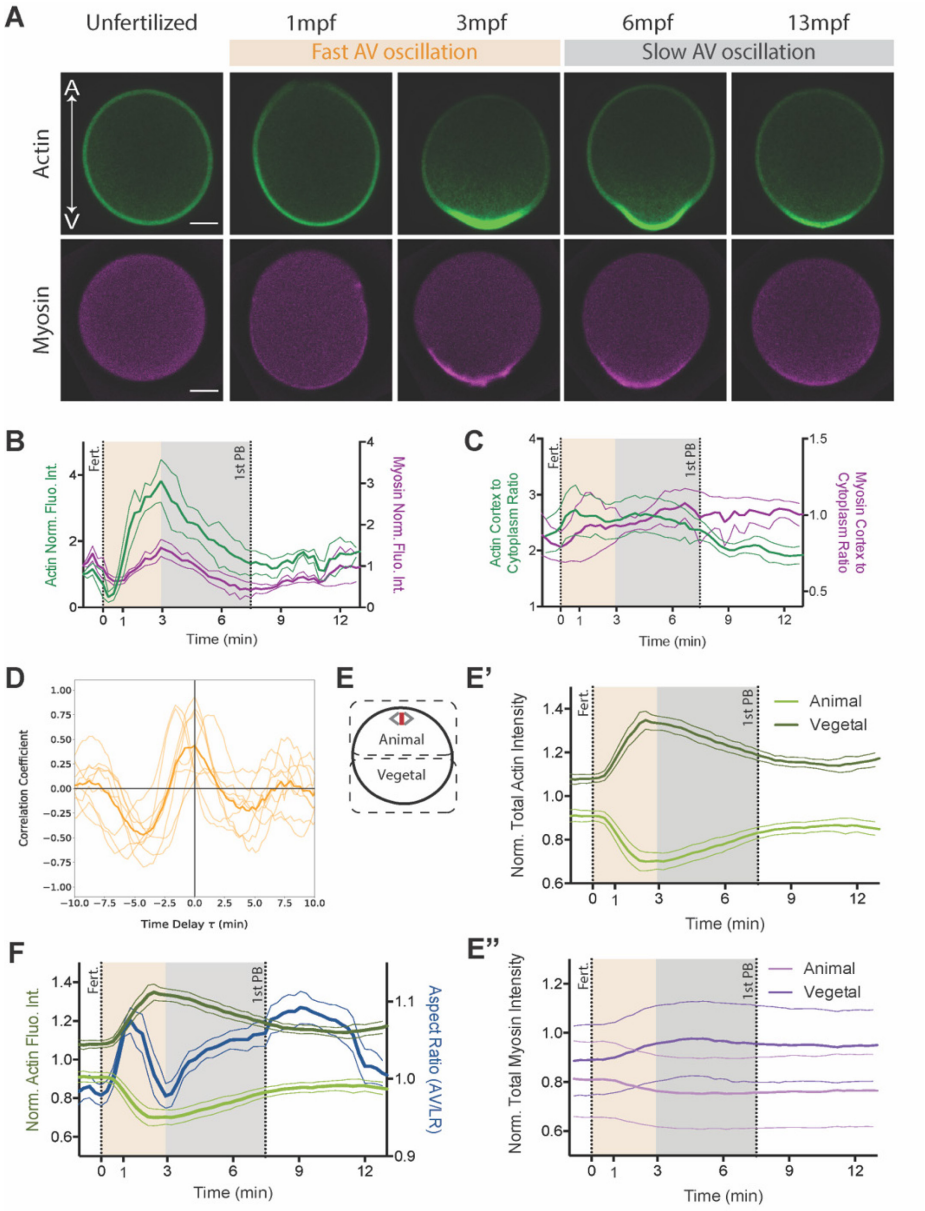

Fig. 3.3 – Actomyosin reorganization upon fertilization. (**A**) Sum intensity projections over 10 central z-slides (15 μm) of ascidian oocytes/zygotes from unfertilized to 13 mpf expressing Utrophin-Venus to mark F-actin (top row) and iMyo-YFP to mark myosin (bottom row). A is animal, V is vegetal. Scale bar, 30 μm (**B**) Quantification of total actin (green line, left Y axis) and myosin (magenta line, right Y axis) intensities over time in oocytes co-expressing Utrophin-Venus to mark F-actin and iMyo-mScarlet to mark myosin. N = 2 animals, n = 3 oocytes. Error bars, SEM. (**C**) Quantification of the ratio of cortical to cytoplasmic intensities for actin (green line, left Y axis, N = 3 animals, n = 3 oocytes) and myosin (magenta line, right Y axis, N = 2 animals, n = 3 oocytes) over time in Sum projections over 10 central z-slides (15 μm). Error bars, SEM. (**D**) Temporal cross-correlation analysis between actin (N = 3 animals, n = 3 oocytes) and myosin (N = 3 animals, n = 3 oocytes) total intensities showing peaks at time lag zero. Plot shows individual actin-myosin cross-correlation (semitransparent orange lines) and the average (thick orange line). Code generated by Gregory Szep. (**E**) Schematic representation for the animal-vegetal intensity analysis in E' and E''. (**E'**) Quantification of the total actin intensity in the animal and vegetal halves of ascidian oocytes/zygotes from unfertilized to 13 mpf (N = 3 animals, n = 4 oocytes). Error bars, SEM. (**E''**) Quantification of the total myosin intensity in the animal and vegetal halves of ascidian oocytes/zygotes from unfertilized to 13 mpf (N = 3 animals, n = 5 oocytes). Error bars, SEM. (**F**) Overlay of actin intensity redistribution, taken from E', and changes aspect ratio, taken from Fig. 3.1.B', over time.

3.4 An increase in cortical contractility upon fertilization drives the fast AV expansion and shortening

To understand how actomyosin polarization towards the VP might direct the cellular deformations observed during the fast AV oscillation, we first examined the organization of cortical actin in unfertilized oocytes (Fig. 3.4.A-A'). We found that actin is homogenously distributed along the cortex of the oocyte. An AP view, however, shows a bright patch of actin associated to the spindle[14] (Fig. 3.4.A-A', arrow head) at the center of an area depleted of actin (Fig. 3.4.A'). This local depletion of actin surrounding the meiotic spindle could render the cortex at the AP-most part of the oocyte weaker than at the rest of the oocyte surface and therefore more susceptible to contractility-induced cortical instabilities[48-50].

Next, we analyzed the dynamic reorganization of cortical actin during the fast AV oscillation. We found that prior to any observable deformations of the newly fertilized oocyte, a small zone of local actin depolymerization became visible (Fig. 3.4.B. 48s, white arrow head). Given that this small area was observed at any position around the oocyte surface and that it preceded any obvious cellular deformations, we postulate it corresponds to the sperm entry point at fertilization[18, 51]. This is in agreement with studies in *C. elegans* where the sperm centrosome has been shown to locally downregulate actomyosin contractility and induce polarizing cortical flows[52-53]. In addition, a hallmark of animal fertilization is the establishment of an sperm-triggered calcium wave that raises the cytoplasmic levels of calcium[17, 54] and activates myosin II contractility[55]. We thus speculate that the observed AV actomyosin polarization is the result of cortical actomyosin flows caused by a newly established gradient of contractility along the AV axis. To test this hypothesis, we examined and quantified cortical actin dynamics at a high temporal resolution (Fig. 3.4.B-C-D) during the fast AV oscillation. Surprisingly, we found that upon fertilization, the actin cortex ruptured, beginning at the actin-depleted region of the AP (Fig. 3.4.B, 48 s – 1 min 4 s; Fig. 3.4.C, 48 s – 1 min 4 s; Fig. 3.4.D, 48 s – 1 min 4 s). The rupture then propagated towards the VP (Fig. 3.4.C, 48 s – 1 min 20 s; Fig. 3.4.D, 48 s – 1 min 20 s, white arrow) consistent with the AP expansion we described previously (Fig. 3.1.C', pink line, orange area). Therefore, this rupture likely triggers the loss of actin at the animal half upon fertilization that we observed previously (Fig. 3.3.E').

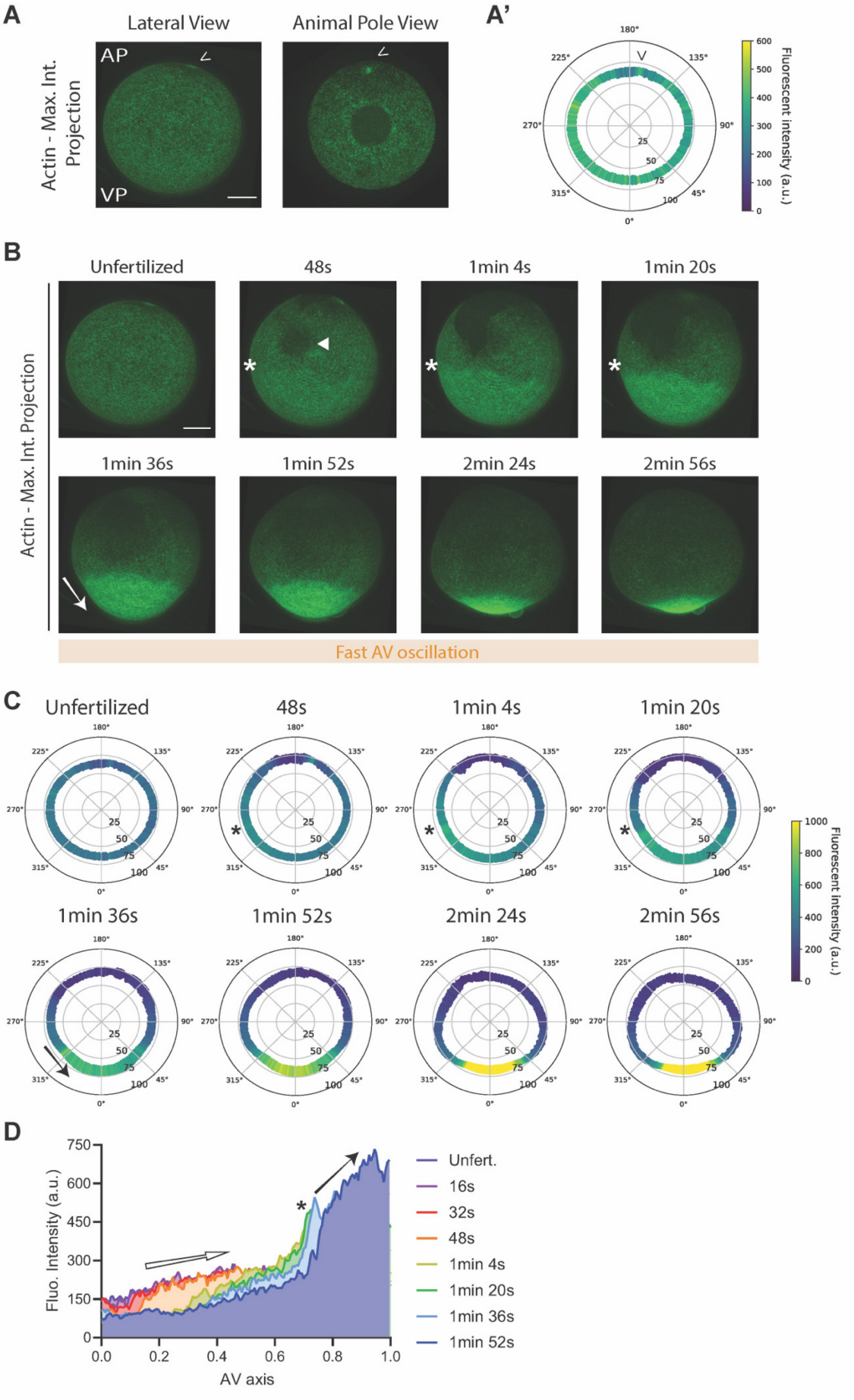
A
Lateral View
Animal Pole View
Actin - Max. Int. Projection
AP
VP
A'
V
Fluorescent Intensity (a.u.)
B
Unfertilized
48s
1min 4s
1min 20s
1min 36s
1min 52s
2min 24s
2min 56s
Actin - Max. Int. Projection
Fast AV oscillation
C
Unfertilized
48s
1min 4s
1min 20s
1min 36s
1min 52s
2min 24s
2min 56s
Fluorescent Intensity (a.u.)
D
Fluo. Intensity (a.u.)
AV axis
Unfert.
16s
32s
48s
1min 4s
1min 20s
1min 36s
1min 52s

Fig. 3.4 – Dynamic redistribution of cortical actin during the fast AV oscillation. (**A**) Maximum intensity projections of actin in unfertilized oocytes. AP is animal pole, VP is vegetal pole. Arrow head indicates the patch of actin accumulation at the spindle. Scale bar, 30 μm. (**A'**) Polar plot of segmented cortical actin intensity of sum intensity projections over 10 central z-slides (15 μm) an unfertilized oocyte (taken from Fig. 3.3.A, Unfertilized). Arrow head indicates the position of the bright actin patch. Angles represent the position around the oocyte (VP is at 0°, AP is at 180°). The radius of the oocyte (in μm) is indicated in the concentric circles. Color bar indicates fluorescent intensity in arbitrary units. Code generated by Matilda Peruzzo. (**B**) Maximum intensity projections of confocal images of cortical actin intensity during the fast AV oscillation. Arrow head indicates the point of sperm entry, asterisk indicates the position of the actin transition zone (see section 3.6) and the arrow indicates the time where flows the transition zone are first detected (see section 3.6). Scale bar, 30 μm. (**C**) Polar plots as in A' for the timepoints shown in B. Asterisk indicates the position of the actin transition zone (see section 3.6) and the arrow indicates the time where flows are first detected (see section 3.6). Code generated by Matilda Peruzzo. (**D**) Line quantification of actin intensity along the cortex during consecutive timepoints upon fertilization for one oocyte. White arrow indicates the vegetal-ward increase in intensity at the animal half during the first time points. Asterisk corresponds to the position of the actin transition zone in B and C. Black arrow indicates the vegetal flow of the transition zone also shown in B and C (see section 3.6).

Due to the short time scales at which the AP expands (Fig. 3.1.C', pink line, orange area) and the fact that the rupture of the cortex increases in size (Fig. 3.4.B-C, 48 s - 1 min 20 s), we suggest that an elastic peeling of the cortex at the AP would induce a release of tension along the AV axis similar to what has been observed *in vitro* using reconstituted actin cortices anchored to liposome membranes[50, 56] or during bleb formation[57]. In order to test this hypothesis, we performed UV laser ablations at the actin-depleted area of the AP cortex of unfertilized oocytes with the aim of mimicking the tear of the cortex that occurs upon fertilization and in a calcium-independent manner (Fig. 3.5.A). We found that the AP expands upon UV laser ablation in unfertilized oocytes (Fig. 3.5.A') suggesting that the rupture of the cortex and the release of tension along the AV axis are sufficient to induce the fast expansion of the AP upon fertilization.

We also observed that cortical actin flows of an average speed of 1.7 μm/min towards the VP were established upon UV laser ablation (Fig. 3.5.A"). We thus asked whether such flows are also present in the cortex of fertilized oocytes and if they are responsible for the vegetal actomyosin accumulation. Particle image velocimetry (PIV) and kymograph analysis of high temporal resolution movies of the actin cortex confirmed our hypothesis. Fig. 3.5.B shows an exemplary kymograph of the 2D actin flow profile in a central area of the zygote. It reveals that cortical actin flows towards the vegetal pole of an average velocity of 9 μm/min (Fig. 3.5.B, 48 s – 3 min, black arrow; Fig. 3.5.B', red, right axis) were established upon fertilization. These flows followed the rupture of the cortex at the AP (Fig. 3.5.B, 0 s – 48 s) and would explain the accumulation of actin at the VP that precedes the flattening at the vegetal cortex (Fig. 3.4.C, 1 min 36 s – 2 min 56 s, black arrow; Fig. 3.4.D, 1 min 36 s – 2 min 56 s, black arrow).

The expansion of the AP in laser-ablated unfertilized oocytes is an indication that the unfertilized oocyte displays tension along the AV axis that is released with the rupture of the cortex upon fertilization[50]. Considering the importance of cortical tension anisotropy for the establishment and maintenance of cortical actomyosin flows[38, 53, 58-59] and our observation that the velocity of both the rupture of the cortex at the AP and of the vegetally-directed flows were faster in fertilized oocytes than in the laser-ablated oocytes (Fig. 3.5.C), we asked whether cortical tension increases in ascidian oocytes upon fertilization. Using micropipette aspiration we found that cortical tension is not equal at the animal and vegetal poles of unfertilized oocytes (Fig. 3.5.D), and is significantly higher at the VP. Upon fertilization, the intracellular calcium concentration raises rapidly (Fig. 3.5.E-E', magenta, right axis) inducing an increase of cortical tension along the AV axis that reaches the maximum at 1 mpf when the cortex tears at the AP (Fig. 3.5.E'). This agrees with previous observations that an increase in contractility leads to cortical instabilities that eventually cause rupture of the cortex at its weakest point[48, 60] and its accumulation at the opposite site[50]. Interestingly, during the second slow AV expansion, cortical tension decreases at both animal and vegetal poles, consistent with our previous observation that actomyosin intensity decreases during CP formation at the VP (Fig. 3.5.E', grey area; Fig. 3.3.E'). This further supports our idea that a cortical relaxation, and not contraction as was previously proposed[16], leads to CP formation.

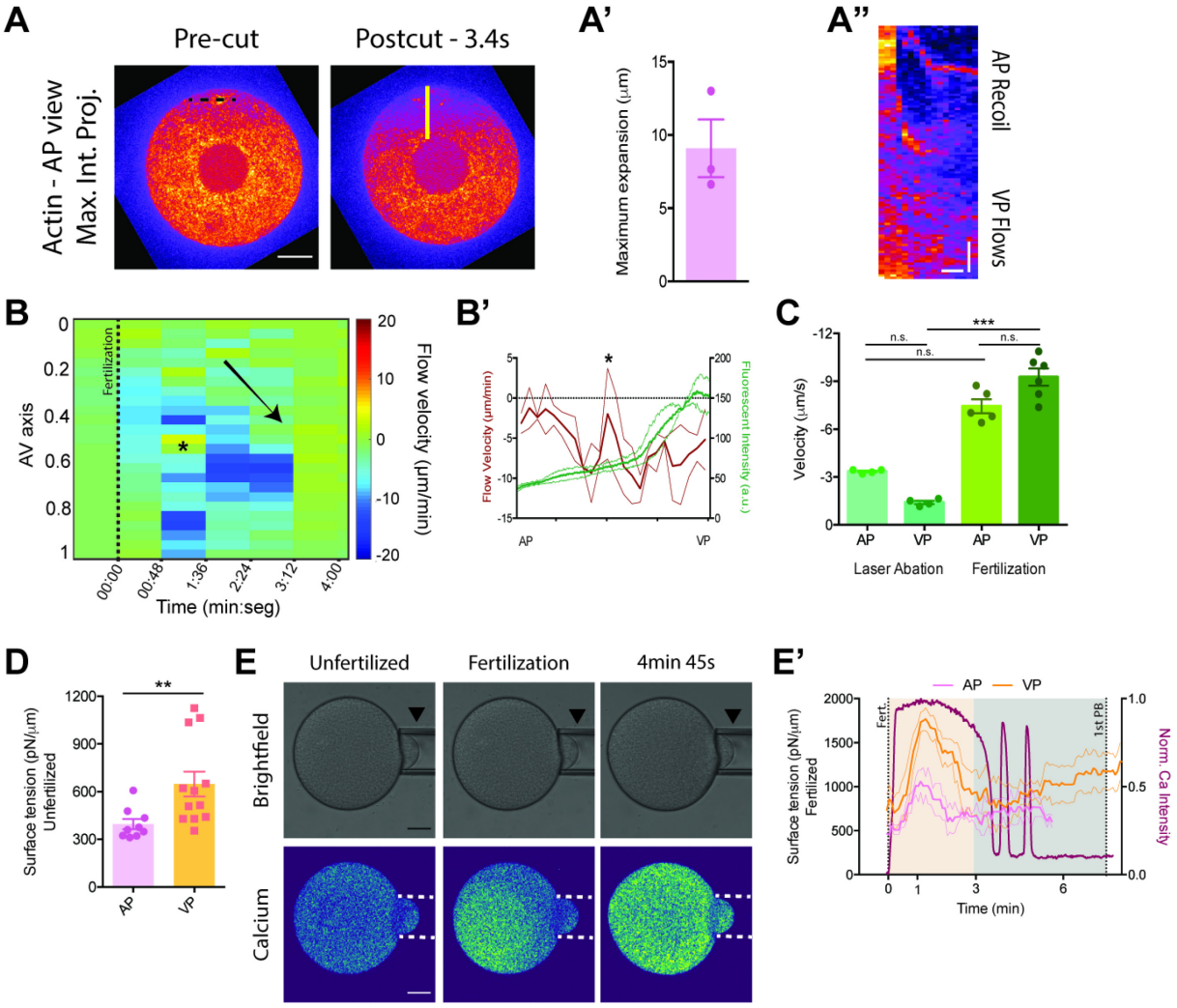

Fig. 3.5 – Contractility-driven cortical actin flows upon fertilization. (**A**) Maximum intensity projection of actin intensity at the AP in unfertilized oocytes before and after UV laser ablation. Black dotted line indicates the ablation site. Scale bar, 30 μm. (**A'**) Quantification of expansion of the AP upon ablation. N = 2 animals, n = 3 oocytes. Error bars, SEM. (**A"**) Kymograph along the solid yellow line in A showing AP recoil/expansion on the top and vegetal-ward flows at the bottom. Vertical scale bar, 10 μm. Horizontal scale bar, 3 s. (**B**) Kymograph of actin flow velocity along the AV axis during the fast AV oscillation. Color bar indicates velocity in μm/min (positive velocities towards the AP, negative velocities towards the VP. Arrow indicates the direction of the flow, asterisk indicates the actin transition zone identified in Fig. 3.3.B (see also section 3.6). Code generated by Shayan Shamipour who also helped with the analysis. (**B'**) Average actin flow velocity (red line, left axis) along the AV axis during the first timepoint that vegetal flows are visible. Actin intensity profile at the time of the flows is shown in green (right axis). Asterisk indicates the actin transition zone identified in Fig. 3.3.B (see also section 3.6). N = 2 animals, n = 2 oocytes. Error bars, SEM. (**C**) Bar chart of actin flow velocity at AP and VP poles in laser-ablated oocytes and during fertilization. N = 2 animals, n = 4 oocytes for laser ablation experiments; N = 3 animals, n = 5 oocytes for animal flows and n =. 5 for vegetal flows for fertilized oocytes. Kruskal-Wallis test and Dunn's multiple comparisons test, n.s., not significant, ***p = 0.0014. Error bars, SEM. (**D**) Surface tension at AP (N = 6 animals, n = 9 oocytes) and VP (N = 5 animals, n = 12 oocytes) of unfertilized oocytes. Mann-Whitney test, **p = 0.0056. Error bars, SEM. (**E**) Confocal cross-sections of brightfield and calcium during a micropipette aspiration experiment in fertilized oocytes. The black arrow head indicates the constant length of the aspirated oocyte in the pipette. Scale bar, 30 μm. (**E'**) Quantification of changes in cortical tension over

time at the AP (pink line, left axis. N = 2 animals, n = 3 oocytes) and VP (orange line, left axis. N = 2 animals, n = 5 oocytes) as a function of normalized calcium intensity (magenta line, right axis). Error bars, SEM.

To further address the possibility that the cortical actin polarization controlling the vegetal flattening is triggered by contractility-driven flows, we performed similar PIV analysis of oocytes expressing the myosin marker iMyo-YFP (Fig. 3.6.A) and in oocytes overexpressing CaMypt (Fig. 3.6.C) in order to downregulate actomyosin contractility. We found that myosin flows were of the same velocity as actin (Fig. 3.6.B-B') further supporting the idea that contractility-driven flows modulate the vegetal accumulation of actin and myosin, eventually leading to the flattening of the VP during the fast AV oscillation. In CaMypt overexpressing oocytes actin flows were severely diminished and no rupture of the cortex was observed (Fig. 3.6.D-D'), consistent with the notion that a fast increase in contractility at fertilization causes the cortex to rupture at the AP leading to the initial fast elongation of the AV axis, the establishment of vegetally-directed cortical flows and the ensuing vegetal flattening.

All together these results support the idea that at the early stages (i.e., at short time scales) the increase of cortical tension - caused by the fertilization calcium wave - triggers an isotropic elastic cortical contraction that causes the actin cortex to break at the AP where it is weaker. At later stages (i.e., at long time scales), the viscous behavior of the actomyosin cortex[61] and vegetally-directed cortical flows modulate the further vegetal polarization of the actomyosin cortex and the flattening of the VP cortex but do not direct CP formation.

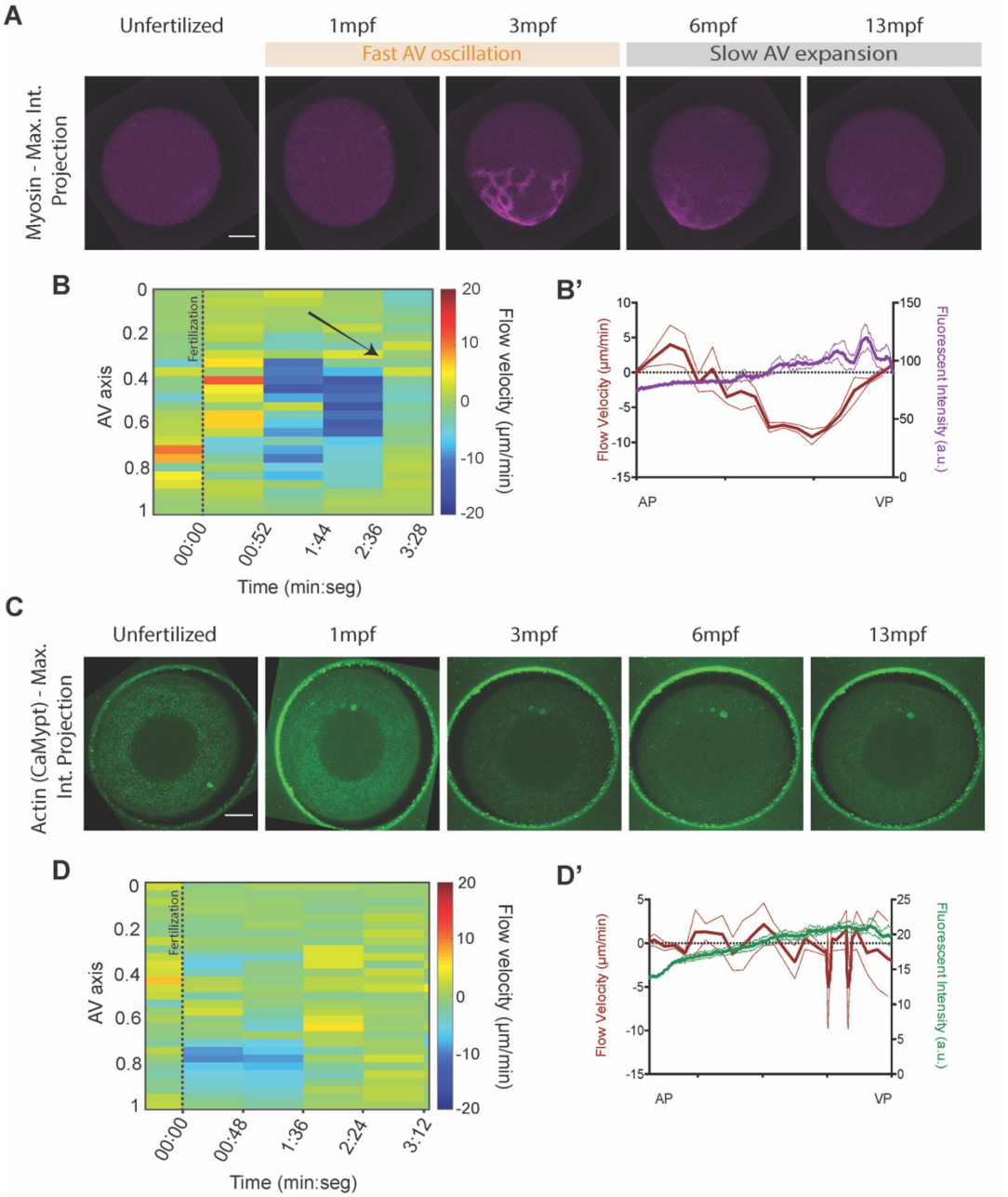

Fig. 3.6 – Cortical myosin flows and defective cortical actin flows in the absence of myosin contractility. (**A**) Maximum intensity projections of confocal images of cortical myosin intensity during the fast AV oscillation and the slow AV expansion. Scale bar, 30 µm. (**B**) Kymograph of myosin flow velocity along the AV axis during the fast AV oscillation. Color bar indicates velocity in µm/min (positive velocities towards the AP, negative velocities towards the VP). Arrow indicates the direction of the flows. Code generated by Shayan Shamipour that also helped with the analysis. (**B'**) Average myosin flow velocity along the AV axis (red line, left axis) during the first timepoint that vegetal flows are visible. Myosin intensity profile at the time of the flows is shown in magenta (right axis). N = 2 animals, n = 2 oocytes. Error bars, SEM. (**C**) Maximum intensity projections of confocal images of cortical actin intensity in CaMypt overexpression oocytes during the first 13 minutes of development. Scale bar, 30 µm. (**D**) Kymograph of actin velocity along the AV axis during the first 3 minutes post fertilization. Color bar indicates velocity in µm/min (positive velocities towards the AP, negative velocities towards the VP). Code generated by Shayan Shamipour who also helped with the analysis. (**D'**) Average actin flow velocity along the AV axis during the first timepoint upon fertilization. actin intensity profile at the time of the flows is shown in green (right axis). N = 2 animals, n = 3 oocytes. Error bars, SEM.

3.5 A mitochondria-rich subcortical layer resists the deformations and flows during the initial fast AV elongation

Actin maximum intensity projections and the polar analysis of actin reorganization along the cortex (Fig 3.4.B-D) revealed a surprising observation: upon rupture of the actin cortex at the AP, actin accumulated at a point in the central-to-vegetal portion of the cortex (Fig. 3.4.B, 48 s – 1 min 20 s, asterisk; Fig. 3.4.C, 48 s – 1 min 20 s, asterisk; Fig. 3.4.D, 48 s – 1 min 20 s, asterisk) and formed a transition zone that demarcated two distinct actin regions, one towards the AP with less actin density that the other one, towards the VP, with higher actin accumulation. Strikingly, this transition zone did not flow towards the VP immediately after the rupture of the cortex at the AP and it was only after 40 s - 1 min from the cortex tearing that this zone started flowing (Fig. 3.4.B, 1 min 36 s, arrow; Fig. 3.4.C, 1 min 36 s, arrow; Fig. 3.4.D, 1 min 36 s, arrow). This was also observed in the kymograph analysis (Fig. 3.5.B-B', asterisk) and suggests that this transition zone effectively creates a 'traffic jam' of actin accumulation that initially resists the cortical flows and the deformations induced by a contracting cortex.

We thus asked how this transition zone forms so that the cell can resist such deformations at the short time scales of the fast AV elongation. To answer this question, we looked at a mitochondria-rich subcortical layer, termed myoplasm, that has been proposed to accumulate at the CP[62] and play a role in the axis establishment during oocyte maturation and early development[63]. Maximum intensity projections of the myoplasm during the early stages of the fast AV elongation showed that the myoplasm was not homogenous throughout the oocyte. At the animal half of the unfertilized oocyte mitochondria within the myoplasm were organized in small dispersed clusters whereas at the vegetal half it appeared as a compacted thick layer (Fig. 3.7.A) deposited along the cortex. The transition zone between these two distinct domains within the myoplasm (Fig. 3.7.A, dotted line, top row) resembled the transition zone that we identified in the actin cortex during the early steps of the fast elongation of the AV axis upon fertilization (Fig. 3.7.A, dotted line, top row). When we overlaid the outline of the compacted myoplasm (i.e., the transition zone) with the actin signal (Fig. 3.7.A, dotted line, bottom row), it colocalized with the transition zone in the actin cortex during the time points preceding the onset of the actin cortical flows at 1 min 36 s post fertilization (Fig. 3.7.A, asterisk). This points to the possibility that the compacted layer of myoplasm is responsible for inducing the actin 'traffic jam' and therefore, an interplay between actin cortical flows and the myoplasm.

Myoplasm fluorescent intensity quantification along the cortex at these time points showed a region where intensity increases without net myoplasm displacement to the VP (Fig. 3.7.A, 1 min 4 s – 1 min 20 s, top row, asterisk; Fig. 3.7.B, 16 s – 1 min 20 s, asterisk). This zone coincided in time and space with the region in the actin cortex where, in a similar manner, actin intensity increased without flowing towards the VP (Fig. 3.7.A, 1 min 4 s – 1 min 20 s, bottom row, asterisk; Fig. 3.4.D, asterisk). Eventually, the actin cortex uncoupled from the myoplasm and started flowing towards the VP (Fig. 3.7.A, bottom row, big arrow; Fig. 3.4.D, arrow), however, the edge of the compacted myoplasm region showed only instantaneous displacement (i.e., no flows) as the position of the edge did not change after 1 min 36 s post fertilization (Fig. 3.7.A, 1 min 36 s – 1 min 52 s, top row, small arrow; Fig. 3.7.B, 1 min 36 s – 1

min 52 s, arrow). This suggests that the compacted region of the myoplasm is not subjected to the same polarizing flows as the actin cortex and it only deforms momentarily.

Altogether, these results support the notion that the actin transition zone that appears upon fertilization represents a sort of 'traffic jam' for actin flows. Moreover, the colocalization of the compacted region of the myoplasm and the accumulation of actin before the onset of cortical flows points to an interaction between the myoplasm and actin dynamics that governs the early stages of the fast AV oscillation by initially resisting the forces generated by the contracting actomyosin cortex and effectively preventing vegetal-ward flows during the fast elongation of the AV axis.

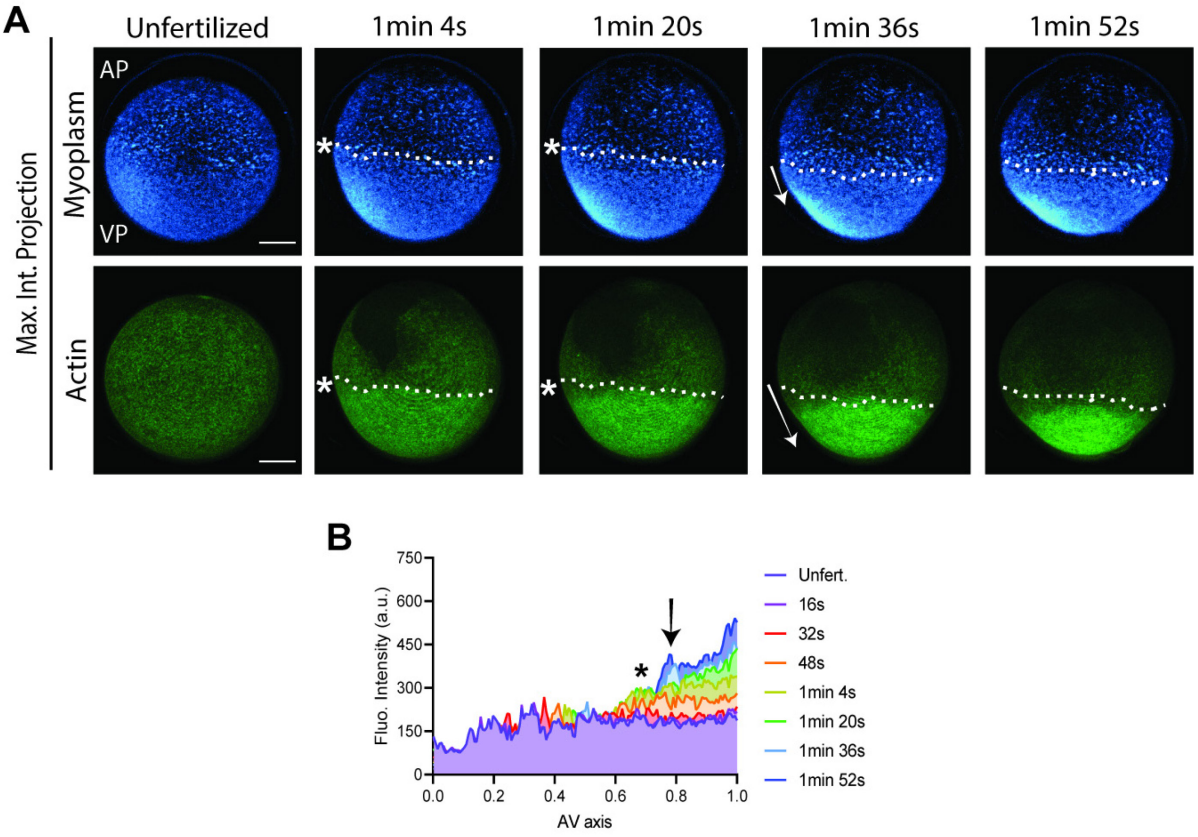

Fig. 3.7 – The compacted myoplasm layer resists the deformations of the actin cortex during the fast elongation of the AV axis. (**A**) Maximum intensity projections of confocal images of myoplasm (top row) and cortical actin (bottom row) during the fast AV elongation. AP is animal pole, VP is vegetal pole. Asterisk indicates the position of the transition zone (dotted line) in the myoplasm (top row) and actin cortex (bottom row), the arrows indicate the time where vegetal displacement is detected. The relative size of the arrows represents the relative vegetal displacement of the transition zone. Scale bar, 30 μm. (**B**) Line quantification of myoplasm intensity along the cortex during consecutive timepoints upon fertilization for one oocyte. The asterisk corresponds to the position of the myoplasm transition zone in A before the onset of flows at 1 min 36 s. Black arrow indicates the vegetal movement of the myoplasm transition zone also shown in A.

3.6 The myoplasm displays properties of a viscoelastic solid material

In the previous section, we showed that the myoplasm appears as a compacted layer only in the vegetal half of the oocyte (Fig. 3.7.A, top row). Coincidentally, upon fertilization the VP expands at a slightly slower rate and to less extent than the AP (Fig. 3.1.C", orange area, orange line). This supports our observations that the actomyosin-generated contractile forces are not enough to initially induce deformations of the compacted myoplasm. We thus hypothesized that the material properties of the myoplasm may play a role in controlling the fertilization-induced deformations (Fig. 3.1.B') by conferring the vegetal hemisphere of the oocyte mechanical resistance to the stresses generated by the contracting actomyosin cortex.

In order to further characterize the myoplasm, we first used transmitted electron microscopy to better understand its composition. Thin-section electron microscopy images of the VP of unfertilized oocytes confirmed previous work and showed that the myoplasm is a mitochondria-rich subcortical layer (Fig. 3.8.A)[14, 16] surrounded by a layer of cortical endoplasmic reticulum (cER) whose tubes and sheets cross the myoplasm from the cortex to the center of the oocyte, presumably forming an overall connected network (Fig. 3.8.A)[64]. 3D reconstruction of 50 serial sections of 70 nm thickness revealed that the mitochondria within the myoplasm did not form an interconnected mitochondrial network as in other systems[65-66] but that the myoplasm was formed by densely packed individual mitochondrion (Fig. 3.8.A'), similar to what has been reported in the Balbiani body of *Xenopus* and zebrafish oocytes[67-68]. In these organisms the Balbiani body has been described as a membrane-less amyloid-like aggregate[69] that displays solid-like properties[68]. Considering that the myoplasm resists the deformations that take place in the oocytes upon fertilization, we thus asked if the myoplasm of ascidian oocytes is also a solid-like layer.

In order to probe the material properties of the myoplasm, we performed UV laser ablations of the myoplasm in unfertilized oocytes (Fig. 3.8.B). Surprisingly, not only we did not observe recoil in the myoplasm upon laser ablation (Fig. 3.8.B, Post-cut - 0.2 s) – an indication that the myoplasm is either not under tension before fertilization or unable to transmit tensile forces –, but the gap induced by the laser did not close during the following 25 minutes (Fig. 3.8.B, Post-cut - 25 min; Fig. 3.8.B'). Given that a hallmark of solid materials is their inability to easily rearrange their components, we then proposed that the myoplasm might be a solid-like structure.

To test this possibility, we performed creep and recovery experiments using micropipette aspiration at the VP of unfertilized oocytes and of unfertilized oocytes treated with latrunculin B to remove the effect of the actin cortex (Fig. 3.8.C-C"). Viscosity values were significantly smaller in the latrunculin-treated oocytes, showing that we indeed were probing an actin-free cortex (Fig. 3.8.C"). We found that the initial elastic response in the actin-depolymerized oocyte to the aspiration was more pronounced than in the control (Fig. 3.8.C'). Strikingly, upon removal of the stress the latrunculin-treated oocyte was able to completely retract the aspirated cortex and recover its original shape (Fig. 3.8.C, bottom row, 13 min; Fig. 3.8.C'). This ability to gradually resume the original shape upon removal of a constant stress is a characteristic of a viscoelastic solid material[70]. This results strongly support our hypothesis that the myoplasm behaves as a solid-like material. However, the myoplasm is a relatively thin layer of mitochondria deposited along the cortex, therefore, it is technically very

challenging to access it for unequivocally probing its material properties. Consequently, we are collaborating with the Kreysing Group (MPI-CBG) in order to further elucidate the elastic or viscoelastic nature of the myoplasm using focused-light-induced cytoplasmic streaming (FLUCS)[71].

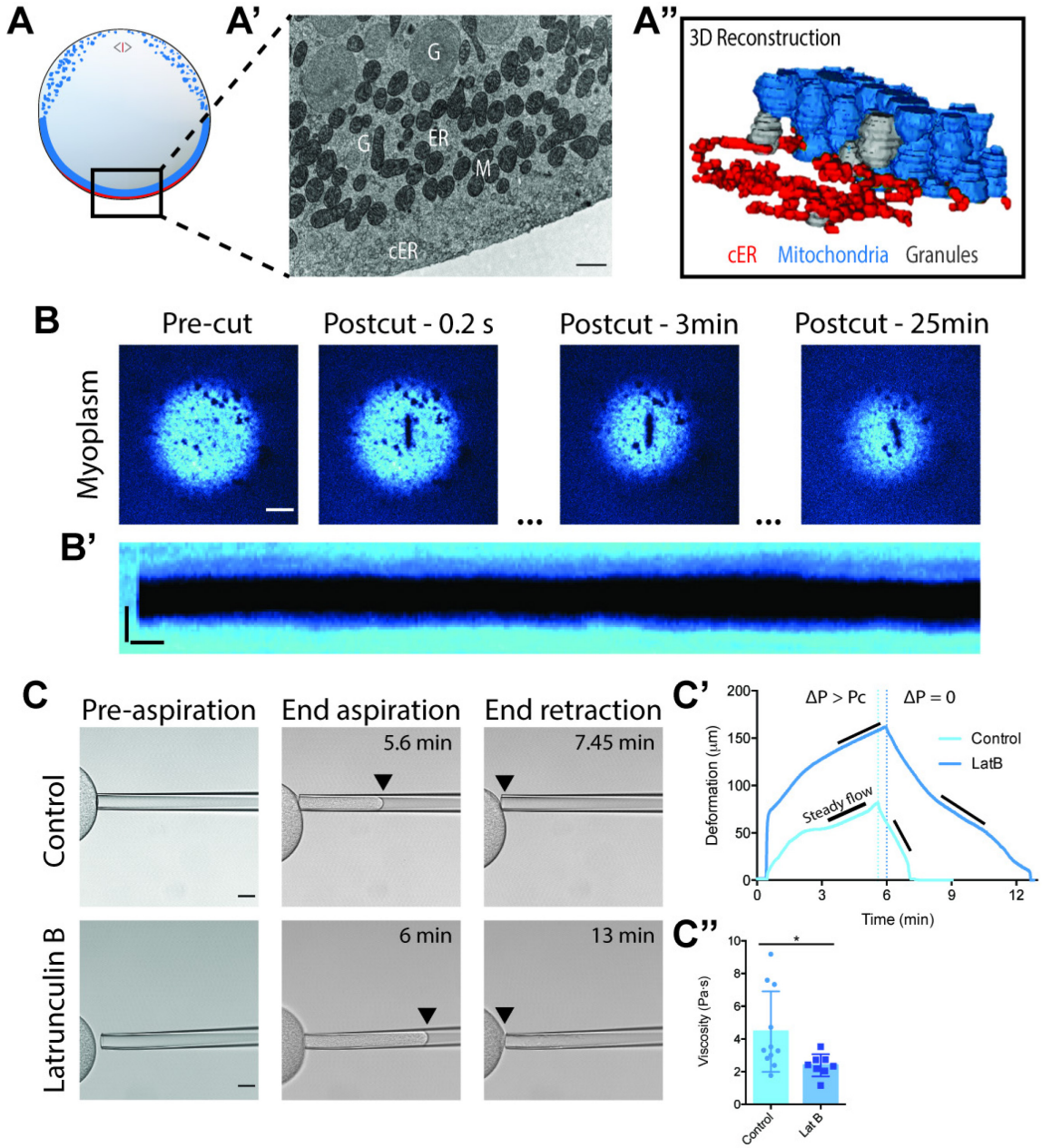

Fig. 3.8 – The myoplasm displays properties of a viscoelastic solid material. (**A**) Schematic representation of an unfertilized oocyte and the region imaged by TEM. (**A'**) Electron microscopy section of the vegetal region highlighted in A. cER is the cortical endoplasmic reticulum, M is mitochondria, G is granules and ER shows endoplasmic reticulum sheets within the myoplasm. Scale bar, 1 μm. Sample preparation and assistance with imaging was done by Vanessa Zheden and Daniel Gütl from the Electron Microscopy Facility at IST Austria. (**A"**) 3D reconstruction of 50 sections of 70 μm taken in the same region shown in A. Mitochondria in blue, cortical endoplasmic reticulum in red and granules in grey. For clarity, only cER from the first sections is shown. (**B**) Images of the myoplasm in unfertilized oocytes during UV laser ablation experiments. Scale bar, 15 μm. (**B'**) Exemplary kymograph of the myoplasm response to UV laser ablation during the first 8 minutes post cut. Horizontal scale bar, 5 s. Vertical scale bar 2 μm. (**C**) Brightfield images of before, during and at the end of creep and recovery micropipette aspirations in control and latrunculin B-treated unfertilized oocytes. The black arrow indicates how far the cortex has flown in the pipette. Scale bar, 30 μm. (**C'**) Exemplary curves of the length of the aspirated cortex over time. Black lines indicates the slopes of the linear steady flow of the cortex in the pipette. ΔP is the aspiration pressure (150 Pa for control, 100 Pa for latrunculin B). Pc is the critical pressure. (**C"**) Bar char of cortex viscosity calculated from the curves in C'. Mann Whitney test a*p = 0.0203. Error bars, SEM.

3.7 The myoplasm buckles at the vegetal pole due to the contracting actomyosin cortex and directs CP formation

Our previous observations on the myoplasm showed that a compacted layer of densely packed mitochondria (Fig. 3.8.A-A') initially resists the deformations imposed by the contracting cortex (Fig. 3.7). This behavior is compatible with a solid-like structure that requires forces to reach a certain threshold in order to deform. We therefore sought to further analyze the behavior of the myoplasm during the fast and slow phases of AV axis oscillations.

To that end, we first examined the dynamic distribution of the myoplasm during both the fast and slow AV deformations upon fertilization (Fig. 3.9.A). We observed that, as with actin and myosin, myoplasm fluorescent intensity decreased at the AP and increased at the VP shortly after fertilization during the fast AV oscillation phase (Fig. 3.9.B, orange area). After myoplasm fluorescent intensity peaked at the end of the fast shortening of the VP, it slowly equalized between the animal and vegetal halves of the zygote (Fig. 3.9.B, grey area), during the slow expansion of the VP, coinciding with CP formation.

The increase of myoplasm fluorescent intensity at the vegetal hemisphere upon fertilization is a surprising result considering that the myoplasm does not flow all the way to the VP (Fig. 3.7.B). Interestingly, we observed that at 3 mpf – when the vegetal cortex flattened (Fig. 3.1.C'-C") - the compacted myoplasm layer folded in a pattern resembling buckling of biological tissues under confinement[72] (Fig. 3.8.A, 3 mpf, arrow head). We identified buckles all along the compacted layer of the myoplasm but they were more pronounced at the point of maximum actin accumulation, that would latter form the CP. The multiple buckles increased the local density of myoplasm at the VP, explaining the increase of intensity that we detected (Fig. 3.9.B, orange area).

To characterize the buckling behavior of the myoplasm, we selected a set of angles at the vegetal half of the oocyte centered at the future CP and measured the length of the myoplasm along the buckles and the length of the underlying actin cortex (Fig. 3.9.C). Before fertilization the ratio of the length of the myoplasm to the length of actin was close to 1 (Fig. 3.9.C'), indicating that the myoplasm is perfectly deposited on top of the cortex. Upon fertilization, the ratio increased, reaching its maximum shortly before 3 mpf (Fig. 3.9.C', orange area) indicating that indeed the myoplasm buckled at the end of the fast AV oscillation, effectively increasing its length at the VP. Once the slow AV expansion phase started, the length ratio slowly returned to values close to the unfertilized ones (Fig. 3.9.C', grey area) thus indicating that the myoplasm straightens when the cortex relaxes. Interestingly, at 6 mpf, when the CP is the most expanded, the ratio was still greater than 1 suggesting that the myoplasm had not fully recovered its original shape.

Taking into account that the ratio of the lengths of the myoplasm to the actin cortex reached its maximum at 3 mpf, we proposed that the amplitude of the buckles would also be maximum at that time. We found that at 3 mpf the buckling amplitude was on average 15 μm (Fig. 3.9.D, 3 mpf), increasing the apparent thickness of the myoplasm by 3-fold[13]. Interestingly, at 6 mpf the buckling amplitude was still higher than before fertilization (10 μm

on average) further supporting the idea that the myoplasm is not fully extended at that time (Fig. 3.9.D, 6 mpf).

We also quantified the relative buckling frequency between the myoplasm and the underlying actin cortex (Fig. 3.9.D'). As expected from previous results, before fertilization the relative buckling frequency between the two layers was 1, indicating that the myoplasm and cortex are straight before fertilization. At 3 mpf, the relative buckling frequency increased to 3.2, strongly suggesting that when the actin cortex flattens at the VP, the myoplasm is more buckled. When the cortex relaxed and the oocyte returned to its almost spherical shape, the myoplasm was not perfectly straight anymore as some remaining buckles could be identified (the average relative buckling frequency was 1.9). Our results further confirm our observations that the myoplasm buckles at the VP at 3mpf when the actin cortex is the flattest and that it straightens during CP formation, returning almost to its original configuration by the end of the slow AV expansion phase.

Buckling is an example of an elastic instability in materials subjected to a compressive force that manifests as the appearance of orthogonal deformations to the main compressing direction[73]. The flattening at the VP is an indication of a contractile event[74-75]. This is supported by the sharp increase in cortical tension at the VP (Fig. 3.5.E') and the establishment of contractility-driven flows towards the VP concomitant to the increase in cortical tension (Fig. 3.5.B). We then hypothesized that the contracting actomyosin cortex compresses the myoplasm causing it to deform and eventually buckle. To test this hypothesis, we aimed to ectopically increase cortical tension locally in unfertilized oocytes by means of micropipette aspiration in order to induce local buckling of the myoplasm. We found that by using a small enough pipette (20 μm in diameter) and applying a constant pressure below the critical pressure during long times, we were able to buckle the myoplasm at the edges of the aspiration site (Fig. 3.9.E-E"), confirming our prediction that the myoplasm buckles under the compressing forces of the contracting actomyosin cortex.

Altogether, our results suggest that the myoplasm and its material properties play an important role in the cortical deformations of ascidian oocytes upon fertilization. We show that the fast AV oscillation upon fertilization depends on a calcium-induced increase in cortical tension that causes the actin cortex at the AP to rupture and quickly bulge out as a result of the release of tension along the AV axis. We propose that the solid-like myoplasm layer confers the vegetal half of the unfertilized oocyte with mechanical resistance to the deformations imposed by the release of tension along the AV axis upon fertilization therefore controlling the deformation of the VP during the fast AV expansion. Moreover, our results also suggest a role for the myoplasm in preventing the onset of actin flows during the early stages of the fast AV oscillation phase. We also show that the compacted myoplasm buckles at the VP at the end of the fast AV oscillation phase due to the compressing forces of the flowing actomyosin cortex. The ensuing relaxation of the vegetal cortex during the slow AV expansion phase together with the straightening of the myoplasm to, almost, its original position leads to CP formation, arguing for an additional role of the myoplasm in modulating all the deformations of the oocyte that we describe upon fertilization.

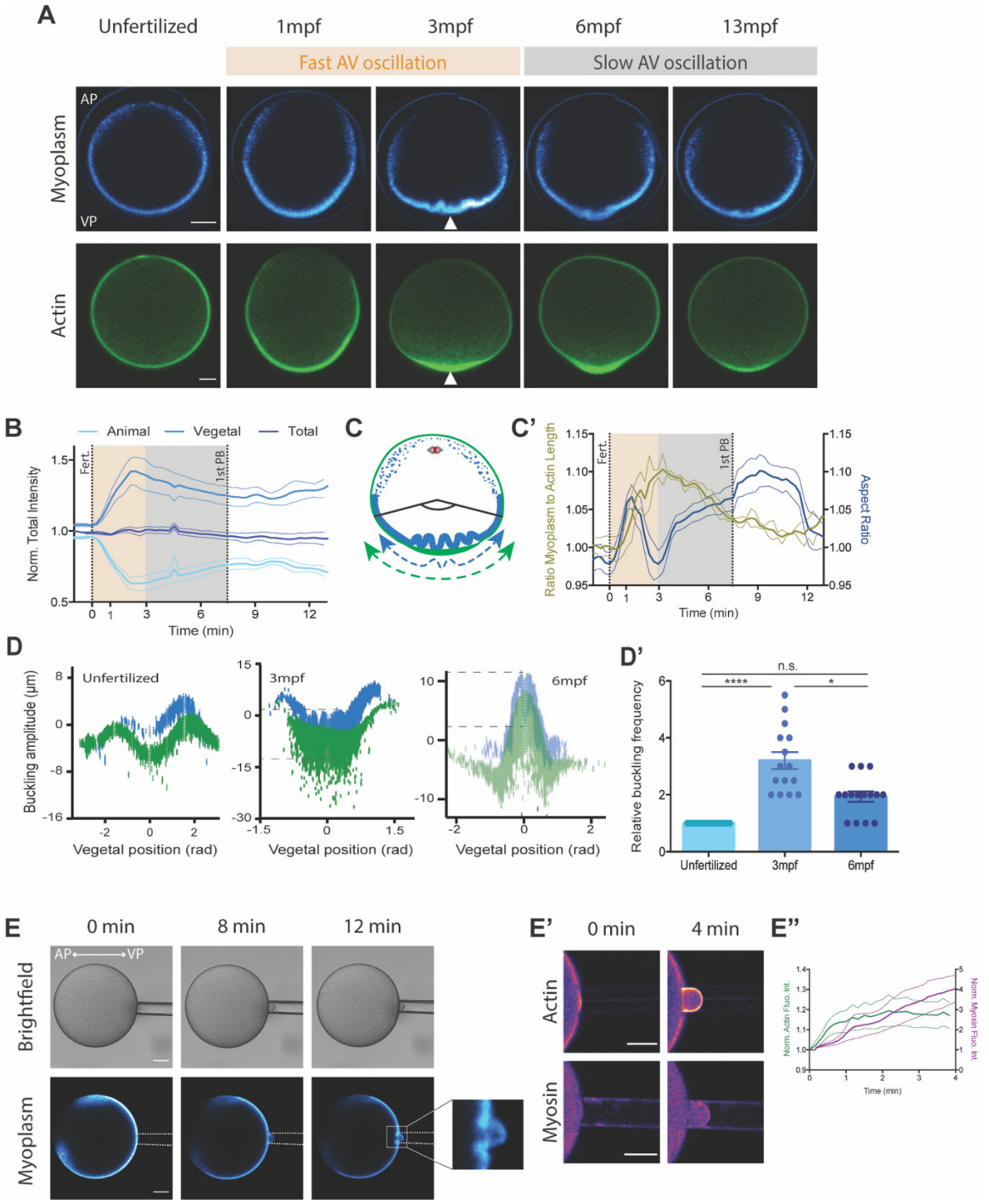

Fig. 3.9 – The myoplasm buckles at the VP at the end due to the contracting cortex. (**A**) Sum intensity projections over 10 central z-slides (15 µm) of ascidian oocytes/zygotes from unfertilized to 13 mpf with labeled myoplasm (top row) and expressing Utrophin-Venus to mark F-actin (bottom row). AP is animal pole, VP is vegetal pole. Arrow head indicates the buckles of the myoplasm and the flattening of the actin cortex. Scale bar, 30 µm. (**B**) Quantification of the total, animal and vegetal myoplasm fluorescent intensity in ascidian oocytes/zygotes from unfertilized to 13 mpf (N = 3 animals, n = 3 oocytes). Error bars, SEM. (**C**) Schematic illustration of the length analysis. Green arrow indicates the length of the actin cortex. The blue arrow indicates the length of the myoplasm along the buckles. (**C'**) Quantification of the ratio of the length of the myoplasm to the length of the actin cortex over time (N = 2 animals, n = 2 oocytes) overlaid with the aspect ratio from Fig. 3.1.B'. Error bars, SEM. Code generated by Gregory Szep. (**D**) Quantification of the buckling amplitude for actin (green) and myoplasm (blue) at 3 different time points (Unfertilized, 3 mpf

and 6 mpf). The x axis represents the position of the actin and myoplasm layers with respect to the CP (fixed at 0 radians). The horizonal dashed lines show the buckling amplitude of the myoplasm. (**D'**) Bar chart with the relative buckling frequency of myoplasm and actin layers at the same time points as in D. N = 9 animals, n = 15 oocytes. Friedman test and Dunn's multiple comparisons tests, n.s., not significant, *p = 0.0318, **** p < 0.0001. Error bars, SEM. (**E**) Confocal cross-section of brightfield (top row) and myoplasm channels (bottom row) of unfertilized oocytes during micropipette aspiration. AP is the animal pole, VP is the vegetal pole. The inset shows a zoom in of the buckled myoplasm at the aspiration site. Scale bar, 30 μm. (**E'**) Confocal images of unfertilized oocytes with actin (Utrophin-Venus) and myosin (iMyo-YFP) labelled. Scale bar, 30 μm. (**E"**) Quantification of normalized actin and myosin fluorescent intensity in E'. N = 2 animals, n = 4 oocytes for each condition. Error bars, SEM.

3.8 Fertilization-induced shape changes in the absence of myoplasm at the vegetal cortex of ascidian oocytes

In order to further understand the role of the myoplasm in modulating both the fast and slow AV oscillations upon fertilization, we designed an experiment in which we were able to locally displace the layer of compacted myoplasm from the cortex of unfertilized oocytes (Fig. 3.10.A). To that end, we centrifuged unfertilized oocytes in a continuous gradient of Ficoll® 400 in ASW for 1 h at 1500g. The oocytes were not oriented in any particular direction before fertilization thus, the resultant effect of the centrifugation was different in each oocyte depending on its relative orientation to the direction of the centrifugal force. Given that the cellular deformations we describe here are more pronounced at the VP, we only examined those oocytes in which the myoplasm was displaced from the vegetal-most cortex before fertilization (Fig. 3.10.B, Centrifuged). Our manipulation of the myoplasm did not have an effect on the cortical endoplasmic reticulum position (and presumably on the maternal determinants attached to it)[76], since we could detect it at the vegetal cortex of centrifuged oocytes before and after fertilization (Fig. 3.10.B).

In order to assess the role of the myoplasm in the fast and slow AV oscillations upon fertilization, we first examined the changes in cell shape that take place in the absence of a continuous layer of myoplasm along the vegetal cortex of the ascidian oocyte. As the non-centrifuged oocytes, the centrifuged ones were almost spherical before fertilization. The displacement of the myoplasm from the cortex was apparent from the clear cytoplasmic region that characterized the centrifuged oocytes (Fig. 3.11.A, top row, white arrow). Upon fertilization of centrifuged oocytes, the AV axis sharply shortened (Fig. 3.11.A, top layer, 1 min 20 s) – opposite to what we observed in control oocytes - and slightly expanded again but the oocyte never recovered the original shape (Fig. 3.11.A, top layer, 10 mpf). By the end of the first 13mpf, we could not consistently observe a structure resembling the CP in the every centrifuged oocyte. In the cases were a bulging of the VP was observed – that we identified as a pseudo-CP -, it appeared wider compared to the CP in control oocytes (Fig. 3.1.A) and not fully expanded (Fig. 3.11.A, top layer, 10mpf). This suggests that a continuous layer of compacted myoplasm is required for the observed changes in cell shape that we described in ascidian oocytes upon fertilization.

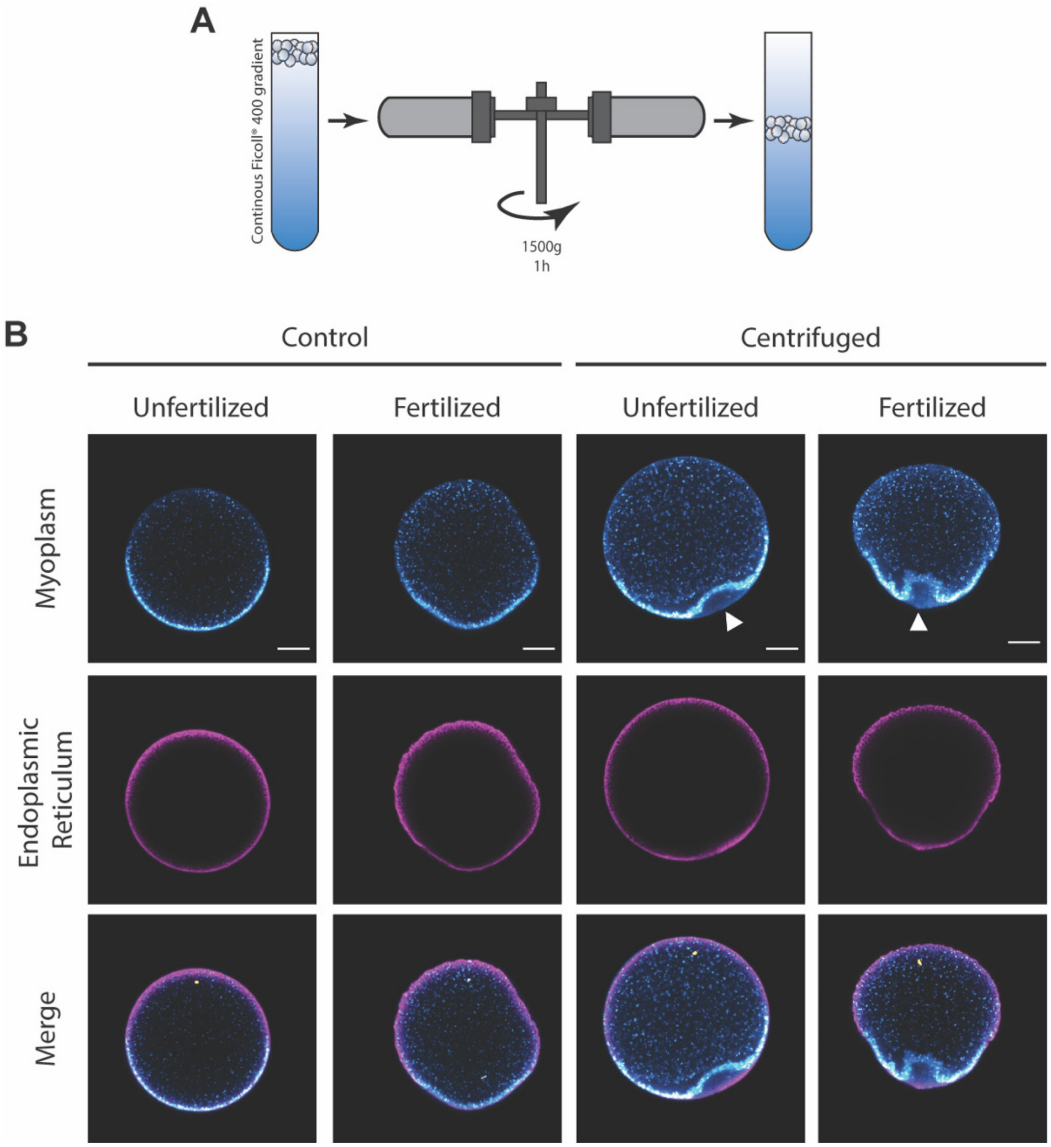

Fig. 3.10 – Immunostaining of centrifuged oocytes. (**A**) Schematic representation of the centrifugation experiment. (**B**) Confocal cross-sections of control and centrifuged oocytes stained for myoplasm, endoplasmic reticulum, and DNA. White arrow heads indicate the displacement of the myoplasm from the vegetal-most cortex. Scale bar, 30 μm.

Next, we described the deformations of the centrifuged oocytes in the same way as in control ones (Fig 3.1). Changes in the aspect ratio of centrifuged oocytes upon fertilization confirmed our observations that the AV axis shortened quickly upon fertilization (Fig. 3.11.B, pink line). This shortening occurred at a slightly faster rate than the fast expansion of the AV axis in control oocytes. However, contrary to the control, the aspect ratio of centrifuged oocytes did not recover its original value for the time we observed the oocytes. Interestingly, measurements of the distance of the animal and vegetal poles from the center of mass in centrifuged oocytes did not reveal any difference in the behavior between the animal and vegetal poles (Fig. 3.11.C) since both deformed in the same way. In summary, the VP in the absence of a continuous myoplasm displayed the same deformations as the AP suggesting that the myoplasm confers mechanical stability to the vegetal cortex, preventing it from

deforming as much as the AP in control oocytes. These results support the idea that the cellular deformations the ascidian oocyte is subjected to upon fertilization are severely affected when the myoplasm is not properly positioned along the vegetal cortex and that removal of that layer eliminates the fast and short AV oscillations, since we only observed a fast shortening of the AV axis.

We have shown that, in the non-centrifuged oocytes, the changes in shape during the *fast AV elongation* are mediated by a reorganization of the actin cortex and that the myoplasm affects such reorganizations. We thus wondered what was the spatiotemporal distribution of the actin cortex in oocytes with no myoplasm at the VP. Maximum actin intensity projections (Fig. 3.11.A, second row) of early time points following fertilization showed that actin was depleted from the AP and progressively accumulated at the VP similar to the non-centrifuged oocytes (Fig. 3.11.D). Moreover, fertilization also induced a rupture of the cortex at the AP of centrifuged oocytes (Fig. 3.11.A, second row, 48 s, asterisk). Interestingly, a second rupture of the cortex at the animal hemisphere was observed in some oocytes (Fig. 3.11.A, second row, 1 min 20 s, asterisks) further arguing for the role of the myoplasm in conferring mechanical stability to the cortex. We also found, consistent with observations in control oocytes, that the slight expansion of the AV axis – that in control oocytes leads to the appearance of a pseudo-CP – corresponded with a relaxation of the vegetal cortex as deducted from the loss of signal at 10 mpf (Fig. 3.11.D). These observations point to a contractility-driven vegetal accumulation of actin, as in control oocytes. Moreover, the occurrence of secondary cortical ruptures and the absence of proper CP formation in centrifuged oocytes further support our hypothesis that the myoplasm confers mechanical stability to the vegetal cortex during the fast AV oscillation phase and that it directs CP formation during the slow oscillation of the AV axis.

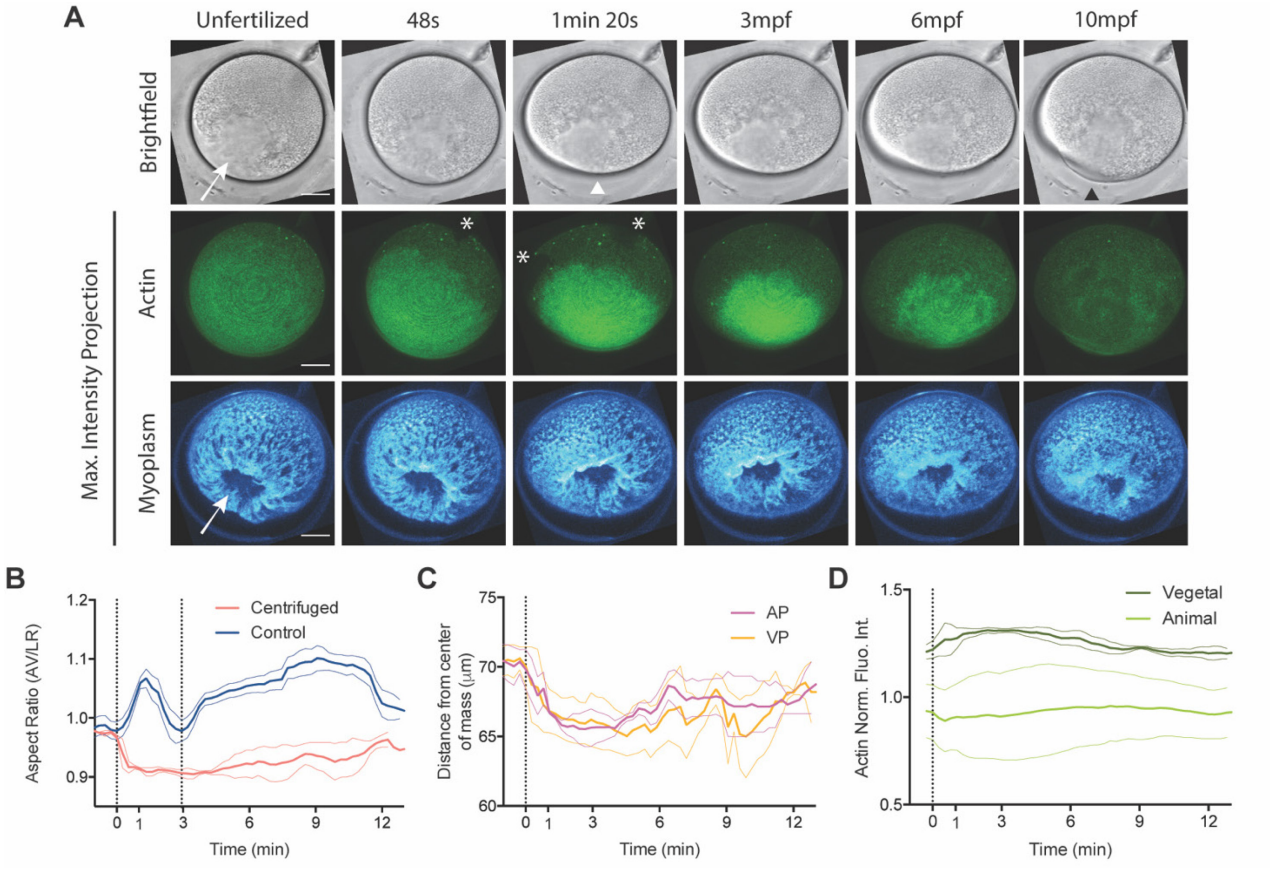

Fig. 3.11 – Shape changes upon fertilization are affected in centrifuged oocytes. (**A**) Brightfield confocal images and maximum intensity projections of actin and myoplasm of a representative centrifuged oocyte during the first 10 minutes following fertilization. White arrow head indicates flattening of the VP, black arrow head shows pseudo-CP, asterisks show ruptures of the actin cortex and white arrow shows the position of the displaced myoplasm after centrifugation. Scale bar, 30 μm. (**B**) Aspect ratio of control (blue line, taken from Fig. 3.1.B') and centrifuged oocytes (pink line) over time. Vertical line at 0 min indicates fertilization time-point. Vertical line at 3 min shows the time at which the control oocytes flatten at the VP. (**C**) Quantification of the distance from the animal and vegetal poles to the center of mass over time in centrifuged oocytes. (**D**) Quantification of the total actin intensity in the animal and vegetal halves of centrifuged ascidian oocytes from unfertilized to 13 mpf.
N = 3 animals, n = 3 oocytes. Error bars, SEM.

We previously speculated that there is an interplay between the myoplasm and the actin cortex and showed that the edge of the compacted myoplasm layer induces the formation of a transition zone in the actin cortex that resists the flows towards the VP (Fig. 3.4). Since we also observed such transition zone in fertilized centrifuged oocytes (Fig. 3.11.A), we hypothesized that a discontinuous myoplasm layer along the vegetal cortex does not prevent vegetal-ward flows of the actin cortex upon fertilization and, consequently, they would be established earlier. PIV and kymograph analysis showed that cortical flows of actin are also triggered upon fertilization (Fig. 3.12.B-B') in centrifuged oocytes but they are diminished compared to those in control cases (3 µm/min on average) (Fig. 3.12.B'). This supports the idea that the myoplasm plays a role in modulating the cortical actin flows that lead to the changes in cell shape we observe upon fertilization in ascidian oocytes. Line analysis of cortical actin during the initial time points following fertilization revealed that in the absence of a continuous layer of myoplasm along the vegetal cortex, cortical actin flows are established earlier than in non-centrifuged oocytes - within 30 to 40 s from fertilization (Fig. 3.12.C, black arrow) - and they are concomitant with the appearance of the cortical ruptures at the animal hemisphere (Fig. 3.12.A, asterisk; Fig. 3.12.C, asterisk). The onset of actin cortical flows also coincided with flows of the myoplasm to the vegetal along the cortex (Fig. 3.12.A, arrows and D, arrow) that were more prolonged in time compared to the vegetal displacement of intact myoplasm in non-centrifuged oocytes (Fig. 3.7). Moreover, since the myoplasm in centrifuged oocytes is not fully attached to the cortex, we could observe progressive accumulation of myoplasm in the cytoplasm of centrifuged oocytes as a consequence of the flows (Fig. 3.12.A, arrow head) that overlaid with regions of cytoplasmic actin accumulation (Fig. 3.12.A, top row).

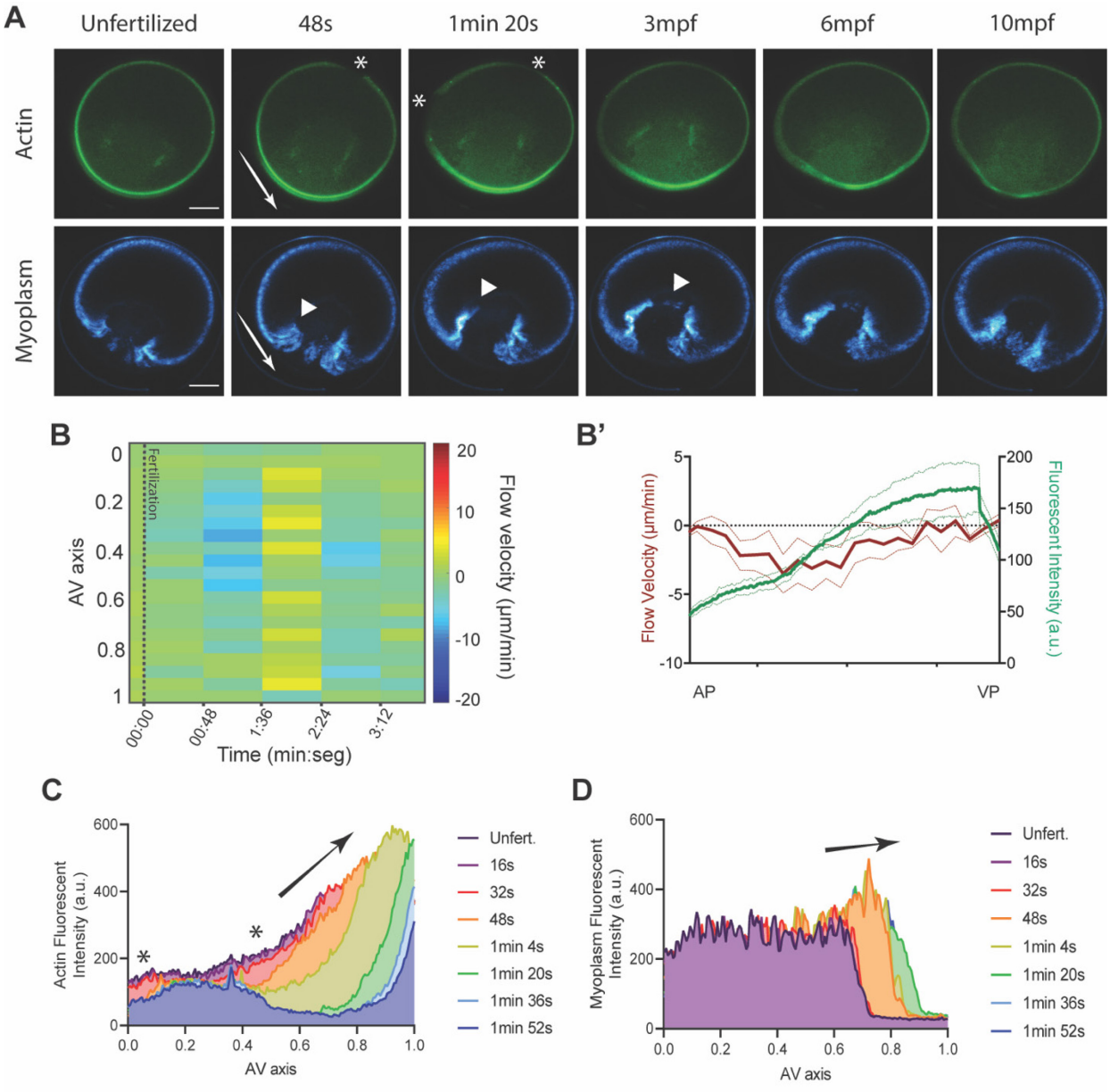

Fig. 3.12 – Cortical actin flows are established earlier if the myoplasm is not intact. (**A**) Sum actin (top row) and myoplasm (bottom row) intensity projections over 10 central z-sections (15 µm) of a representative centrifuged oocyte during the first 10 minutes following fertilization. White arrow indicates the onset of vegetal-ward flows, white arrow head shows cytoplasmic portions of the myoplasm and asterisks show ruptures of the actin cortex. Scale bar, 30 µm. (**B**) Kymograph of actin flow velocity along the AV axis in centrifuged oocytes. Color bar indicates velocity in µm/min (positive velocities towards the AP, negative velocities towards the VP). Code generated by Shayan Shamipour. (**B'**) Average actin flow velocity along the AV axis (red line, left axis) during the first timepoint that vegetal flows are visible. Actin intensity profile at the time of the flows is shown in green (right axis). N = 2 animals, n = 2 oocytes. Error bars, SEM. (**C-D**) Line quantification of actin (C) and myoplasm (D) intensity along the cortex during consecutive timepoints upon fertilization for one representative oocyte. The asterisk corresponds to the position of the cortex ruptures. Black arrow indicates the vegetal flows of actin and myoplasm.

4. Discussion and conclusions

Our data suggest a model in which a solid-like mitochondria-rich layer, in combination with the actomyosin cortex, displays a pleiotropic role in modulating the changes in cell shape that take place in ascidian oocytes upon fertilization.

In this project we first describe and quantify the changes in cell shape that the newly fertilized ascidian oocyte displays. We found that upon fertilization the animal-vegetal (AV) axis periodically elongates and shortens during the first minutes of development. We classify these oscillations according to their time scales: fertilization is followed by a fast AV lengthening-shortening cycle – termed *fast AV oscillation* and lasting on average 3 minutes – that is immediately succeeded by a slow AV elongation that eventually shortens to almost the unfertilized AV length – termed *slow AV oscillation* and it lasts 4 to 5 minutes. We also show that the actomyosin cortex is essential in mediating these cellular deformations and that it has a different mode of action in each oscillation.

In the *fast AV oscillation*, sperm entry at fertilization triggers a calcium wave within the oocyte that causes cortical tension to sharply increase. This creates a situation of cortical instability within the actomyosin cortex that ruptures at the animal pole (AP) - where it is weaker due to a local downregulation of actin density, presumably due to the presence of the meiotic spindle[14]. The rupture of the cortex at the AP then induces a sharp decrease of tension along the AV axis thus leading to the first change in cell shape: a fast elongation of the oocyte along the AV axis that is more pronounced at the AP. We propose that the rupture of the cortex at the AP together with the increase in cortical tension triggers an isotropic elastic contraction of the actomyosin cortex that leads to the establishment of contractility-driven polarizing cortical flows towards the vegetal pole (VP) and a dynamic density profile of the actomyosin cortex that would lead to the fast shortening of the AV axis due to flattening at the VP at the time of maximum actomyosin polarization.

These polarization of the cortex as a consequence of an increase in cortical tension resembles the polarization of the actomyosin cortex that cells and embryos display upon symmetry breaking[2, 53] and during cell migration[49, 77] and bleb formation[57, 78]. Moreover, the resultant elongated, pear-shape morphology of the oocyte during the fast AV expansion can be compared to that of fast migrating ameboid cells[49]. In these processes, changes in cell shape are the result of the inherent self-organizing properties of the cortex that can give rise to the establishment of cortical flows and pattern formation as a result of contractility-driven cortical instabilities[79].

Theoretical descriptions of cellular deformations have shed light into the force-generating mechanisms and the mechanical aspects of cellular deformations as well as the role they play in several biological process such as cell migration[80], cell division[81] and tissue morphogenesis[79]. We provide a quantitative description of the flow and actin density profiles that can be incorporated into current models and try to recapitulate the changes in cell shape that we observe during the first fast AV oscillation phase.

These models assume deformations in the presence of polarizing cortical flows as is the case for the fast AV oscillation upon fertilization in the ascidian oocyte. However, the second phase

of deformations, the *slow AV expansion*, takes place in the absence of cortical flows and during a local downregulation of cortical contractility, as evidenced by a loss of actin signal and a drop of the cortical tension at the VP. We found that cortical actomyosin accumulation decreases over time at the VP coinciding with the time that the contraction pole (CP) expands, suggesting that cortical relaxation of the vegetal cortex allows the CP to form. Previous studies in ascidians have proposed that the initial cortical contraction directly forms the CP[13]. Our results, in contrast, point to another mechanism in controlling CP formation by which local downregulation of cortical actomyosin would allow the VP to expand and form the CP. However, this alone might not be enough to reproduce the characteristic bell-shape of the CP.

A key finding in our study is that we identify a yet unknown role for the myoplasm - a layer of densely packed mitochondria that had previously been involved in symmetry breaking and polarization of the immature ascidian oocyte[6, 9]- in modulating the deformations of the ascidian zygote, in particular during CP formation. We show that, at the time when the vegetal cortex flattens, the myoplasm buckles due to the compressing forces from the polarized actomyosin cortex. Once the vegetal cortex relaxes, effectively releasing the myoplasm from the compression, the buckled myoplasm straightens back to its original shape. The observations of the myoplasm buckling and our laser ablation and micropipette aspiration experiments suggest that the myoplasm behaves like a solid layer, however, due to the position of the myoplasm - in close relation to the cortex - it is technically very challenging to access it in order to study its material properties and elucidate its viscoelastic or purely elastic nature. Non-invasive biophysical techniques like focused light-induced cytoplasmic streaming (FLUCS)[71] can be used to perform stress-strain experiments by creating thermo-viscous flows that would induce localized shear stress to the desired cellular structure and analyzing the resultant deformations[82]. Here, we postulate that CP formation is the result of the compressed myoplasm recovering from the deformation induced by the contracting actomyosin cortex, as oocytes in which the myoplasm has been displaced from the VP do not form a proper CP. However, this prediction needs to be tested with a mathematical model that incorporates the combined material properties of the actomyosin cortex and the myoplasm.

Our data also suggest an additional role for the myoplasm in resisting the deformations of the *fast AV oscillation* by conferring mechanical resistance to the cortex and interfering with the cortical actin flows. Upon rupture of the cortex at the AP following fertilization we identify a transition zone in the actin cortex that progressively accumulates actin but does not flow toward the VP. Since the transition zone of the actin cortex overlays with the beginning of the compacted layer of myoplasm, this points to the establishment of frictional forces between the myoplasm that behaves as a passive layer and buckles when the active layer, in this case the actomyosin cortex, contracts[83]. Our results suggest that the concentration profile of actin upon fertilization is then determined by the peeling effect of the actin cortical rupture, the ensuing cortical contraction and the friction with the myoplasm that needs to be overcome in order to induce any deformations of the vegetal hemisphere of the oocyte. The relative contributions of each component to the cellular deformations and eventually to CP formation need to be further studied with the development of a theoretical model.

The appearance of the transition zone and the overlay of the rich actin region with the compacted myoplasm further implies a mechanochemical interplay, not only mechanical, between the mitochondria and the actin cortex. Actin clouds and cables associated to mitochondria have been previously reported in yeasts and cultured cells[84-85]. Moreover, mitochondria have been shown to induce actin polymerization of both branched and filamentous networks, depending on the (de)polarization state of the mitochondria[86]. Interestingly, in centrifuged oocytes we observed localized regions of cytoplasmic actin accumulations that colocalized with the portion of the myoplasm that flows into the center of the oocyte. Indeed, in centrifuged oocytes the cortex to cytoplasmic ratio for total actin signal indicated a preferential cytoplasmic accumulation upon fertilization, coinciding with the time of the onset of flows and in contrast to what we reported in non-centrifuged oocytes (Fig. 4.1.A-B). We re-examined our data and could identify a transient cytoplasmic increase in actin signal in the VP coinciding with the maximum buckling of the myoplasm (Fig. 4.1.C) pointing to the idea that the myoplasm might be a source of local actin polymerization in ascidian oocytes. However, due to the autofluorescence of the myoplasm in the same wavelength as our actin marker and the crowded nature of the cytoplasm, we could not observe this polymerization event in every oocyte we examined and thus focused on the role of cortical actin. Our observations point to an interplay between the myoplasm and the actin cytoskeleton that determines the mechanochemical properties of the cortex by governing actin turnover or actin polymerization rates which have been shown to be sufficient to induce contractility-driven pattern formation[79]. How this interplay contributes to the polarization of the cortex and the changes in cell shape upon fertilization remains to be explored.

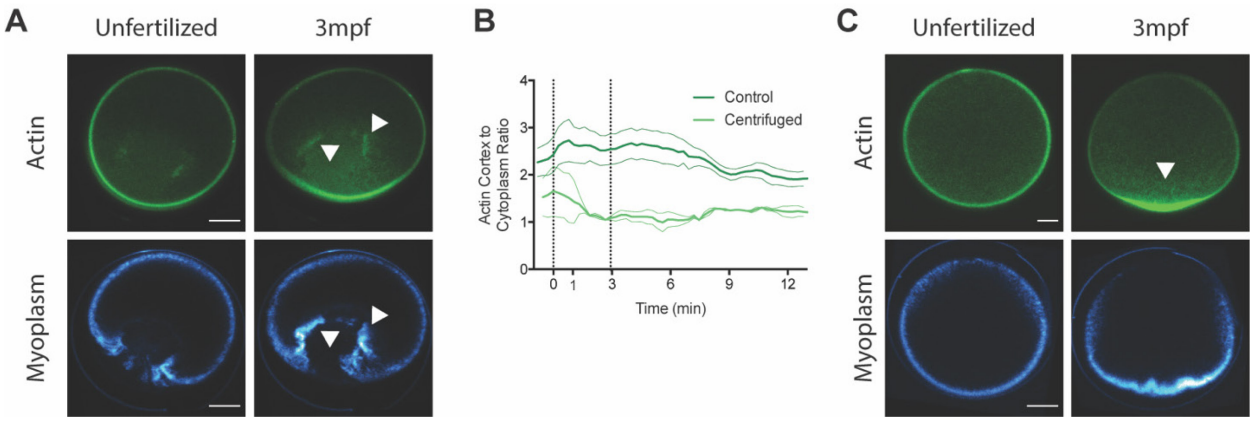

Fig. 4.1 – Cytoplasmic actin in centrifuged and non-centrifuged ascidian oocytes upon fertilization. (**A and C**) Sum actin (top row) and myoplasm (bottom row) intensity projections over 10 central z-sections (15 μm) of a representative centrifuged (A) and a control oocyte (C) before and 3 minutes post fertilization. Arrow heads indicate the cytoplasmic pool of actin colocalizing with the cytoplasmic portion of myoplasm. Scale bar, 30 μm. (**B**) Quantification of the ratio of cortical to cytoplasmic intensities for actin in control (N = 3 animals, n = 3 oocytes) and centrifuged oocytes (N = 2 animals, n = 2 oocytes) over time. Error bars, SEM.

The myoplasm in ascidians is deposited over a layer of cortical endoplasmic reticulum that is associated to maternal mRNAs and granules implicated in germ plasm formation[13]. The

presence of a mitochondrial cloud in one form or another has been reported in oocytes across the animal kingdom and in vertebrates it is known as the Balbiani body[87]. The fact that the myoplasm is a solid-like layer deposited along the vegetal cortex and is strongly deformed upon fertilization brings up the question of what keeps the individual mitochondria compacted in a singular layer in ascidian oocytes. It has been shown that in *Xenopus* and zebrafish oocytes the mitochondria in the Balbiani body are embedded in a protein matrix that forms an amyloid-like aggregate[69] identifiable by electron microscopy studies. Our observations of the myoplasm under the electron microscope did not reveal any obvious protein matrix accumulated within the highly ordered mitochondria in the myoplasm. Mass spectrometry analysis revealed that the most abundant protein in the Balbiani body of *Xenopus* and zebrafish oocytes was Xvelo and Bucky ball, respectively, two homolog proteins characterized by their ability to form amyloid-like aggregates due to their low complexity regions[88] suggesting that the Balbiani body is a phase separated entity[69]. Attempts to find an either sequence or domain homolog of the matrix proteins identified in *Xenopus* and zebrafish in ascidians were unsuccessful. Similar mass spectrometry analysis of the myoplasm are needed in order to identify what is the glue that keeps the mitochondria together in the ascidian oocyte.

4.1 The role of the contraction pole in morphogenesis

The development of ascidians has long been regarded as the main example of mosaic development, in which the differential inheritance of maternal factors will determine the fate of each blastomere[21, 89]. In fact, the fate map of the ascidian embryo development can be obtained from the 8-cell stage[90]. The fertilized egg of ascidian localizes the maternal determinants in two consecutive phases of ooplasmic segregation: the first phase – the main focus of this project - accumulates maternal mRNAs at the VP of the zygote in the CP. Following this, the second phase of ooplasmic segregation translocates some of the maternal determinants to the vegetal posterior region of the zygote before the first cell cleavage, thereby bisecting the cytoplasm of the zygote that contains the myoplasm and the future CAB[16]. These consecutive reorganizations of the ooplasm direct the establishment of the anterior-posterior, dorsal-ventral and left-right axes before the first cell division[21]. The embryo continues to divide following a series of stereotypical cleavages, reaching the gastrula stage at the 110-cell stage when the developmental fate of the blastomere becomes restricted[91]. Therefore, it is crucial to understand the processes that lead to maternal determinants segregation in order to have wholesome view of embryonic development in ascidians.

The events and cellular deformations that we describe here take place during the traditionally called first phase of ooplasmic segregation in which a cortical contraction was proposed to lead to the formation of the CP that would accumulate, presumably via advective flows, the maternal determinants for endoderm and mesoderm-derived tissues and morphogenic determinants, namely, unequal cleavage and gastrulation[92]. In seminal studies, Nishida performed CP ablations and observed that ablated embryos failed to gastrulate and exhibited a radial cleavage pattern. These embryos also failed to specify vegetal cell fates as they lacked

endoderm, muscle and notochord tissues[22], arguing for a morphogenic role of the CP. However, these experiments did not interfere with CP formation.

In this project we were able to interfere with CP formation in two ways. First we overexpressed a constitutively active version of myosin phosphatase (CaMypt) in order to downregulate myosin contractility. These oocytes did not form a proper CP upon fertilization due to the downregulation of myosin contractility and, similar to what Nishida reported in CP-ablated embryos, the embryos failed to properly established the embryonic axis (Fig. 4.2). However, careful examination into the developmental pattern and maternal determinants localization is needed in these embryos to establish whether maternal mRNAs were localized to the VP upon fertilization.

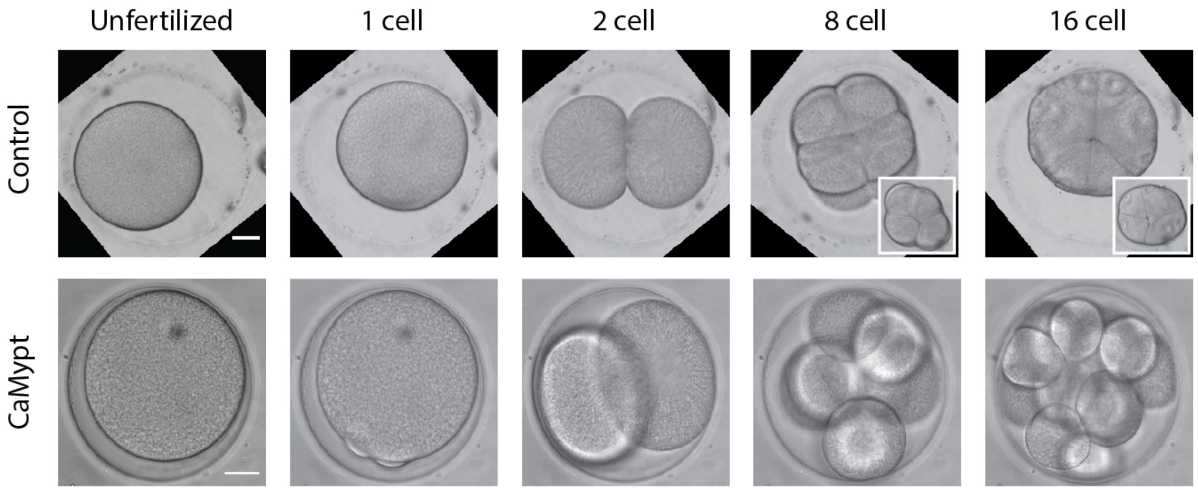

Fig. 4.2 – Cleavage pattern is affected in CaMypt-injected embryos. Brightfield confocal images of control and CaMypt-injected embryos until the 16-cell stage. Insets are lateral views of the embryo.

Genetic or pharmacological treatments that interfere with the actomyosin cortex during CP formation have a global effect in the oocyte and affect other processes during early development such as polar body extrusion, spindle orientation and cytokinesis and are, therefore, difficult to interpret in the context of CP formation and its role in morphogenesis. We established another way of interfering with CP, by centrifugation of unfertilized oocytes in order to displace the myoplasm from the cortex. In these oocytes, we could still observe the localization of cortical ER at the vegetal cortex upon fertilization, arguing that the maternal determinants were also properly localized in the absence of CP. Moreover, most of the centrifuged oocytes developed beyond the first cleavage, most of them reaching, at least, the gastrula stage. Given the variability of the centrifuged oocytes in terms of the portion of displaced myoplasm, it is difficult to assess if the failure to develop of centrifuged oocytes is due to the new position of the myoplasm or a collateral effect of centrifugation.

The question remains as to whether the CP is a functional structure in the fertilized oocyte of ascidian embryos or it forms as a consequence of the self-organizing and mechanical properties of the actomyosin cortex and the advective flows that accumulate cortical endoplasmic reticulum and maternal determinants.

Appendix A

A Fitting Buckles in two Dimensions

We begin by binarizing an equatorial confocal section of the actin and myoplasm signals from a time-lapse with the Otsu algorithm [1]. Let us represent the resultant time-lapse as four dimensional images with channel and spatial axis in the rst three dimensions and time in the last dimension (c; x; y; t). The binarized image can be represented as a four dimensional array of Boolean values

$$\mathrm{X}\,[c, x, y, t]$$

To prepare the data for fitting, we extract the spatial cartesian coordinates in the binarized image for which the pixel values are set to **True** . This gives us a list of coordinates $x; y$ in μm for each time point t and channel c

$$\mathcal{D}[c, t] := \; argmax_{x,y}\, \mathrm{X}\,[c, x, y, t]$$

The cartesian coordinates $\mathcal{D}[c, t]$ are used as input data for finding ellipses using a matrix diagonalization method that is robust to noise [2]. This way the quality of the binarization does not have an impact on the estimated ellipse parameters. Successful fits yield ellipse parameters for each channel c and time t

Ellipse Parameters	Description
a, b	Semi-major and minor axis length
x_0, y_0	Origin
θ	orientation

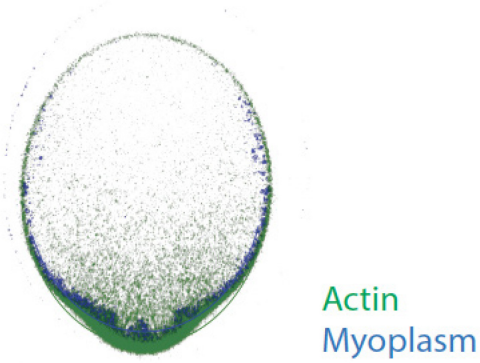

Figure A.1: Ellipse boundary on top of binarized data, revealing first-order approximations to centre of mass, orientation and eccentricity. Green represents the actin cortex and blue the myoplasm layer.

This gives us a first-order approximation to the centre of mass, orientation and eccentricity of the actin cortex and myoplasm layers within the oocyte (Figure A.1). However these parameters do not tell us anything about the buckling of the layers, fitting of which is cumbersome in cartesian coordinates. The ellipse parameters allow us to transform the noisy binarized image into co-moving elliptical coordinates

$$\mathrm{X}\,[c, r, \theta, t]$$

Where θ becomes the position along the cortex (centred around the contraction pole) and r becomes the amplitude of the buckles (Figure A.2). Viewing the data in this coordinate frame simplifies the task of fitting the buckles. As before we extract spatial coordinates, this time in the co-moving elliptical frame, by looking for pixel values that are set to **True**

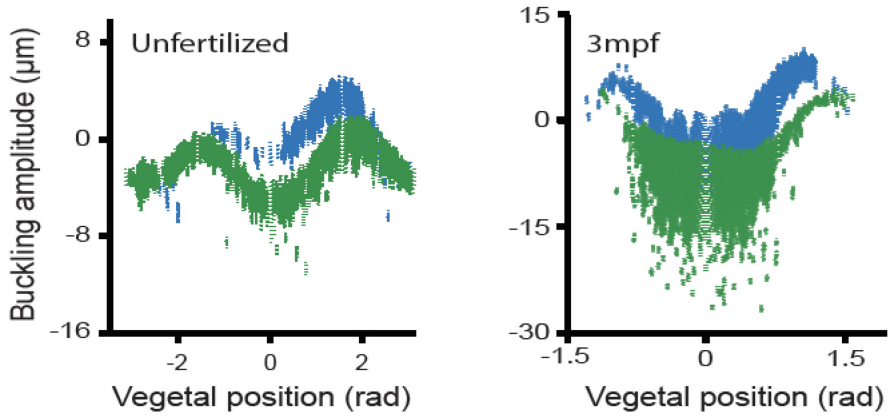

Figure A.2: Representation of the buckling amplitude as a function of the position along the vegetal cortex. Actin cortex in green and myoplasm in blue.

$$\mathcal{P}[c,t] := argmax_{r,\theta}\, \mathrm{X}\,[c,r,\theta,t]$$

We fit the buckles independently for each time point t and channel c with Gaussian basis functions in the (r,θ) plane using linear regression. This is done by minimizing the objective

$$\sum_{r,\theta\in\mathcal{P}[c,t]}\left|r - f_{[c,t]}(\theta)\right|^2 \quad \text{where} \quad f_{[c,t]}(\theta) = \sum_{\phi}\omega_{\phi}[c,t]\, e^{\left(\frac{\theta-\phi}{\sigma}\right)^2}$$

Here the model for the buckles $f_{[c,t]}(\theta)$ is a superposition of Gaussian basis functions at different locations along the cortex ϕ of typical width σ. The hyperparameter σ is chosen to adapt to the typical persistence length of a layer.

While the binarization can be noisy for finding the ellipse parameters, the task of fitting buckles requires cleaner data. To this end, morphological opening/closing image transformations are applied to de-noise the data before applying regression.

References

[1] N. Otsu, “A Threshold Selection Method from Gray-Level Histograms” IEEE Transactions on Systems, Man, and Cybernetics , vol. 9, 1 1979.

[2] A. Fitzgibbon, M. Pilu, and R. Fisher, “Direct least square fitting of ellipses” IEEE Transactions on Pattern Analysis and Machine Intelligence , vol. 21, 5 1999.

References

1. Luby-Phelps, K., The physical chemistry of cytoplasm and its influence on cell function: an update. *Mol Biol Cell* **2013,** *24* (17), 2593-2596.
2. Illukkumbura, R.; Bland, T.; Goehring, N. W., Patterning and polarization of cells by intracellular flows. *Current Opinion in Cell Biology* **2020,** *62*, 123-134.
3. Singh, D.; Odedra, D.; Dutta, P.; Pohl, C., Mechanical stress induces a scalable switch in cortical flow polarization during cytokinesis. *Journal of Cell Science* **2019,** *132* (19).
4. Schuh, M.; Ellenberg, J., A New Model for Asymmetric Spindle Positioning in Mouse Oocytes. *Current Biology* **2008,** *18* (24), 1986-1992.
5. Lénárt, P.; Bacher, C. P.; Daigle, N.; Hand, A. R.; Eils, R.; Terasaki, M.; Ellenberg, J., A contractile nuclear actin network drives chromosome congression in oocytes. *Nature* **2005,** *436* (7052), 812-818.
6. Prodon, F.; Sardet, C.; Nishida, H., Cortical and cytoplasmic flows driven by actin microfilaments polarize the cortical ER-mRNA domain along the a–v axis in ascidian oocytes. *Developmental biology* **2008,** *313*, 682-699.
7. Lemaire, P., Unfolding a chordate developmental program, one cell at a time: Invariant cell lineages, short-range inductions and evolutionary plasticity in ascidians. *Developmental Biology* **2009,** *332* (1), 48-60.
8. Lemaire, P.; Smith, W. C.; Nishida, H., Ascidians and the Plasticity of the Chordate Developmental Program. *Current Biology* **2008,** *18*, R620-R631.
9. Prodon, F.; Chenevert, J.; Sardet, C., Establishment of animal–vegetal polarity during maturation in ascidian oocytes. *Developmental Biology* **2006,** *290* (2), 297-311.
10. McDougall, A.; Chenevert, J.; Lee, K.; Hebras, C.; Dumollard, R., Cell Cycle in Ascidian Eggs and Embryos. *Results and problems in cell differentiation* **2011,** *53*, 153-169.
11. Silvestre, F.; Gallo, A.; Cuomo, A.; Covino, T.; Tosti, E., Role of cyclic AMP in the maturation of Ciona intestinalis oocytes. *Zygote (Cambridge, England)* **2011,** *19*, 365-371.
12. Li, H.; Guo, F.; Rubinstein, B.; Li, R., Actin-driven chromosomal motility leads to symmetry breaking in mammalian meiotic oocytes. *Nature Cell Biology* **2008,** *10* (11), 1301-1308.
13. Sardet, C.; Paix, A.; Prodon, F.; Dru, P.; Chenevert, J., From oocyte to 16-cell stage: Cytoplasmic and cortical reorganizations that pattern the ascidian embryo. *Developmental Dynamics* **2007,** *236* (7), 1716-1731.
14. Sardet, C.; Speksnijder, J.; Terasaki, M.; Chang, P., Polarity of the ascidian egg cortex before fertilization. *Development* **1992,** *115* (1), 221-237.
15. Tokuhisa, M.; Muto, M.; Nishida, H., Eccentric position of the germinal vesicle and cortical flow during oocyte maturation specify the animal-vegetal axis of ascidian embryos. *Development* **2017,** *144* (5), 897-904.
16. Roegiers, F.; Djediat, C.; Dumollard, R.; Rouviere, C.; Sardet, C., Phases of cytoplasmic and cortical reorganizations of the ascidian zygote between fertilization and first division. *Development* **1999,** *126* (14), 3101-3117.
17. Whitaker, M., Calcium at fertilization and in early development. *Physiol Rev* **2006,** *86* (1), 25-88.
18. Roegiers, F.; McDougall, A.; Sardet, C., The sperm entry point defines the orientation of the Ca2+-induced contraction wave that directs the first phase of cytoplasmic

reorganization in the ascidian egg. *Development (Cambridge, England)* **1995,** *121*, 3457-3466.
19. Dumollard, R.; Sardet, C., Three different calcium wave pacemakers in ascidian eggs. *Journal of cell science* **2001,** *114*, 2471-2481.
20. Prodon, F.; Yamada, L.; Shirae-Kurabayashi, M.; Nakamura, Y.; Sasakura, Y., Postplasmic/PEM RNAs: A class of localized maternal mRNAs with multiple roles in cell polarity and development in ascidian embryos. *Developmental Dynamics* **2007,** *236* (7), 1698-1715.
21. Nishida, H., Specification of embryonic axis and mosaic development in ascidians. *Developmental Dynamics* **2005,** *233* (4), 1177-1193.
22. Nishida, H., Vegetal egg cytoplasm promotes gastrulation and is responsible for specification of vegetal blastomeres in embryos of the ascidian Halocynthia roretzi. *Development* **1996,** *122* (4), 1271-1279.
23. Nishida, H., Localization of egg cytoplasm that promotes differentiation to epidermis in embryos of the ascidian Halocynthia roretzi. *Development* **1994,** *120* (2), 235-243.
24. Weiser, D. C.; Row, R. H.; Kimelman, D., Rho-regulated Myosin phosphatase establishes the level of protrusive activity required for cell movements during zebrafish gastrulation. *Development* **2009,** *136* (14), 2375-2384.
25. Schindelin, J.; Arganda-Carreras, I.; Frise, E.; Kaynig, V.; Longair, M.; Pietzsch, T.; Preibisch, S.; Rueden, C.; Saalfeld, S.; Schmid, B.; Tinevez, J.-Y.; White, D. J.; Hartenstein, V.; Eliceiri, K.; Tomancak, P.; Cardona, A., Fiji: an open-source platform for biological-image analysis. *Nature Methods* **2012,** *9* (7), 676-682.
26. Sommer, C.; Straehle, C.; Köthe, U.; Hamprecht, F. A. In *Ilastik: Interactive learning and segmentation toolkit*, 2011 IEEE International Symposium on Biomedical Imaging: From Nano to Macro, 30 March-2 April 2011; 2011; pp 230-233.
27. Thielicke, W.; Stamhuis, E. J., PIVlab – Towards User-friendly, Affordable and Accurate Digital Particle Image Velocimetry in MATLAB. *Journal of Open Research Software* **2014,** *2*.
28. Gibson, D. G.; Young, L.; Chuang, R.-Y.; Venter, J. C.; Hutchison, C. A.; Smith, H. O., Enzymatic assembly of DNA molecules up to several hundred kilobases. *Nature Methods* **2009,** *6* (5), 343-345.
29. Roure, A.; Rothbächer, U.; Robin, F.; Kalmar, E.; Ferone, G.; Lamy, C.; Missero, C.; Mueller, F.; Lemaire, P., A Multicassette Gateway Vector Set for High Throughput and Comparative Analyses in Ciona and Vertebrate Embryos. *PLOS ONE* **2007,** *2* (9), e916.
30. Mastop, M.; Bindels, D. S.; Shaner, N. C.; Postma, M.; Gadella, T. W. J.; Goedhart, J., Characterization of a spectrally diverse set of fluorescent proteins as FRET acceptors for mTurquoise2. *Scientific Reports* **2017,** *7* (1), 11999.
31. Yasuo, H.; McDougall, A., Practical Guide for Ascidian Microinjection: Phallusia mammillata. *Advances in Experimental Medicine and Biology* **2018,** *1029*, 15-24.
32. Godard, B. G.; Dumollard, R.; Munro, E.; Chenevert, J.; Hebras, C.; McDougall, A.; Heisenberg, C.-P., Apical Relaxation during Mitotic Rounding Promotes Tension-Oriented Cell Division. *Developmental Cell* **2020,** *55* (6), 695-706.e694.
33. Guevorkian, K.; Colbert Mj Fau - Durth, M.; Durth M Fau - Dufour, S.; Dufour S Fau - Brochard-Wyart, F.; Brochard-Wyart, F., Aspiration of biological viscoelastic drops. *Physical Review Letter* **2010,** *104* (21), 1079-7114.
34. Guevorkian, K.; Maître, J. L., Micropipette aspiration: A unique tool for exploring cell and tissue mechanics in vivo. *Methods in Cell Biology* **2017,** *139*, 187-201.

35. Petridou, N. I.; Grigolon, S.; Salbreux, G.; Hannezo, E.; Heisenberg, C.-P., Fluidization-mediated tissue spreading by mitotic cell rounding and non-canonical Wnt signalling. *Nature Cell Biology* **2019,** *21* (2), 169-178.
36. Smutny, M.; Behrndt, M.; Campinho, P.; Ruprecht, V.; Heisenberg, C., UV Laser Ablation to Measure Cell and Tissue-Generated Forces in the Zebrafish Embryo In Vivo and Ex Vivo. *Methods in molecular biology* **2015,** *1189*, 219-235.
37. Mueller, J.; Szep, G.; Nemethova, M.; de Vries, I.; Lieber, A. D.; Winkler, C.; Kruse, K.; Small, J. V.; Schmeiser, C.; Keren, K.; Hauschild, R.; Sixt, M., Load Adaptation of Lamellipodial Actin Networks. *Cell* **2017,** *171* (1), 188-200.e116.
38. Shamipour, S.; Kardos, R.; Xue, S.-L.; Hof, B.; Hannezo, E.; Heisenberg, C.-P., Bulk Actin Dynamics Drive Phase Segregation in Zebrafish Oocytes. *Cell* **2019,** *177* (6), 1463-1479.e1418.
39. Reipert, S.; Goldammer, H.; Richardson, C.; Goldberg, M. W.; Hawkins, T. J.; Hollergschwandtner, E.; Kaufmann, W. A.; Antreich, S.; Stierhof, Y.-D., Agitation Modules: Flexible Means to Accelerate Automated Freeze Substitution. *J Histochem Cytochem* **2018,** *66* (12), 903-921.
40. Goldammer, H.; Hollergschwandtner, E.; Elisabeth, N. H.; Frade, P. R.; Reipert, S., Automatized Freeze Substitution of Algae Accelerated by a Novel Agitation Module. *Protist* **2016,** *167* (4), 369-376.
41. Marikawa, Y.; Yoshida, S.; Satoh, N., Development of Egg Fragments of the Ascidian Ciona savignyi: The Cytoplasmic Factors Responsible for Muscle Differentiation Are Separated into a Specific Fragment. *Developmental Biology* **1994,** *162* (1), 134-142.
42. Marikawa, Y.; Satoh, N., Gray and Red Fragments of the Egg of the Ascidian Ciona savignyi: Preferential Development of Muscle Cells from Gray Fragments. *Development, Growth & Differentiation* **1991,** *33* (4), 307-316.
43. Speksnijder, J. E., The repetitive calcium waves in the fertilized ascidian egg are initiated near the vegetal pole by a cortical pacemaker. *Developmental Biology* **1992,** *153* (2), 259-271.
44. Sardet, C.; McDougall A Fau - Yasuo, H.; Yasuo H Fau - Chenevert, J.; Chenevert J Fau - Pruliere, G.; Pruliere G Fau - Dumollard, R.; Dumollard R Fau - Hudson, C.; Hudson C Fau - Hebras, C.; Hebras C Fau - Le Nguyen, N.; Le Nguyen N Fau - Paix, A.; Paix, A., Embryological methods in ascidians: the Villefranche-sur-Mer protocols. *Methods in molecular biology* **2011,** *770*, 365-400.
45. Dumollard, R.; McDougall, A.; Rouvière, C.; Sardet, C., Fertilisation calcium signals in the ascidian egg. *Biology of the Cell* **2004,** *96* (1), 29-36.
46. Speksnijder, J.; Sardet, C.; Jaffe, L., The activation wave of calcium in the ascidian egg and its role in ooplasmic segregation. *The Journal of Cell Biology* **1990,** *110*, 1589 - 1598.
47. Nizak, C.; Martin-Lluesma, S.; Moutel, S.; Roux, A.; Kreis, T. E.; Goud, B.; Perez, F., Recombinant Antibodies Against Subcellular Fractions Used to Track Endogenous Golgi Protein Dynamics in Vivo. *Traffic* **2003,** *4* (11), 739-753.
48. Paluch, E.; Piel, M.; Prost, J.; Bornens, M.; Sykes, C., Cortical Actomyosin Breakage Triggers Shape Oscillations in Cells and Cell Fragments. *Biophysical Journal* **2005,** *89* (1), 724-733.
49. Ruprecht, V.; Wieser, S.; Callan-Jones, A.; Smutny, M.; Morita, H.; Sako, K.; Barone, V.; Ritsch-Marte, M.; Sixt, M.; Voituriez, R.; Heisenberg, C.-P., Cortical Contractility Triggers a Stochastic Switch to Fast Amoeboid Cell Motility. *Cell* **2015,** *160* (4), 673-685.

50. Carvalho, K.; Tsai, F.-C.; Lees, E.; Voituriez, R.; Koenderink, G. H.; Sykes, C., Cell-sized liposomes reveal how actomyosin cortical tension drives shape change. *Proceedings of the National Academy of Sciences* **2013,** *110* (41), 16456.
51. Speksnijder, J. E.; Jaffe, L. F.; Sardet, C., Polarity of sperm entry in the ascidian egg. *Developmental Biology* **1989,** *133* (1), 180-184.
52. Zhao, P.; Teng, X.; Tantirimudalige, S. N.; Nishikawa, M.; Wohland, T.; Toyama, Y.; Motegi, F., Aurora-A Breaks Symmetry in Contractile Actomyosin Networks Independently of Its Role in Centrosome Maturation. *Developmental Cell* **2019,** *48* (5), 631-645.e636.
53. Munro, E.; Nance, J.; Priess, J. R., Cortical Flows Powered by Asymmetrical Contraction Transport PAR Proteins to Establish and Maintain Anterior-Posterior Polarity in the Early C. elegans Embryo. *Developmental Cell* **2004,** *7* (3), 413-424.
54. Santella, L.; Lim, D.; Moccia, F., Calcium and fertilization: the beginning of life. *Trends in Biochemical Sciences* **2004,** *29* (8), 400-408.
55. Stack, C.; Lucero, A. J.; Shuster, C. B., Calcium-responsive contractility during fertilization in sea urchin eggs. *Dev Dyn* **2006,** *235* (4), 1042-1052.
56. Carvalho, K.; Lemière, J.; Faqir, F.; Manzi, J.; Blanchoin, L.; Plastino, J.; Betz, T.; Sykes, C., Actin polymerization or myosin contraction: Two ways to build up cortical tension for symmetry breaking. *Philosophical transactions of the Royal Society of London. Series B, Biological sciences* **2013,** *368*, 20130005.
57. Tinevez, J.-Y.; Schulze, U.; Salbreux, G.; Roensch, J.; Joanny, J.-F.; Paluch, E., Role of cortical tension in bleb growth. *Proceedings of the National Academy of Sciences* **2009,** *106* (44), 18581.
58. Munjal, A.; Lecuit, T., Actomyosin networks and tissue morphogenesis. *Development* **2014,** *141* (9), 1789-1793.
59. Mayer, M.; Depken, M.; Bois, J. S.; Jülicher, F.; Grill, S. W., Anisotropies in cortical tension reveal the physical basis of polarizing cortical flows. *Nature* **2010,** *467* (7315), 617-621.
60. Fang, C.; Hui, T. H.; Wei, X.; Shao, X.; Lin, Y., A combined experimental and theoretical investigation on cellular blebbing. *Scientific Reports* **2017,** *7* (1), 16666.
61. Prost, J.; Jülicher, F.; Joanny, J. F., Active gel physics. *Nature Physics* **2015,** *11* (2), 111-117.
62. Speksnijder, J. E.; Terasaki, M.; Hage, W. J.; Jaffe, L. F.; Sardet, C., Polarity and reorganization of the endoplasmic reticulum during fertilization and ooplasmic segregation in the ascidian egg. *The Journal of cell biology* **1993,** *120* (6), 1337-1346.
63. Jeffery, W. R.; Swalla, B. J., The myoplasm of ascidian eggs: a localized cytoskeletal domain with multiple roles in embryonic development. *Semin Cell Biol* **1990,** *1* (5), 373-381.
64. Gualtieri, R.; Sardet, C., The endoplasmic reticulum network in the ascidian egg: localization and calcium content. *Biology of the Cell* **1989,** *65* (3), 301-304.
65. Zamponi, N.; Zamponi, E.; Cannas, S. A.; Billoni, O. V.; Helguera, P. R.; Chialvo, D. R., Mitochondrial network complexity emerges from fission/fusion dynamics. *Scientific Reports* **2018,** *8* (1), 363.
66. Rafelski, S. M., Mitochondrial network morphology: building an integrative, geometrical view. *BMC Biology* **2013,** *11* (1), 71.
67. Lee, K. L.; Marlow, F. L., Visualizing the Balbiani Body in Zebrafish Oocytes. *Methods in Molecular Biology* **2019,** *1920*, 277-293.

68. Chang, P.; Torres, J.; Lewis, R. A.; Mowry, K. L.; Houliston, E.; King, M. L., Localization of RNAs to the mitochondrial cloud in Xenopus oocytes through entrapment and association with endoplasmic reticulum. *Mol Biol Cell* **2004,** *15* (10), 4669-4681.
69. Boke, E.; Ruer, M.; Wühr, M.; Coughlin, M.; Lemaitre, R.; Gygi, S. P.; Alberti, S.; Drechsel, D.; Hyman, A. A.; Mitchison, T. J., Amyloid-like Self-Assembly of a Cellular Compartment. *Cell* **2016,** *166* (3), 637-650.
70. Zadpoor, A. A., Mechanics of Biological Tissues and Biomaterials: Current Trends. *Materials (Basel)* **2015,** *8* (7), 4505-4511.
71. Mittasch, M.; Gross, P.; Nestler, M.; Fritsch, A. W.; Iserman, C.; Kar, M.; Munder, M.; Voigt, A.; Alberti, S.; Grill, S. W.; Kreysing, M., Non-invasive perturbations of intracellular flow reveal physical principles of cell organization. *Nature Cell Biology* **2018,** *20* (3), 344-351.
72. Trushko, A.; Di Meglio, I.; Merzouki, A.; Blanch-Mercader, C.; Abuhattum, S.; Guck, J.; Alessandri, K.; Nassoy, P.; Kruse, K.; Chopard, B.; Roux, A., Buckling of an Epithelium Growing under Spherical Confinement. *Developmental Cell* **2020,** *54* (5), 655-668.e656.
73. Landau, L. D.; Lifshitz, E. M.; Sykes, J. B.; Reid, W. H.; Dill, E. H., Theory of Elasticity: Vol. 7 of Course of Theoretical Physics. *Physics Today* **1960,** *13* (7), 44-46.
74. Bischof, J.; Brand, C. A.; Somogyi, K.; Májer, I.; Thome, S.; Mori, M.; Schwarz, U. S.; Lénárt, P., A cdk1 gradient guides surface contraction waves in oocytes. *Nature Communications* **2017,** *8* (1), 849.
75. Lucero, A.; Stack, C.; Bresnick, A. R.; Shuster, C. B., A Global, Myosin Light Chain Kinase-dependent Increase in Myosin II Contractility Accompanies the Metaphase–Anaphase Transition in Sea Urchin Eggs. *Mol Biol Cell* **2006,** *17* (9), 4093-4104.
76. Paix, A.; Chenevert, J.; Sardet, C., Localization and Anchorage of Maternal mRNAs to Cortical Structures of Ascidian Eggs and Embryos Using High Resolution In Situ Hybridization. *Methods in molecular biology (Clifton, N.J.)* **2011,** *714*, 49-70.
77. Bodor, D. L.; Pönisch, W.; Endres, R. G.; Paluch, E. K., Of Cell Shapes and Motion: The Physical Basis of Animal Cell Migration. *Developmental Cell* **2020,** *52* (5), 550-562.
78. Charras, G. T.; Coughlin, M.; Mitchison, T. J.; Mahadevan, L., Life and Times of a Cellular Bleb. *Biophysical Journal* **2008,** *94* (5), 1836-1853.
79. Hannezo, E.; Dong, B.; Recho, P.; Joanny, J.-F.; Hayashi, S., Cortical instability drives periodic supracellular actin pattern formation in epithelial tubes. *Proceedings of the National Academy of Sciences* **2015,** *112* (28), 8620.
80. Callan-Jones, A.; Voituriez, R., Active Gel Model of Amoeboid Cell Motility. *New Journal of Physics* **2013,** *15*.
81. Mietke, A.; Jülicher, F.; Sbalzarini, I. F., Self-organized shape dynamics of active surfaces. *Proceedings of the National Academy of Sciences* **2019,** *116* (1), 29.
82. Mittasch, M.; Tran, V. M.; Rios, M. U.; Fritsch, A. W.; Enos, S. J.; Ferreira Gomes, B.; Bond, A.; Kreysing, M.; Woodruff, J. B., Regulated changes in material properties underlie centrosome disassembly during mitotic exit. *Journal of Cell Biology* **2020,** *219* (4).
83. Stringfellow, R. G.; Freund, L. B., The effect of interfacial friction on the buckle-driven spontaneous delamination of a compressed thin film. *International Journal of Solids and Structures* **1993,** *30* (10), 1379-1395.
84. Moore, A. S.; Coscia, S. M.; Simpson, C. L.; Ortega, F. E.; Wait, E. C.; Heddleston, J. M.; Nirschl, J. J.; Obara, C. J.; Guedes-Dias, P.; Boecker, C. A.; Chew, T.-L.; Theriot, J. A.;

Lippincott-Schwartz, J.; Holzbaur, E. L. F., Actin cables and comet tails organize mitochondrial networks in mitosis. *Nature* **2021,** *591* (7851), 659-664.
85. Boldogh, I. R.; Yang, H.-C.; Nowakowski, W. D.; Karmon, S. L.; Hays, L. G.; Yates, J. R.; Pon, L. A., Arp2/3 complex and actin dynamics are required for actin-based mitochondrial motility in yeast. *Proceedings of the National Academy of Sciences* **2001,** *98* (6), 3162.
86. Fung, T.; Ji, W.; Higgs, H.; Chakrabarti, R., Two distinct actin filament populations have effects on mitochondria, with differences in stimuli and assembly factors. *Journal of Cell Science* **2019,** *132*.
87. Jamieson-Lucy, A.; Mullins, M. C., Chapter One - The vertebrate Balbiani body, germ plasm, and oocyte polarity. In *Current Topics in Developmental Biology*, R. Lehmann, Ed. Academic Press: 2019; Vol. 135, pp 1-34.
88. Molliex, A.; Temirov, J.; Lee, J.; Coughlin, M.; Kanagaraj, A. P.; Kim, H. J.; Mittag, T.; Taylor, J. P., Phase separation by low complexity domains promotes stress granule assembly and drives pathological fibrillization. *Cell* **2015,** *163* (1), 123-133.
89. Kloc, M.; Etkin, L. D., RNA localization mechanisms in oocytes. *Journal of Cell Science* **2005,** *118* (2), 269-282.
90. Nishida, H.; Stach, T., Cell Lineages and Fate Maps in Tunicates: Conservation and Modification. *ZOOLOGICAL SCIENCE* **2014,** *31*, 645-652.
91. Nishida, H., Cell lineage analysis in ascidian embryos by intracellular injection of a tracer enzyme: III. Up to the tissue restricted stage. *Developmental Biology* **1987,** *121* (2), 526-541.
92. Sardet, C.; Dru, P.; Prodon, F., Maternal determinants and mRNAs in the cortex of ascidian oocytes, zygotes and embryos. *Biology of the cell / under the auspices of the European Cell Biology Organization* **2005,** *97*, 35-49.

References for 'Cytoplasm's got moves' see section 1.1.1

References for Appendix A see in section